Upsilon Spectroscopy using Lattice QCD

Paul McCallum

Department of Physics and Astronomy
University of Glasgow

Thesis submitted to the University of Glasgow
for the degree of Doctor of Philosophy
July 1997

To all my family in

recognition of the sacrifices they have made

Acknowledgements

I am indebted to my supervisor Christine Davies and to other members of the NRQCD collaboration, in particular John Sloan and Junko Shigemitsu. I would like to thank Andrew Lidsey, Sara Collins, Hugh Shanahan, Arifa Ali-Khan and Joachim Hein for their assistance and guidance throughout the years. I would also like to thank members of the theory group and others; Alessandro, Andy, Brian, Dan, David, Douglas, Gerry, Gordon, Jack, Laurence, Luke, Mark C, Mark G, Mark S, Nektarios, Scott, Steven, Stevie, Susan and Suzanne.

This work was kindly funded by the Particle Physics and Astronomy Research Council (PPARC).

Better to be a king in your own game than a pawn in someone else's

Declaration

Apart from chapters 1 and 2 and except where specific reference is made to the work of others, this thesis has been composed by the author.

Contents

Abstract

The non-relativistic QCD theory developed by the NRQCD collaboration is employed in simulations reproducing the upsilon spectrum. Correlations are analysed using multi-correlation fitting routines yielding energies and amplitudes. Good reproduction of the experimental upsilon spectrum is found with statistical errors comparable with systematic errors. The effects of three such systematic errors, lattice spacing, truncation of the relativistic expansion and quenching, are investigated. Radial and orbital splittings are found to have lattice spacing errors and truncation errors that are much smaller than statistical errors. These splittings give good to excellent agreement with experiment on the removal of quenching errors. Spin splittings and the wavefunction at the origin are found to have large lattice spacing, truncation and radiative correction errors which are of the order of 10%, comparable with statistical errors. These quantities give reasonable agreement with experiment on the removal of quenching errors and a prediction for the S state hyperfine splitting of 41(6) MeV is obtained.

The method developed by the NRQCD collaboration to obtain the strong coupling constant in the $\overline{\mathrm{MS}}$ scheme at the Z^0 mass is followed with lattice spacings determined from the upsilon radial and orbital splittings used to scale the coupling values. A best value of 0.1171(23) was obtained for this coupling. Sources of systematic error affecting this value are investigated and are found to be at the few percent level.

Chapter 1

Introduction to Quantum Field Theory

1.1 Lagrangian Field Theory

An invaluable tool in the study of field theory is the subject known as *Lagrangian mechanics*. Central to this subject are quantities known as the action, S, and the Lagrangian density, $\mathcal{L}$. Described in [1, 2], the action is defined in terms of the Lagrangian density by

$$S = \int_R d^4x \, \mathcal{L}(\phi, \partial_\mu \phi) \tag{1.1}$$

where the Langrangian density is itself given in terms of the field, $\phi(x)$, $x = (x^0, x^1, x^2, x^3)$, and its derivatives,

$$\partial_\mu \phi(x) \equiv \frac{\partial \phi(x)}{\partial x^\mu}, \qquad \mu = 0, 1, 2, 3. \tag{1.2}$$

One of the most important themes of Lagrangian mechanics is the *principle of least action*, which states that the actual motion of a field $\phi(x)$ is such that S is a minimum; that is $\delta S = 0$ for any incremental change in the motion. Considering such an arbitrary incremental change

$$\phi(x) \to \phi(x) + \delta\phi(x) \tag{1.3}$$

for which $\phi(x)$ remains the same on the surface of the volume R, then

$$\begin{aligned}
\delta S &= \int_R d^4x \left\{ \frac{\partial \mathcal{L}}{\partial \phi}\delta\phi + \frac{\partial \mathcal{L}}{\partial(\partial_\mu \phi)}\delta(\partial_\mu \phi) \right\} &(1.4)\\
&= \int_R d^4x \left\{ \frac{\partial \mathcal{L}}{\partial \phi} - \partial_\mu \left(\frac{\partial \mathcal{L}}{\partial(\partial_\mu \phi)} \right) \right\} \delta\phi + \int_R d^4x\, \partial_\mu \left(\frac{\partial \mathcal{L}}{\partial(\partial_\mu \phi)}\delta\phi \right). &(1.5)
\end{aligned}$$

The last term can be converted using into an integral over the surface of R using Gauss's divergence theorem, which then vanishes on account of $\delta\phi(x)$ being zero on this surface. Hence for $\delta S = 0$, the Euler–Lagrange equation of motion for the field $\phi(x)$,

$$\frac{\partial \mathcal{L}}{\partial \phi} = \partial_\mu \left(\frac{\partial \mathcal{L}}{\partial(\partial_\mu \phi)} \right), \tag{1.6}$$

can be extracted. This result can be generalised to any number and type of fields, $\phi_n(x)$, $n = 1, \ldots, N$, present in the Lagrangian density, $\mathcal{L}(\phi_n, \partial_\mu \phi_n)$.

Analogously to classical mechanics, momentum fields, $\pi_n(x)$, conjugate to the fields $\phi_n(x)$, can be defined by

$$\pi_n(x) = \frac{\partial \mathcal{L}}{\partial \dot{\phi}_n(x)} \tag{1.7}$$

where the $\dot{}$ indicates partial differentiation with respect to time. On quantisation, both the $\phi_n(x)$ and $\pi_n(x)$ fields are subject to the usual Heisenberg equal-time commutation relations:

$$[\phi_n(\mathbf{x}, t), \pi_m(\mathbf{x}', t)] = i\delta_{nm}\delta(\mathbf{x} - \mathbf{x}'), \tag{1.8}$$

$$[\phi_n(\mathbf{x}, t), \phi_m(\mathbf{x}', t)] = [\pi_n(\mathbf{x}, t), \pi_m(\mathbf{x}', t)] = 0. \tag{1.9}$$

Symmetry transformations can be applied to $\mathcal{L}$, leaving it invariant and giving rise to conserved quantities. Considering an infinitesimal such transformation to both the field $\phi(x)$ and the coordinates x^α,

$$
\begin{aligned}
x^\alpha &\rightarrow x'^\alpha && (1.10)\\
\phi(x) &\rightarrow \phi'(x') \quad , && (1.11)
\end{aligned}
$$

such that $\phi(x)$ and x^α remain constant on the surface of a volume R, the total change in ϕ, $\delta_T\phi(x)$, is given by

$$\delta_T\phi(x) = \delta\phi(x) + \partial_\alpha\phi(x)\,\delta x^\alpha, \tag{1.12}$$

where $\delta\phi(x)$ is the change induced in ϕ at constant x. The corresponding change in $\mathcal{L}$ is given by

$$
\begin{aligned}
\delta\mathcal{L} &= \frac{\partial\mathcal{L}}{\partial\phi}\delta\phi + \frac{\partial\mathcal{L}}{\partial(\partial_\mu\phi)}\delta(\partial_\mu\phi) + \frac{\partial\mathcal{L}}{\partial x^\alpha}\delta x^\alpha && (1.13)\\
&= \partial_\mu\left(\frac{\partial\mathcal{L}}{\partial(\partial_\mu\phi)}\delta\phi\right) + \frac{\partial\mathcal{L}}{\partial x^\alpha}\delta x^\alpha && (1.14)\\
&= \partial_\mu\left(\frac{\partial\mathcal{L}}{\partial(\partial_\mu\phi)}(\delta_T\phi - \partial_\alpha\phi\,\delta x^\alpha) + \mathcal{L}\delta x^\mu\right) && (1.15)
\end{aligned}
$$

using equations (1.12), (1.5) and the fact that $\phi(x)$ satisfies the Euler–Lagrange equation (1.6). For an invariant Lagrangian, $\delta\mathcal{L} = 0$ and so $\partial_\mu j^\mu = 0$ where

$$
\begin{aligned}
j^\mu &= \frac{\partial\mathcal{L}}{\partial(\partial_\mu\phi)}\delta_T\phi - \left\{\left(\frac{\partial\mathcal{L}}{\partial(\partial_\mu\phi)}\right)\partial_\beta\phi - \delta^\mu_\beta\mathcal{L}\right\}\delta x^\beta && (1.16)\\
&= \frac{\partial\mathcal{L}}{\partial(\partial_\mu\phi)}\delta_T\phi - \mathcal{T}^\mu_\beta\delta x^\beta && (1.17)
\end{aligned}
$$

$$\text{and} \qquad \mathcal{T}^\mu_\nu = \left(\frac{\partial\mathcal{L}}{\partial(\partial_\mu\phi)}\right)\partial_\nu\phi - \delta^\mu_\nu\mathcal{L}. \tag{1.18}$$

Again this result generalises to any number and type of fields, with summation over fields implied for terms containing more than one ϕ or derivative of ϕ.

Integration of $\partial_\mu j^\mu = 0$ over an arbitrary volume V gives

$$\int_V \partial_0 j^0 \, \mathbf{d^3x} + \int_V \partial_i j^i \, \mathbf{d^3x} = 0. \tag{1.19}$$

The last term can be converted using Gauss's divergence theorem into an integral over the surface of V, which then vanishes on account of $\delta\phi(x)$ and δx^α being zero on this surface. Hence,

$$\frac{\mathrm{d}}{\mathrm{dt}} \int_V j^0 \, \mathbf{d^3x} = 0 \tag{1.20}$$

and the quantity $Q = \int_V j^0 \, \mathbf{d^3x}$ is thus conserved. This consequence of symmetry transformations is known as *Noether's theorem.*

As an illustrative example, the transformation, known as a translation, given by

$$x^\alpha \to x^\alpha + \delta^\alpha \tag{1.21}$$

such that $\delta_T\phi = 0$ gives rise to the divergenceless current; $\partial_\mu \mathcal{T}^\mu_\beta = 0$ and so the conserved quantities are

$$P^\beta = \int \mathcal{T}^{0\beta} \, \mathbf{d^3x} \tag{1.22}$$

or more explicitly

$$\begin{aligned} P^0 &= \int \mathbf{d^3x} \{\pi(x)\dot{\phi}(x) - \mathcal{L}\} && (1.23)\\ &= \int \mathcal{H} \, \mathbf{d^3x} && (1.24) \end{aligned}$$

and

$$\begin{aligned} P^j &= \int \mathbf{d^3x} \, \pi(x) \frac{\partial\phi(x)}{\partial x_j} && (1.25)\\ &= \int \mathcal{P} \, \mathbf{d^3x}. && (1.26) \end{aligned}$$

P^β is the four momentum of the system, with $P^0 = H$ the Hamiltonian and $\mathbf{P} = (P^j)$ the momentum. $\mathcal{H}$ and $\mathcal{P}$ are respectively the energy and momentum densities.

1.2 Particle Interpretation of the Scalar Quantum Field

The scalar (having no spin) field, $\phi(x)$, provides a heuristic model of field theory, and on quantisation can be interpreted as a particle theory.

Applying (1.6) to the Lagrangian density

$$\mathcal{L} = \frac{1}{2}\left(\partial_\mu\phi(x)\partial^\mu\phi(x) - m^2\phi^2(x)\right) \tag{1.27}$$

yields the Klein–Gordon equation of motion,

$$(\Box + m^2)\phi(x) = 0. \tag{1.28}$$

With $\pi(x) = \dot{\phi}(x)$, for this Lagrangian density, substitution into equation (1.23) gives the Klein–Gordon Hamiltonian

$$H = \int \mathbf{d^3x}\,\frac{1}{2}\left(\dot{\phi}^2 + (\nabla\phi)^2 + m^2\phi^2\right). \tag{1.29}$$

Analogously to the non-relativistic Schrödinger case, the probability current is defined as

$$\mathbf{j} = -\frac{i}{2m}(\phi^*\nabla\phi - \phi\nabla\phi^*). \tag{1.30}$$

To conserve particle number however, Noether's theorem demands that a divergenceless probability four-current exists; $\partial_\mu j^\mu = 0$. For the probability current of (1.30), the appropriate time component, j^0, also known as the probability density ρ, ought to be

$$\rho = \frac{i}{2m}(\phi^* \partial_0 \phi - \phi \partial_0 \phi^*). \tag{1.31}$$

However, this probability density is not positive definite since ρ can assume negative values. To circumvent this problem, the field ϕ is no longer assumed to describe a single scalar particle, but instead may describe many scalar particles, creating and annihilating them appropriately. To see this, the field $\phi(x)$ is regarded as a hermitian operator, Fourier expanded according to

$$\phi(x) = \int \frac{\mathbf{d^3k}}{(2\pi)^3 2\omega_k} \left\{ a(k) e^{-ikx} + a^\dagger(k) e^{ikx} \right\} \tag{1.32}$$

with $\omega_k = (\mathbf{k^2} + m^2)^{1/2}$. Written more simply,

$$\phi(x) = \int \frac{\mathbf{d^3k}}{[(2\pi)^3 2\omega_k]^{1/2}} \left\{ f_k(x) a(k) + f_k^*(x) a^\dagger(k) \right\} \tag{1.33}$$

where the frequency functions $f_k(x)$ are given by

$$f_k(x) = \frac{1}{[(2\pi)^3 2\omega_k]^{1/2}} e^{-ikx} \tag{1.34}$$

and are orthonormal to one another using the inner product

$$\int \mathbf{d^3x} \left\{ f_k^*(x) i \frac{\partial f_{k'}(x)}{\partial t} - \frac{\partial f_k^*(x)}{\partial t} i f_{k'}(x) \right\} = \delta^3(\mathbf{k} - \mathbf{k'}). \tag{1.35}$$

The operators $a(k)$ and $a^\dagger(k)$, which will be shown to create and annihilate quanta, can be given in terms of the field $\phi(x)$ by inverting (1.33);

$$a(k) = \int \mathbf{d^3x} [(2\pi)^3 2\omega_k]^{1/2} \left\{ f_k^*(x) i \frac{\partial \phi(x)}{\partial t} - \frac{\partial f_k^*(x)}{\partial t} i \phi(x) \right\}, \tag{1.36}$$

$$a^\dagger(k) = \int \mathbf{d^3x} [(2\pi)^3 2\omega_{k'}]^{1/2} \left\{ \phi(x) i \frac{\partial f_{k'}(x)}{\partial t} - \frac{\partial \phi(x)}{\partial t} i f_{k'}(x) \right\}. \tag{1.37}$$

Combining these expressions, making use of the field commutation relations (1.8) and (1.9), gives the commutator of $a(k)$ and $a^\dagger(k')$,

$$[a(k), a^\dagger(k')] = (2\pi)^3 2\omega_k \delta^3(\mathbf{k} - \mathbf{k}'). \tag{1.38}$$

If $|n(k)\rangle$ is an eigenvector of $N(k) = a^\dagger(k)a(k)$ with eigenvalue $n(k)$,

$$N(k)|n(k)\rangle = n(k)|n(k)\rangle, \tag{1.39}$$

then $a^\dagger(k)|n(k)\rangle$ and $a(k)|n(k)\rangle$ are also eigenvectors of $N(k)$ with eigenvalues $n(k) + 1$ and $n(k) - 1$ respectively, implying that $a^\dagger(k)$ and $a(k)$ are creation and annihilation operators assuming $N(k)$ to be a number operator.

Substitution of (1.33) into (1.23) and (1.25) yields the following expressions for the energy and momentum operators

$$H = \int \frac{\mathbf{d^3k}}{(2\pi)^3 2\omega_k} N(k)\omega_k, \tag{1.40}$$

$$\mathbf{P} = \int \frac{\mathbf{d^3k}}{(2\pi)^3 2\omega_k} N(k)\mathbf{k} \tag{1.41}$$

where $\omega_k = (\mathbf{k^2} + m^2)^{1/2}$ and the zeros of both of these equations have been adjusted. In this particle interpretation, $N(k)$ is the number of particles of four-momentum k. $N(k)\omega_k$ and $N(k)\mathbf{k}$ are the total energy and total momentum of all particles present with momentum k, hence H and $\mathbf{P}$ give the total energy and total momentum of the system.

1.3 The Dirac Field

The Lagrangian density formed from the Dirac field $\psi(x)$ and its conjugate field $\overline{\psi}(x)$,

$$\mathcal{L} = \overline{\psi}(x) \left(i\gamma^\mu \partial_\mu - m\right) \psi(x) \tag{1.42}$$

gives rise, on application of (1.6), to the Dirac equation

$$(i\gamma^\mu \partial_\mu - m)\psi(x) = 0, \tag{1.43}$$

a relativistic equation describing the motion of fermions. Using equations (1.23) and (1.25) along with the Lagrangian density (1.42) and the fact that $\pi(x) = i\psi^\dagger(x)$, the Hamiltonian and momentum of a system of fermions are given by

$$H = \int \mathbf{d^3x}\, \overline{\psi}(x) \left\{ -i\gamma^j \partial_j + m \right\} \psi(x) \tag{1.44}$$

$$= \int \mathbf{d^3x}\, \psi^\dagger(x) i \frac{\partial \psi(x)}{\partial t} \quad , \tag{1.45}$$

using the Dirac equation (1.43), and

$$\mathbf{P} = -i \int \mathbf{d^3x}\, \psi^\dagger(x) \nabla \psi(x). \tag{1.46}$$

These are the familiar expressions for the expectation values of the operators $i\partial_t$ and $-i\nabla$.

Similarly to equation (1.33), the Dirac field and its conjugate field can be Fourier expanded in terms of the plain wave solutions to the Dirac equation, $u_s(p)e^{-ipx}$ and $v_s(p)e^{ipx}$;

$$\psi(x) = \int \frac{\mathbf{d^3p}\, m}{(2\pi)^3 \omega_p} \sum_s \left\{ b_s(p) u_s(p) e^{-ipx} + d_s^\dagger(p) v_s(p) e^{ipx} \right\}, \tag{1.47}$$

$$\overline{\psi}(x) = \int \frac{\mathbf{d^3p}\, m}{(2\pi)^3 \omega_p} \sum_s \left\{ b_s^\dagger(p) \overline{u}_s(p) e^{ipx} + d_s(p) \overline{v}_s(p) e^{-ipx} \right\} \tag{1.48}$$

where $\omega_p = (\mathbf{p}^2 + m^2)^{1/2}$ and the index s identifies two linearly independent positive energy spinors, u_1 and u_2 as well as two linearly independent negative energy spinors v_1 and v_2. Two types of creation/annihilation operators are needed to take account of the fact that particles are distinguishable from antiparticles. To satisfy the requirements of the *Pauli exclusion principle*, anticommutation relations are proposed for these creation and annihilation operators;

$$\{b_s(p), b^\dagger_{s'}(p')\} = \{d_s(p), d^\dagger_{s'}(p')\} = (2\pi)^3 \frac{\omega_p}{m} \delta^3(\mathbf{p} - \mathbf{p}')\delta_{ss'}, \tag{1.49}$$

$$\{b_s(p), b_{s'}(p')\} = \{b^\dagger_s(p), b^\dagger_{s'}(p')\} = 0, \tag{1.50}$$

$$\{d_s(p), d_{s'}(p')\} = \{d^\dagger_s(p), d^\dagger_{s'}(p')\} = 0. \tag{1.51}$$

On substituting the expressions (1.47) and (1.48) into equations (1.45) and (1.46), and using the anticommutation relations for the creation and annihilation operators, the Hamiltonian and momentum can be given in terms of these operators as

$$H = \int \frac{\mathbf{d^3p}\, m}{(2\pi)^3\omega_p} \omega_p \sum_s \left\{ b^\dagger_s(p) b_s(p) + d^\dagger_s(p) d_s(p) \right\}, \tag{1.52}$$

$$\mathbf{P} = \int \frac{\mathbf{d^3p}\, m}{(2\pi)^3\omega_p} \mathbf{p} \sum_s \left\{ b^\dagger_s(p) b_s(p) + d^\dagger_s(p) d_s(p) \right\}. \tag{1.53}$$

This time the particle interpretation gives $b^\dagger_s(p)b_s(p)$ as the number of particles of four-momentum p and spinor index s. Correspondingly, $d^\dagger_s(p)d_s(p)$ gives the number of antiparticles of four-momentum p and spinor index s.

1.4 The Electromagnetic Field and the Gauge Transformation

Defining the antisymmetric tensor $F^{\mu\nu}(x)$ in terms of the electromagnetic field $A^\mu(x)$ by

$$F^{\mu\nu}(x) = \partial^\mu A^\nu(x) - \partial^\nu A^\mu(x) \tag{1.54}$$

inherently satisfies two of Maxwell's equations. Then with both the Lagrangian density

$$\mathcal{L} = -\frac{1}{4} F_{\mu\nu}(x) F^{\mu\nu}(x) - \frac{1}{2}(\partial_\mu A^\mu(x))^2 \tag{1.55}$$

and the subsequent *Lorentz gauge condition* $\partial_\mu A^\mu(x) = 0$, application of the Euler–Lagrange equation (1.6) gives rise to the other Maxwell equations in vacuo;

$$\Box A^\mu(x) = 0. \tag{1.56}$$

The electromagnetic field $A^\mu(x)$ can be Fourier expanded in terms of plane wave solutions to (1.56),

$$A^\mu(x) = \int \frac{\mathbf{d^3k}}{(2\pi)^3 2\omega_k} \sum_s \varepsilon^\mu_{(s)}(k) \left\{ a_{(s)}(k) e^{-ikx} + a^\dagger_{(s)}(k) e^{ikx} \right\} \tag{1.57}$$

where $\omega_k = (\mathbf{k}^2 + m^2)^{1/2}$ and the index $s = 0, 1, 2, 3$ identifies four linearly independent polarisation vectors satisfying the normalisation

$$\varepsilon_{(s)} \cdot \varepsilon_{(s')} = g_{ss'}. \tag{1.58}$$

With the conjugate field $\pi^\mu(x)$ given by $\pi^\mu(x) = \frac{\partial \mathcal{L}}{\partial \dot{A}_\mu(x)}$, equation (1.55) gives explicitly $\pi^\mu(x) = F^{\mu 0}(x) - g^{\mu 0}(\partial_\nu A^\nu(x))$. Allowing $A^\mu(x)$ and $\pi^\mu(x)$ to satisfy the equal-time commutation relations

$$[A^\mu(\mathbf{x}, t), \pi^\nu(\mathbf{x}', t)] = i g^{\mu\nu} \delta^3(\mathbf{x} - \mathbf{x}'), \tag{1.59}$$

$$[A^\mu(\mathbf{x}, t), [A^\nu(\mathbf{x}', t)] = [\pi^\mu(\mathbf{x}, t), \pi^\nu(\mathbf{x}', t)] = 0 \tag{1.60}$$

gives the commutator of the creation and annihilation operators, $a^\dagger_{(s)}(k)$ and $a_{(s)}(k)$, as

$$[a_{(s)}(k), a^\dagger_{(s')}(k')] = -2 g_{ss'} \omega_k (2\pi)^3 \delta^3(\mathbf{k} - \mathbf{k}'). \tag{1.61}$$

Substitution of (1.57) and (1.55) into equation (1.23) and subsequent use of (1.61) yields the electromagnetic Hamiltonian

$$H = \int \frac{\mathbf{d^3k}}{(2\pi)^3 2\omega_k} \omega_k \left\{ \sum_{s=1}^{3} a^\dagger_{(s)}(k) a_{(s)}(k) - a^\dagger_{(0)}(k) a_{(0)}(k) \right\}. \tag{1.62}$$

The particle interpretation then implies that photons of four different polarisations contribute to the Hamiltonian—which is an unphysical result. To resolve this, the *Gupta–Bleuler condition* $\partial_\mu A^{(+)\mu}|\psi\rangle = 0$ is employed where $|\psi\rangle$ is an arbitrary state vector and $A^{(+)\mu}(x)$ is the half of equation (1.57) containing annihilation operators[1]. This condition implies a null expectation value for the Lorentz condition; $\langle\psi|\partial_\mu A^\mu|\psi\rangle = 0$ and leads to the result

$$\int \frac{\mathbf{d^3k}}{(2\pi)^3 2\omega_k}\omega_k \left(a_{(0)}(k) - a_{(3)}(k)\right) e^{-ikx}|\psi\rangle = 0 \quad , \tag{1.63}$$

that is

$$\int \frac{\mathbf{d^3k}}{(2\pi)^3 2\omega_k}\omega_k \langle\psi|a^\dagger_{(0)}(k)a_{(0)}(k)|\psi\rangle = \int \frac{\mathbf{d^3k}}{(2\pi)^3 2\omega_k}\omega_k \langle\psi|a^\dagger_{(3)}(k)a_{(3)}(k)|\psi\rangle \tag{1.64}$$

and so contributions to the Hamiltonian from the photon polarisation state with $s = 0$ cancel those with $s = 3$ leaving only two physical photon polarisation states.

Combining the Lorentz gauge Lagrangian (1.55) with that of the Dirac field (1.42), the total Lagrangian

$$\mathcal{L} = \overline{\psi}(x)(i\gamma^\mu\partial_\mu - m)\psi(x) - \frac{1}{4}F_{\mu\nu}(x)F^{\mu\nu}(x) - \frac{1}{2}(\partial_\mu A^\mu(x))^2 \tag{1.65}$$

describes a system of fermions and photons. This Lagrangian is invariant under the Lorentz to Lorentz gauge transformation

$$A^\mu(x) \to A^\mu(x) + \partial^\mu f(x) \qquad \text{with} \qquad \Box f(x) = 0. \tag{1.66}$$

However it is not invariant under the infinitesimal phase transformation to the fermion fields

$$\begin{aligned} \psi(x) &\to \psi(x) + ig\Lambda(x)\psi(x), \\ \overline{\psi}(x) &\to \overline{\psi}(x) - ig\Lambda(x)\overline{\psi}(x). \end{aligned} \tag{1.67}$$

[1] See [1] for a fuller account of this subject

To establish invariance, the derivative in the Dirac Lagrangian is replaced by the covariant derivative

$$D_\mu = \partial_\mu - igA_\mu(x) \tag{1.68}$$

and both transformations (1.66) and (1.67) are undergone simultaneously with $\Lambda(x) = f(x)$. It is the addition to the Lagrangian of this extra term $g\overline{\psi}(x)\gamma^\mu A_\mu(x)\psi(x)$ that enables the fermion and electromagnetic fields to couple and hence interact.

1.5 Particle Propagators

Section 1.2 showed that the scalar field could be decomposed into an infinite sum of operators which were shown to create and annihilate the quanta of the field. It should therefore be possible to create a particle from the vacuum at one space-time point and subsequently annihilate it at another. This idea is encapsulated in the *Feynman scalar propagator*, Δ_F, given by

$$i\Delta_F(x-y) = \langle 0|T\{\phi(x)\phi(y)\}|o\rangle \tag{1.69}$$

where the T denotes time ordering of the fields. $\Delta_F(x-y)$ is then equivalent to a scalar particle travelling from space-time point y to space-time point x. Using equation (1.33) and the commutator of the creation and annihilation operators (1.38), it can be shown that

$$\Delta_F(x-y) = \frac{1}{(2\pi)^4}\int d^4k\, \frac{e^{-ik(x-y)}}{k^2 - m^2} \tag{1.70}$$

where, unlike the previous sections, k_0 is being integrated over. Written this way, it is easily verified that

$$-(\Box + m^2)\Delta_F(x) = \delta^{(4)}(x) \tag{1.71}$$

and so the propagator is given by the inverse of the bilinear term appearing in the Lagrangian density (1.27).

Fermion and photon propagators for the fields of sections 1.3 and 1.4 can similarly be defined by

$$\begin{aligned} iS_F(x-y) &= \langle 0|T\{\psi(x)\overline{\psi}(y)\}|0\rangle, &(1.72)\\ iD_F^{\mu\nu}(x-y) &= \langle 0|T\{A^\mu(x)A^\nu(y)\}|0\rangle &(1.73)\end{aligned}$$

respectively. Like the scalar propagator, the fermion propagator can be written as

$$S_F(x-y) = \frac{1}{(2\pi)^4}\int d^4p\,\frac{\gamma^\mu p_\mu + m}{p^2 - m^2}e^{-ip(x-y)} \qquad (1.74)$$

with p_0 being integrated over. This form is equivalent to

$$S_F(x-y) = (i\gamma^\mu\partial_\mu + m)\Delta_F(x-y) \qquad (1.75)$$

and so again it is seen that the propagator is the inverse of the bilinear term appearing in the Lagrangian density (1.42). It is also noticeable in the fermion case, that if y is an earlier space-time point than x, then the propagator represents both an antiparticle travelling forwards in time and equivalently a particle travelling backwards in time.

1.6 Quantum Chromodynamics

Sections 1.3 and 1.4 essentially describe the behaviour of the fermions and bosons which comprise the theory of QED (Quantum Electrodynamics). However to successfully describe the theory of QCD (Quantum Chromodynamics), the $SU(3)$ group must be incorporated to account for the property of quarks and gluons known as *colour*. Consequently the gauge field becomes a 3×3 matrix and can be written as the linear combination $A^\mu(x) = \lambda_a A^\mu_a(x)/2$, where summation over the index a from 1 to 8 is implied. The gluon fields $A^\mu_a(x)$ are known as Yang–Mills fields and together ($a = 1, \ldots, 8$) they form a Yang–Mills vector. The eight 3×3 matrices λ_a are the generators of the $SU(3)$ group and are given, for example in the standard representation, in [1]. The electromagnetic tensor similarly becomes a 3×3 matrix; written as $F^{\mu\nu}(x) = \lambda_a F^{\mu\nu}_a(x)/2$ and defined according to

$$F^{\mu\nu}_a(x) = \partial^\mu A^\nu_a(x) - \partial^\nu A^\mu_a(x) + g f_{abc} A^\mu_b(x) A^\nu_c(x) \tag{1.76}$$

where the f_{abc} values are the structure constants of the $SU(3)$ group appearing in the commutation relation $[\lambda_a/2, \lambda_b/2] = i f_{abc} \lambda_c/2$.

The Lagrangian for QCD is given by

$$\mathcal{L} = \sum_q \overline{\psi}^i_q(x) \left(i\gamma^\mu D^{i,j}_\mu - m_q \delta^{ij} \right) \psi^j_q(x) - \frac{1}{4} F^a_{\mu\nu}(x) F^{\mu\nu}_a(x) \tag{1.77}$$

$$\text{with} \qquad D^{i,j}_\mu = \delta^{ij} \partial_\mu - ig \frac{\lambda^a_{i,j}}{2} A^a_\mu(x) \tag{1.78}$$

such that summation is undertaken over all quark flavours q for the fermionic piece. The fermion wavefunction, as well as being a 4-component Dirac spinor, becomes a 3-component vector in colour space.

For a quantum field theory such as QCD, amplitudes for particular processes can be calculated using Feynman diagrams. However certain Feynman diagrams involve loop momenta integrals that are divergent and so if the theory is to be believable, it must be renormalizable [2, 1]. This means that infinities arising from divergent integrals must be able to be cancelled by redefining the bare input parameters to the Lagrangian, such as the bare coupling and bare masses. This in turn results in renormalized couplings and masses that depend on the typical scales involved. In QCD the strong coupling constant is defined as $\alpha_s = g^2/4\pi$ and the renormalization scale dependence of this coupling is governed by the renormalization group equation [3]

$$\mu \frac{\partial \alpha_s(\mu)}{\partial \mu} = -\frac{\beta_0}{2\pi}\alpha_s^2(\mu) - \frac{\beta_1}{4\pi^2}\alpha_s^3(\mu) - \frac{\beta_2}{64\pi^3}\alpha_s^4(\mu) - \cdots \tag{1.79}$$

Although this equation is valid for all renormalization schemes, the β coefficients β_n for $n \geq 2$ are scheme dependent. The first two β coefficients and the third for the *modified minimal subtraction* ($\overline{\mathrm{MS}}$) scheme are given by

$$\beta_0 = 11 - \frac{2}{3}n_f, \tag{1.80}$$

$$\beta_1 = 51 - \frac{19}{3}n_f, \tag{1.81}$$

$$\beta_2 = 2857 - \frac{5033}{9}n_f + \frac{325}{27}n_f^2 \tag{1.82}$$

with n_f being the number of flavours with quark mass less than the scale μ. Solution of this differential equation for small α_s naturally introduces a constant of integration and this is generally taken to be either the value of α_s at an arbitrary reference scale μ_0 or an arbitrary reference scale value itself, Λ. Solution for α_s involves terms which contain logarithms of the ratio μ^2/Λ^2 (see for instance [3]).

A plot of $\alpha_s(\mu)$ against the scale μ exhibits a property of QCD known as *asymptotic freedom*; that is $\alpha_s \to 0$ as $\mu \to \infty$. Perturbation theory is then valid for processes with $\alpha_s \ll 1$. Hence expanding a general operator Q in terms of α_s,

$$Q = Q^{(0)} + Q^{(1)}\alpha_s + Q^{(2)}\alpha_s^2 + \cdots \quad , \tag{1.83}$$

successive corrections to the zero order estimate of a quantity $q^{(0)} = \langle\psi|Q^{(0)}|\psi\rangle$ can be made:

$$q = q^{(0)} + \alpha_s q^{(1)} + \alpha_s^2 q^{(2)} + \ldots \tag{1.84}$$

where $q^{(i)} = \langle\psi|Q^{(i)}|\psi\rangle$. Examples of perturbative processes are deep inelastic scattering and electron–positron collision experiments, described in [3].

1.6.1 Hadrons

Although quarks and gluons have colour, they are only ever observed as constituents of colourless objects known as *hadrons*. Hadrons having no gluonic excited content can be either of two types, *baryons* and *mesons*. Baryons are formed from three quarks, each having one of the three colours of $SU(3)$; mesons are formed from a quark and an antiquark, the antiquark possessing the anticolour corresponding to that of the quark. With six flavours of known quarks, *up, down, strange, charm, bottom* and *top*, a multitude of hadron combinations are possible many of which have been found experimentally. One combination in particular, that of a bottom quark (b) with a bottom antiquark ($\bar{b}$), gives rise to the *upsilon* (Υ) system of meson states and is the subject of this thesis.

With typical radial and orbital Υ splittings of $\sim$ 500 MeV ($\mathcal{O}(M_b v^2)$) and with an experimental b quark mass of around 4.5 GeV, the typical value for the square of the quark velocity is $v^2 \sim 0.1$ and so the b quarks in the Υ system are quite non-relativistic. The typical quark momentum (and therefore gluon momentum and energy) is $\mathcal{O}(M_b v) \sim 1.4$ GeV. At this low energy scale, $\alpha_s \not\ll 1$ and so perturbation theory is not a valid means of calculation. Described in the next section, *lattice gauge theory* was developed by Wilson in the early 1970s [4] and is the only calculational tool available in this non-perturbative regime. The Υ system yields well to lattice determination: comprising of two heavy quarks, light quark mass extrapolation (needed for heavy–light and light–light systems) is unnecessary; having a small physical volume, the Υ is less susceptible to finite volume errors and since the quarks are non-relativistic, their propagators are much quicker to calculate than those for relativistic quarks.

1.7 Lattice Gauge Theory

A lattice is a regular array of points (see figure (1.1)) such that the coordinates in this lattice space-time are restricted to these points, i.e. to multiples of the lattice spacing a;

$$x^\mu = n^\mu a \tag{1.85}$$

and so the field is given only at these coordinates $\phi(n^\mu a) \equiv \phi(n)$. Continuum derivatives and integrals are replaced by finite differences and sums

$$\partial_\mu \phi(x) \quad \rightarrow \quad \frac{1}{a}\left(\phi(n+\hat{\mu}) - \phi(n)\right), \tag{1.86}$$

$$\Box\phi(x) \quad \rightarrow \quad \frac{1}{a^2}\sum_\mu \left(\phi(n+\hat{\mu}) + \phi(n-\hat{\mu}) - 2\phi(n)\right), \tag{1.87}$$

$$\int d^4x \quad \rightarrow \quad a^4 \sum_n \tag{1.88}$$

where $\hat{\mu}$ is the unit vector in the μ direction.

1.7.1 Scalar field on the lattice

The Euclidean action for the scalar Lagrangian density of (1.27) is given by

$$S_E = \frac{1}{2}\int d^4x\, \phi(x)(-\Box + m^2)\phi(x) \tag{1.89}$$

and so the lattice equivalent is

$$S_E = -\sum_{n,\hat{\mu}} \hat{\phi}(n)\hat{\phi}(n+\hat{\mu}) + \frac{1}{2}(8+\hat{m}^2)\sum_n \hat{\phi}(n)\hat{\phi}(n) \tag{1.90}$$

where the quantities ϕ and m have absorbed appropriate powers of the lattice spacing to yield their dimensionless equivalents $\hat{\phi}$ and $\hat{m}$ (see for instance [5]). Alternatively, the action can be written in the form

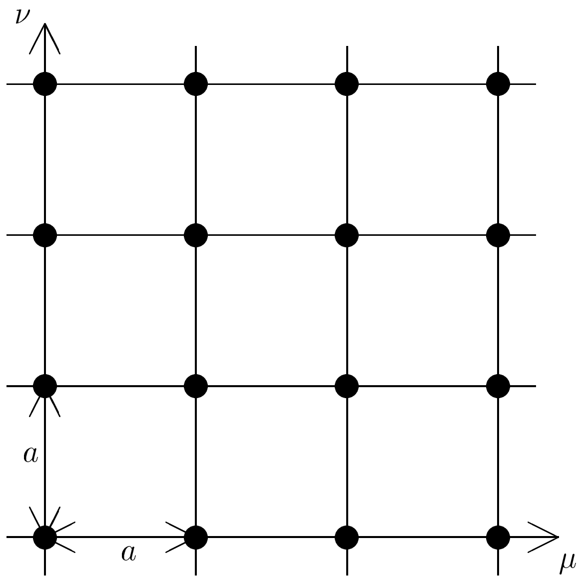

Figure 1.1: Example of a 2-dimensional lattice.

$$S_E = \frac{1}{2}\sum_{n,m}\hat{\phi}(n)K(n,m)\hat{\phi}(m) \tag{1.91}$$

with $K(n,m)$ given by

$$K(n,m) = -\sum_{\mu}(\delta_{n+\hat{\mu},m} + \delta_{n-\hat{\mu},m} - 2\delta_{n,m}) + \hat{m}^2\delta_{n,m}, \tag{1.92}$$

such that, by the reasoning of section 1.5, the scalar propagator is given by the inverse of $K(n,m)$, $K^{-1}(n,m)$. Giving the definitions of the lattice delta function and Fourier transform as

$$\delta_{n,m} = \int_{-\pi}^{\pi}\frac{d^4\hat{k}}{(2\pi)^4}e^{i\hat{k}(n-m)} \qquad \text{and} \qquad K(n,m) = \int_{-\pi}^{\pi}\frac{d^4\hat{k}}{(2\pi)^4}K(\hat{k})e^{i\hat{k}(n-m)}, \tag{1.93}$$

it is easily calculated that $K(\hat{k}) = 4\sum_{\mu}\sin^2\frac{\hat{k}_\mu}{2} + \hat{m}^2$ and with the inverse defined by $\sum_l K(n,l)K^{-1}(l,m) = \delta_{n,m}$, subsequent calculation yields

$$K^{-1}(n,m) = \frac{1}{(2\pi)^4} \int_{-\pi}^{\pi} d^4\hat{k}\, \frac{e^{i\hat{k}(n-m)}}{4\sum_\mu \sin^2 \frac{\hat{k}_\mu}{2} + \hat{m}^2}. \tag{1.94}$$

This expression for the lattice scalar propagator is seen to be similar to the Euclidean version of the continuum scalar propagator (Equation (1.70) but with a + sign in the denominator) and reduces to it in the zero lattice spacing limit.

1.7.2 Dirac field on the lattice

The Euclidean action for the Lagrangian density of the free Dirac field, (1.42), is given for one species of fermion by

$$S_E = \int d^4x\, \overline{\psi}(x)(\gamma_\mu \partial_\mu + m)\psi(x) \tag{1.95}$$

such that the Euclidean gamma matrices satisfy the anticommutating relationship $\{\gamma_\mu, \gamma_\nu\} = 2\delta_{\mu\nu}$. The lattice equivalent can be obtained by making the replacements

$$\int d^4x \quad \rightarrow \quad a^4 \sum_n, \tag{1.96}$$

$$\partial_\mu \psi(x) \quad \rightarrow \quad \frac{1}{2a}\left(\psi(n+\hat{\mu}) - \psi(n-\hat{\mu})\right) \tag{1.97}$$

and is

$$S_E = \sum_{n,m} \overline{\hat{\psi}}(n) K_F(n,m) \hat{\psi}(m) \tag{1.98}$$

with the matrix $K_F(n,m)$ given as (I being the identity matrix)

$$K_F(n,m) = \sum_\mu \frac{1}{2}\gamma_\mu(\delta_{n+\hat{\mu},m} - \delta_{n-\hat{\mu},m}) + \hat{m}\delta_{n,m} I \tag{1.99}$$

where again, the dimensionless quantities with hats have replaced their dimensionful counterparts after appropriate powers of the lattice spacing have been absorbed.

By the reasoning of section 1.5, the fermion propagator is given by the inverse of $K_F(n,m)$, $K_F^{-1}(n,m)$. Using the definitions of the lattice delta function and Fourier transform, (1.93), it is found that $K_F(\hat{p}) = \sum_\mu \gamma_\mu i \sin\hat{p}_\mu + \hat{m}I$. Subsequent calculation gives the lattice fermion propagator to be

$$K_F^{-1}(n,m) = \frac{1}{(2\pi)^4}\int_{-\pi}^{\pi} d^4\hat{p}\, \frac{-i\sum_\mu \gamma_\mu \sin\hat{p}_\mu + \hat{m}I}{\sum_\mu \sin^2\hat{p}_\mu + \hat{m}^2} e^{i\hat{p}(n-m)}. \tag{1.100}$$

Like the scalar propagator, this lattice fermion propagator is similar to its Euclidean continuum counterpart (Equation (1.74) with a + sign in the denominator). However, unlike the scalar propagator, the range of the sin function is $[-\pi, \pi]$ and so for each of the four space-time dimensions, there are two values of $\hat{p}_\mu$ giving the same sin value. Hence the propagator represents sixteen particles—clearly an untenable situation. To overcome this doubling problem *Wilson* proposed that the following modification term, which falls off linearly in the lattice spacing, be added to the action

$$-\frac{r}{2}\sum_n \bar{\hat{\psi}}(n)\Box\hat{\psi}(n) \tag{1.101}$$

where r is known as the Wilson parameter. This gives equation (1.98), however this time with

$$K_F^{(W)}(n,m) = (\hat{m}+4r)\delta_{n,m}I - \frac{1}{2}\sum_\mu \left((rI-\gamma_\mu)\delta_{n+\hat{\mu},m} + (rI+\gamma_\mu)\delta_{n-\hat{\mu},m}\right). \tag{1.102}$$

The resulting propagator, describing *Wilson fermions*, is that of equation (1.100) but with $\hat{m}$ replaced by $\hat{m} + 2r\sum_\mu \sin^2\left(\frac{\hat{p}_\mu}{2}\right)$ and so represents a single particle, while still converging to the continuum propagator in the zero lattice spacing limit.

1.7.3 Gauge field on the lattice

The gluonic gauge field is represented on the lattice by the unitary matrices

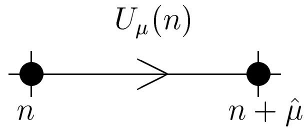

Figure 1.2: Gauge link at site n in μ direction

$$U_\mu(n) = e^{ig\hat{A}_\mu(n)} = e^{igaA_\mu(n)}. \tag{1.103}$$

Known as a *gauge link*, $U_\mu(n)$ connects the neighbouring points n and $n+\hat{\mu}$ and is directed from n to $n+\hat{\mu}$. The connection from $n+\hat{\mu}$ to n, $U_{-\mu}(n+\hat{\mu})$, is given by the hermitian conjugate of $U_\mu(n)$, $U_\mu^\dagger(n)$.

The lattice analogy of the local phase transformation (equations (1.66) and (1.67)) is given by

$$\begin{aligned} \hat{\psi}(n) &\rightarrow G(n)\hat{\psi}(n), & (1.104)\\ \overline{\hat{\psi}}(n) &\rightarrow \overline{\hat{\psi}}(n)G^{-1}(n), & (1.105)\\ U_\mu(n) &\rightarrow G(n)U_\mu(n)G^{-1}(n+\hat{\mu}) & (1.106) \end{aligned}$$

where the matrix $G(n)$ is a member of the $SU(3)$ group and is local to the site n. To maintain gauge invariance on the lattice, the Wilson fermion action is modified to include gauge links

$$\begin{aligned} S_F^{(W)} = (\hat{m}+4r)\sum_n \overline{\hat{\psi}}(n)\hat{\psi}(n) - \frac{1}{2}\sum_{n,\mu}\Big(&\overline{\hat{\psi}}(n)(rI-\gamma_\mu)U_\mu(n)\hat{\psi}(n+\hat{\mu}) \\ &+ \overline{\hat{\psi}}(n+\hat{\mu})(rI+\gamma_\mu)U_\mu^\dagger(n)\hat{\psi}(n)\Big), \end{aligned} \tag{1.107}$$

thereby taking a form analogous to the continuum case.

The smallest gauge invariant quantity constructed from the gauge field only is

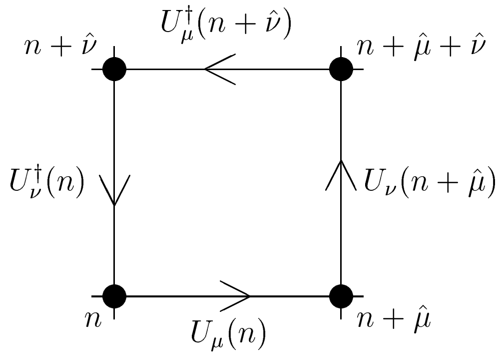

Figure 1.3: Plaquette in the $\mu\nu$ plane

the trace of the 1×1 Wilson loop known as the *plaquette*. Shown in figure (1.3), it is formed from four gauge links around a square in an anticlockwise direction;

$$U_P(n) = U_{\mu\nu}(n) = U_\mu(n)U_\nu(n+\hat\mu)U_\mu^\dagger(n+\hat\nu)U_\nu^\dagger(n). \tag{1.108}$$

It can then be observed that, accurate to $\mathcal{O}(a^2)$, $U_{\mu\nu}(n) = e^{iga^2F_{\mu\nu}(n)}$, allowing the lattice gauge Wilson action to be written as

$$S_G^{(W)} = \beta \sum_P \left(1 - \frac{\mathrm{Tr}}{6}(U_P + U_P^\dagger)\right) \tag{1.109}$$

where the sum is over all plaquettes and $\beta = 6/g^2$ is often used to specify the lattice since g is a function of a. This expression readily reduces to the continuum Euclidean gauge action $S_G = \frac{1}{2}\int d^4x\,\mathrm{Tr}(F_{\mu\nu}F_{\mu\nu})$ as the lattice spacing is taken to zero.

1.8 Numerical Lattice Simulations

An alternative to the canonical method of quantum field theory of sections 1.3 and 1.4 is the path integral approach developed by Feynman. This approach revolves around a central quantity known as the *partition function*, which is given on the lattice by

$$\mathcal{Z} = \int \mathcal{D}\overline{\psi}\mathcal{D}\psi\mathcal{D}U \, e^{-S_{\mathrm{QCD}}} \tag{1.110}$$

where $S_{\mathrm{QCD}} = S_G + S_F$, the sum of the gauge and fermion actions of equations (1.109) and (1.107) respectively. The integration measures are defined by the finite products

$$\mathcal{D}\psi = \prod_n d\psi(n), \quad \mathcal{D}\overline{\psi} = \prod_n d\overline{\psi}(n), \quad \mathcal{D}U = \prod_{n,\mu} dU_\mu(n). \tag{1.111}$$

Quantities such as the fermion propagator are calculated by taking the expectation values of the appropriate operators;

$$G(m,n) = \langle \psi(m)\overline{\psi}(n) \rangle = \frac{\int \mathcal{D}\overline{\psi}\mathcal{D}\psi\mathcal{D}U \, \psi(m)\overline{\psi}(n) e^{-S_{\mathrm{QCD}}}}{\int \mathcal{D}\overline{\psi}\mathcal{D}\psi\mathcal{D}U \, e^{-S_{\mathrm{QCD}}}}. \tag{1.112}$$

For this particular example, the fermionic part of the integration can be performed analytically giving

$$G(m,n) = \frac{\int \mathcal{D}U \, K_q^{-1}(U,m,n) \mathrm{det} K_F(U,m,n) e^{-S_G}}{\int \mathcal{D}U \, \mathrm{det} K_F(U,m,n) e^{-S_G}} \tag{1.113}$$

where $K_F(U,m,n)$ is the bilinear term appearing in the fermion action (1.107), summed over all flavours of quarks (for the particular case of QCD) and $K_q^{-1}(U,m,n)$ is the inverse of this bilinear term for the one flavour q of quark being propagated.

Performing the integration (1.113) is equivalent to performing integrations over all site, colour and space-time indices and is computationally unfeasible. To overcome this problem, (1.113) can be interpreted as an average over random configurations of gauge links, weighted by the probability density function $\mathrm{det} K_F(U,m,n) e^{-S_G}$. Methods for generating ensembles of these gauge link configurations with weighting $\mathrm{det} K_F(U,m,n) e^{-S_G}$, which are as statistically independent as practical, are detailed in [5]. Given such an ensemble, $\{U\}$, the propagator is calculated as

$$G(m,n) = \frac{1}{N_{conf}} \sum_{i=1}^{N_{conf}} K_q^{-1}(\{U\}_i, m, n). \tag{1.114}$$

When generating an ensemble, the weighting $\det K_F(U,m,n)e^{-S_G}$ is calculated for each configuration. Since $K_F(U,m,n)$ is generally a large matrix, this is computationally very expensive and so very often $\det K_F(U,m,n)$ is taken to be constant, resulting in an ensemble of quenched gauge configurations. Recent developments in computing power, however, have allowed the generation of ensembles with a small even number of fermions incorporated in $\det K_F(U,m,n)$, thus the lattice equivalent of allowing the vacuum polarization of gluons into loops of these fermions. Such enembles are known as dynamical gauge configuration ensembles. For many of the Υ mass splittings, the appropriate number of flavours of vacuum polarization quarks is $n_f = 3$ (see chapter 6), these being the u, d and s quarks. Since the dependence of mass splittings on the masses of these quarks is approximately linear [6, 7], and since the u and d quarks have negligible masses compared to the s quark, dynamical gauge configurations should be generated with two flavours of fermions having $\hat{m} = \hat{m}_s^0/3$, $\hat{m}_s^0$ being the dimensionless bare mass of the s quark. Hence, subsequent results from quenched and these dynamical gauge configurations will give correct mass splittings on extrapolation to $n_f = 3$. Unfortunately no dynamical configurations were available having $\hat{m} = \hat{m}_s^0/3$, however two ensembles were available [8] having two flavours of light quarks with masses close to $\hat{m}_s^0/3$ thus allowing an extrapolation to $\hat{m}_s^0/3$ [7].

Chapter 2

Non-Relativistic Quantum Chromodynamics

2.1 Potential Models

Following on from the successful application of potential models to QED it would be desirable to be able to apply this approach to QCD. However unlike QED, QCD is a non-abelian gauge theory and as such exhibits properties associated with this type of theory. Two of these properties are asymptotic freedom and colour confinement; asymptotic freedom implies a non-interacting theory in the infinite energy limit while colour confinement is the property whereby only colourless bound states of the interacting constituents are observed. Perturbation theory can be used to obtain the part of the potential associated with asymptotic freedom while non-perturbative methods must be used to obtain the part associated with colour confinement.

The perturbative part of the potential can be obtained by considering the amplitude for quark/antiquark elastic scattering with one gluon exchange. The appropriate S-matrix element is

$$S_{fi} = \delta_{fi} + i(2\pi)^4 \delta^{(4)}(P_f - P_i)\mathcal{M}_{fi}. \tag{2.1}$$

such that the potential $V(\mathbf{r})$ is given by the Fourier transform of $\mathcal{M}_{fi}(k)$. For an initial quark $q_i(p_1, \sigma_1)$ and antiquark $\overline{q}_j(p_2, \sigma_2)$, the factor $\delta_{i,j}/\sqrt{3}$ ensures a colourless meson state. The factor $\delta_{k,l}/\sqrt{3}$ is similarly used for the final quark $q_k(q_1, \tau_1)$ and antiquark $\overline{q}_l(q_2, \tau_2)$. Contributions from the s- and t-channels then give [9]

$$\begin{aligned}
\mathcal{M}_{fi} \quad = \quad & -\frac{1}{(2\pi)^6}\frac{m^2}{(E_{p_1}E_{p_2}E_{q_1}E_{q_2})^{1/2}} g_s^2 \frac{\delta_{i,j}}{\sqrt{3}}\frac{\delta_{k,l}}{\sqrt{3}} \\
& \times \left\{ \frac{1}{(p_1 - q_1)^2}\frac{\lambda^a_{k,i}}{2}\frac{\lambda^a_{j,l}}{2}\overline{u}(q_1, \tau_1)\gamma_\mu u(p_1, \sigma_1)\overline{v}(p_2, \sigma_2)\gamma^\mu v(q_2, \tau_2) \right. \\
& \left. - \frac{1}{(p_1 + p_2)^2}\frac{\lambda^a_{j,i}}{2}\frac{\lambda^a_{k,l}}{2}\overline{u}(q_1, \tau_1)\gamma_\mu v(q_2, \tau_2)\overline{v}(p_2, \sigma_2)\gamma^\mu u(p_1, \sigma_1) \right\}.
\end{aligned} \tag{2.2}$$

The contribution from the t-channel disappears while that from the s-channel gives

$$\mathcal{M}_{fi} = \frac{1}{(2\pi)^6}\frac{4}{3}\frac{g_s^2}{\mathbf{k}^2} \tag{2.3}$$

and so

$$V(r) = -\frac{4}{3}\frac{\alpha_s}{r}. \tag{2.4}$$

The non-perturbative part of the potential can be given by σr^n for $n > 0$ [9] and from lattice considerations as well as meson spectra, n is generally taken to be 1. This simplistic funnel potential

$$V(r) = -\frac{4}{3}\frac{\alpha_s}{r} + \sigma r, \tag{2.5}$$

known as the Cornell model [10], gives surprisingly good agreement with experiment for radial and orbital meson spectra states [11].

Many other potential models exist [9]. One such model known as the Richardson potential [12] has the form

$$V(r) = -\frac{4}{3}\frac{48\pi^2}{33-2n_f}\frac{1}{(2\pi)^3}\int \mathbf{d^3k}\,\frac{e^{i\mathbf{k}\cdot\mathbf{r}}}{\mathbf{k}^2\ln(1+\mathbf{k}^2/\Lambda^2)}. \tag{2.6}$$

For large $\mathbf{k}$ this has the form of a Coulombic potential and for small $\mathbf{k}$ it has the form of a linear potential. At intermediate $\mathbf{k}$ however, the potential has an r dependence that is approximately logarithmic. This potential also gives good agreement with experiment for radial and orbital meson spectra states [13].

2.1.1 Relativistic corrections to potential models

To obtain more accurate meson spectra predictions including predictions of spin splittings, relativistic corrections involving the spins of the quark and antiquark must be added to the basic static potential (2.5). This has been achieved in, for example, [14, 15]. The method of Eichten and Feinberg [14] gives the spin-dependent corrections to order $1/m^2$ as

$$\begin{aligned} V_{SD}(r) &= \frac{\mathbf{L}\cdot\mathbf{S}}{m^2 r}\left(\frac{\mathrm{d}V_0(r)}{2\mathrm{d}r}+\frac{\mathrm{d}V_1(r)}{\mathrm{d}r}+\frac{\mathrm{d}V_2(r)}{\mathrm{d}r}\right)+\frac{2\mathbf{S_1}\cdot\mathbf{S_2}}{3m^2}\nabla^2 V_2(r) \\ &\quad +\left(\frac{(\mathbf{S_1}\cdot\mathbf{r})(\mathbf{S_2}\cdot\mathbf{r})}{m^2 r^2}-\frac{\mathbf{S_1}\cdot\mathbf{S_2}}{3m^2}\right)V_3(r) \end{aligned} \tag{2.7}$$

where $\mathbf{S}=\mathbf{S_1}+\mathbf{S_2}$ is the total spin, $V_0(r)$ is the static potential (2.5) and such that the potentials V_i, $i=1,\ldots,3$ can be calculated non-perturbatively as the expectation values of correlations of components of the chromoelectric and chromomagnetic fields.

An alternative treatment similar to that of the previous section gives to order v^2 the Breit–Fermi Hamiltonian [9]

$$H = 2m+\frac{\mathbf{p}^2}{m}-\frac{\mathbf{p}^4}{4m^3}+V_0(r)+V_{SI}(r)+V_{LS}(r)+V_{SS}(r)+V_T(r). \tag{2.8}$$

Here, the static potential is assumed to consist of contributions that are both vector and scalar in nature;

$$V_0(r) = V_V(r) + V_S(r). \tag{2.9}$$

The vector contribution, $V_V(r)$, gives rise to the γ^μ matrices in equation (2.2) while the scalar contribution, $V_S(r)$, if included in equation (2.2) would have given rise to identity matrices where the γ^μ matrices are.

The spin-independent correction is cumbersome and is given in [9]. Of interest here are the spin-dependent correction terms, given by

$$\begin{aligned} V_{LS}(r) &= \frac{1}{2m^2 r}\left(3\frac{\mathrm{d}V_V(r)}{\mathrm{d}r} - \frac{\mathrm{d}V_S(r)}{\mathrm{d}r}\right)\mathbf{L}\cdot\mathbf{S}, & (2.10)\\ V_{SS}(r) &= \frac{2}{3m^2}\mathbf{S_1}\cdot\mathbf{S_2}\nabla^2 V_V(r), & (2.11)\\ V_T(r) &= \frac{1}{12m^2}\left(\frac{1}{r}\frac{\mathrm{d}V_V(r)}{\mathrm{d}r} - \frac{\mathrm{d}^2 V_V(r)}{\mathrm{d}r^2}\right)S_{12} & (2.12)\end{aligned}$$

where

$$S_{12} = 12\left(\frac{(\mathbf{S_1}\cdot\mathbf{r})(\mathbf{S_2}\cdot\mathbf{r})}{r^2} - \frac{\mathbf{S_1}\cdot\mathbf{S_2}}{3}\right). \tag{2.13}$$

Expectation values of the operators V_{LS}, V_{SS} and V_T can be obtained for appropriate states. To do this, it is necessary to calculate the expectation values of the operators $\mathbf{L}\cdot\mathbf{S}$, $\mathbf{S_1}\cdot\mathbf{S_2}$ and S_{12}. If S, L and J are the eigenvalues of the total spin $\mathbf{S}$, orbital angular momentum $\mathbf{L}$ and total angular momentum $\mathbf{J}$ respectively, it then follows that

$$\begin{aligned} \langle\mathbf{L}\cdot\mathbf{S}\rangle &= \frac{1}{2}\left(J(J+1) - L(L+1) - S(S+1)\right), & (2.14)\\ \langle\mathbf{S_1}\cdot\mathbf{S_2}\rangle &= \frac{1}{2}\left(S(S+1) - S_1(S_1+1) - S_2(S_2+1)\right) & (2.15)\end{aligned}$$

and non-trivially for the diagonal elements of S_{12} that

operator	state $^1S_0$	$^3S_1$	$^1P_1$	$^3P_0$	$^3P_1$	$^3P_2$
$\langle \mathbf{L}\cdot\mathbf{S}\rangle$	0	0	0	-2	-1	1
$\langle \mathbf{S_1}\cdot\mathbf{S_2}\rangle$	$-\frac{3}{4}$	$\frac{1}{4}$	$-\frac{3}{4}$	$\frac{1}{4}$	$\frac{1}{4}$	$\frac{1}{4}$
$\langle S_{12}\rangle$	0	0	0	-4	2	$-\frac{2}{5}$

Table 2.1: Eigenvalues of the spin-orbit, spin-spin and tensor operators for various states given by their spectroscopic notation.

$$\langle S_{12}\rangle = \frac{4}{(2L+3)(2L-1)}\left(S(S+1)L(L+1) - \frac{3}{2}\langle \mathbf{L}\cdot\mathbf{S}\rangle - 3\langle \mathbf{L}\cdot\mathbf{S}\rangle^2\right). \quad (2.16)$$

Immediately then it will be noticed that if a state has either $L = 0$ or $S = 0$, there will be no spin-orbit, V_{LS}, or tensor, V_T, contributions to the potential. Table (2.1) gives eigenvalues of the operators (2.14) to (2.16) for S and P states represented by the spectroscopic notation $^{2S+1}L_J$.

As stated earlier, the static potential is believed to consist of vector and scalar parts. To establish to what extent each part contributes, a quantity ρ known as the Peskin ratio [16] can be deployed. Defined by

$$\rho = \frac{M(^3P_2) - M(^3P_1)}{M(^3P_1) - M(^3P_0)} \quad (2.17)$$

only spin-dependent terms in the potential will contribute to this quantity and in fact, since $\langle S_{12}\rangle = 1/4$ for the ^3P_J states, only the spin-orbit and tensor terms will contribute. Assuming the static potential to be entirely of vector nature, i.e. $V_V = V_0$ and $V_S = 0$, gives

$$\rho = \frac{1}{5}\frac{8\alpha_s\langle r^{-3}\rangle + 7\sigma\langle r^{-1}\rangle}{2\alpha_s\langle r^{-3}\rangle + \sigma\langle r^{-1}\rangle} \quad (2.18)$$

which has the bounds $4/5 \leq \rho \leq 7/5$ corresponding to $\sigma = 0$ or $\alpha_s = 0$. The experimental value for the Peskin ratio for the Υ meson is $\rho_{exp} = 0.66$ [3], therefore ruling out this case. Assuming the static potential to be entirely of scalar nature, i.e. $V_S = V_0$ and $V_V = 0$, gives $\rho = 2$ which is also incompatible with experiment. On the other hand, putting $V_V = -4\alpha_s/3r$ and $V_S = \sigma r$ gives

$$\rho = \frac{1}{5}\frac{8\alpha_s\langle r^{-3}\rangle - \frac{5}{2}\sigma\langle r^{-1}\rangle}{2\alpha_s\langle r^{-3}\rangle - \frac{1}{4}\sigma\langle r^{-1}\rangle} \tag{2.19}$$

and so if the Coulomb part dominates, $\rho < 4/5$ in accord with experiment.

2.2 Motivation for NRQCD

The most attractive feature of studying hadrons composed of heavy quarks is the fact that the quarks can be treated in a non-relativistic framework. Potential models give the square of the typical quark velocity in the Υ meson as $v^2 \sim 0.1$ (see for example [15]). This low velocity leads to two important consequences. The first is that the probability of low energy gluon emission by the quarks in the meson is small; since the amplitude for a quark to radiate a gluon is proportional to v, the probability of a gluonic hybrid state, $P(Q\overline{Q}g)$, is suppressed by $\mathcal{O}(v^2)$. The second is the fact that an exchanged gluon has energy and hence momentum of the same order as the quark momenta and so its energy is thus larger than the quark kinetic energies by a factor of v. Consequently, exchanged gluons have reaction times that are $1/v$ smaller than those for the quarks and can therefore be approximated as instantaneous. these two consequences facilitate the study of heavy quark mesons as $Q\overline{Q}$ bound states interacting via instantaneous potentials. The potentials, described in the previous section, can be extracted on the lattice and bound states obtained using the Schrödinger equation for mesons.

The approach of NRQCD [17, 18, 19, 20, 21, 22], however, has the advantage over the potential model approach in that quark dynamics are retained, leading to a proper treatment of retardation effects. Therefore the appearance of hybrid states such as $Q\overline{Q}g$, whose component occurs with probability $\mathcal{O}(v^2) \sim 10\%$, as mentioned, and $Q\overline{Q}q\overline{q}$, where $q\overline{q}$ are a light quark/antiquark pair, are systematically accounted for. Another disadvantage with potential models is that they are phenomenological by nature and so to obtain an increasingly accurate predictive power, an increasing number of parameters are needed making the models overly complex—see for example [15]. In contrast NRQCD is formulated with, in principle, only two parameters and the accuracy of its predictive power can be increased comparatively easily.

NRQCD is one of only a few major theoretical approaches to studying heavy quark mesons and has been successfully applied to both heavy-heavy quark systems [23, 24, 25, 26, 27, 28, 29, 30] and heavy-light quark systems [31, 32, 33]. The major difficulty with studying non-relativistic systems is that they have a wide range of important energy scales—the highest being the quark mass $\sim M$, then the quark momentum $\sim Mv$ and the lowest being the quark kinetic energy $\sim Mv^2$. So to simulate the Υ on the lattice and be able to see all three energy scales requires, a lattice spacing that must be small compared with the wavelength $1/M$ (thereby minimising finite lattice spacing errors) and a lattice length that is large compared with the wavelength $1/Mv^2$ (thereby minimising finite volume errors). These requirements imply a space-time grid of around 80^4 which is clearly untenable on today's computing facilities. To get round this problem, the quark mass, which is the least important of the three energy scales in a non-relativistic system is sacrificed in the NRQCD simulation allowing for a much larger lattice spacing $a \sim 1/M$ and so a more realistic space-time grid of around 20^4. This is achieved by replacing the usual Dirac Lagrangian for quarks by an effective Lagrangian with the introduction of an ultraviolet cut-off $\Lambda \sim M$ so as to exclude relativistic momenta. This non-relativistic theory has many advantages over the original Dirac theory; the quark field decouples from the antiquark field allowing quark propagators to be calculated separately, the fermion doubling problem of section 1.7.2 is not encountered when dealing with non-relativistic propagators on the lattice and the non-relativistic propagators are far simpler and less costly to calculate than relativistic propagators.

2.3 Transforming the Dirac Theory

The Dirac theory can be regularized at non-relativistic energies by introducing the ultraviolet cut-off Λ so as to exclude relativistic momenta [18]. The effect of relativistic intermediate states, which are highly virtual and therefore local, is incorporated by adding to the Lagrangian local interaction terms in powers of $1/\Lambda$. The theory can then be renormalized at any finite order in $1/\Lambda$ by introducing extra coupling constants as coefficients of the extra interaction terms. This way, any desired accuracy $(p/\Lambda)^n$ is achieved by including all interactions up to order $1/\Lambda^n$ with the requirement that the couplings be determined by matching the modified theory to the full theory through order $(p/\Lambda)^n$. The modified theory is thus known as an effective field theory.

The Dirac theory can also be transformed into a non-relativistic theory by a transformation known as a Foldy–Wouthuysen–Tani (FWT) transformation [34, 35, 36] which allows the Lagrangian to be expanded in powers of $1/M$, so that

$$\begin{aligned} \overline{\Psi}(\gamma^\mu D_\mu - M)\Psi \quad \rightarrow \quad & \psi^\dagger \left(iD_t - M + \frac{\mathbf{D}^2}{2M} \right) \psi \\ & + \psi^\dagger \left(\frac{g}{2M} \boldsymbol{\sigma} \cdot \mathbf{B} + \frac{g}{8M^2} \boldsymbol{\nabla} \cdot \mathbf{E} + \frac{\mathbf{D}^4}{8M^3} + \cdots \right) \psi \\ & + \text{ antiquark terms } + \text{ quark-antiquark terms } + \cdots \end{aligned} \tag{2.20}$$

The 4-component Dirac spinor Ψ is decoupled by the unitary transformation

$$\Psi \rightarrow e^{-iS} \Psi \tag{2.21}$$

such that the upper components form a 2-component Pauli spinor ψ describing the quark dynamics, while the lower components similarly describe the antiquark dynamics. If both the regularization of the Dirac theory and the FWT transformation are combined, such that the cut-off $\Lambda \sim M$, then the FWT transformation (2.20) is essentially an expansion in powers of $1/\Lambda$ and so to obtain an accuracy of $(p/\Lambda)^n = v^n$, only terms up to order $1/\Lambda^n$ need be retained.

An easier alternative to the FWT transformation in establishing the relativistic correction terms of the NRQCD Lagrangian is the method developed in [20] and is followed here. Power counting rules, developed in the next section, are used to determine the magnitude of candidate correction terms such that a Lagrangian can be composed, accurate to any desired power of v.

2.4 The NRQCD Lagrangian

The lowest order FWT transformation applied to the Dirac theory gives a quark Lagrangian similar to that of the Schrödinger theory. When combined with the gauge field Lagrangian it looks like

$$\mathcal{L} = \psi^\dagger(x)\left(iD_t + \frac{\mathbf{D}^2}{2M}\right)\psi(x) - \frac{1}{4}F_{\mu\nu}(x)F^{\mu\nu}(x), \qquad (2.22)$$

where the mass term M has been omitted from the simulation and can be added as a constant shift later. In section 2.4.2 relativistic correction terms to this Lagrangian are considered, satisfying certain symmetries. Beforehand however, rules are developed to enable the contribution to the energy spectrum, in powers of M and v, of a particular term to be evaluated. Thereby a decision can be made on which terms must be included for a desired accuracy.

2.4.1 Power counting for NRQCD

The 2-component Pauli spinor representing the quark field, $\psi(x)$, or equivalently the field representing the antiquark, $\chi(x)$, is normalised to unity, hence

$$\int \mathbf{d^3x}\, \psi^\dagger(x)\psi(x) = 1. \tag{2.23}$$

By the uncertainty principle, the quark in a meson is localised within a region $\Delta x \sim 1/Mv$, therefore

$$\psi^\dagger(x)\psi(x) \sim (Mv)^3 \tag{2.24}$$

and so the quark field has magnitude $\psi(x) \sim (Mv)^{3/2}$. Naturally, the kinetic energy operator has expectation value

$$\int \mathbf{d^3x}\, \psi^\dagger(x)\frac{\mathbf{D}^2}{2M}\psi(x) \sim Mv^2 \tag{2.25}$$

and so $\mathbf{D} \sim Mv$. Hence, from the Schrödinger equation for the quark field,

$$\left(iD_t + \frac{\mathbf{D}^2}{2M}\right)\psi(x) = 0, \tag{2.26}$$

the temporal covariant derivative, D_t, has magnitude $\sim Mv^2$.

The natural gauge to use for non-relativistic dynamics is the Coulomb gauge, in which the spatial components of $A^\mu(x)$ are small. The temporal component, on the other hand, has a relatively large magnitude which can be estimated from the fact that $D_t = \partial_t + ig\phi(x)$, giving

$$g\phi(x) \sim Mv^2. \tag{2.27}$$

To estimate the magnitude of the spatial components of $A^\mu(x)$, the Euler–Lagrange equation

$$\frac{\partial\mathcal{L}}{\partial A^\mu} = \partial_\nu\left(\frac{\partial\mathcal{L}}{\partial(\partial_\nu A^\mu)}\right), \tag{2.28}$$

can be applied to the Lagrangian (2.22), giving the following field equations for $\phi(x)$ and $\mathbf{A}(x)$;

$$\nabla^2 g\phi(x) = -g^2\psi^\dagger(x)\psi(x) \qquad \text{and} \tag{2.29}$$

$$\left(\partial_t^2 - \nabla^2\right) g\mathbf{A}(x) = \frac{ig^2\boldsymbol{\nabla}\psi^\dagger(x)\psi(x)}{2M} - \frac{ig^2\psi^\dagger(x)\boldsymbol{\nabla}\psi(x)}{2M} + \partial_t\left(\boldsymbol{\nabla} g\phi(x)\right). \tag{2.30}$$

Equation (2.29) along with (2.24) and (2.27) give

$$g^2 \sim \frac{(Mv)^2(Mv^2)}{(Mv)^3} = v \tag{2.31}$$

and so from (2.30)

$$g\mathbf{A}(x) \sim \frac{1}{(Mv)^2}\left(\frac{v}{M}(Mv)^4 + (Mv^2)(Mv)(Mv^2)\right) = Mv^3. \tag{2.32}$$

Thus the electric and magnetic fields have magnitudes

$$g\mathbf{E}(x) = -\boldsymbol{\nabla} g\phi(x) + \cdots \sim (Mv)(Mv^2) = M^2v^3, \tag{2.33}$$

$$g\mathbf{B}(x) = \boldsymbol{\nabla} \times g\mathbf{A}(x) + \cdots \sim (Mv)(Mv^3) = M^2v^4 \tag{2.34}$$

where $\boldsymbol{\nabla}$, the momentum operator, $\sim Mv$.

2.4.2 Relativistic corrections

Relativistic corrections to the quark Lagrangian (2.22) must satisfy symmetries such as gauge invariance, parity, rotational symmetry. Only four such correction terms are needed to increase the accuracy of this Lagrangian by a factor of $\mathcal{O}(v^2)$. These are

$$c_1\frac{1}{M^3}\psi^\dagger(x)\mathbf{D}^4\psi(x), \tag{2.35}$$

$$c_2\frac{g}{M^2}\psi^\dagger(x)(\mathbf{D}\cdot\mathbf{E} - \mathbf{E}\cdot\mathbf{D})\psi(x), \tag{2.36}$$

$$c_3\frac{ig}{M^2}\psi^\dagger(x)\boldsymbol{\sigma}\cdot(\mathbf{D}\times\mathbf{E} - \mathbf{E}\times\mathbf{D})\psi(x), \tag{2.37}$$

$$c_4\frac{g}{M}\psi^\dagger(x)\boldsymbol{\sigma}\cdot\mathbf{B}\psi(x). \tag{2.38}$$

Other terms such as

$$f_1 \frac{g}{M^3} \psi^\dagger(x)\{\mathbf{D}^2, \boldsymbol{\sigma}\cdot\mathbf{B}\}\psi(x), \tag{2.39}$$

$$f_2 \frac{ig}{M^4} \psi^\dagger(x)\{\mathbf{D}^2, \boldsymbol{\sigma}\cdot(\mathbf{D}\times\mathbf{E} - \mathbf{E}\times\mathbf{D})\}\psi(x), \tag{2.40}$$

$$f_3 \frac{ig^2}{M^3} \psi^\dagger(x)\boldsymbol{\sigma}\cdot\mathbf{E}\times\mathbf{E}\psi(x) \tag{2.41}$$

are required to increase the accuracy by a factor of $\mathcal{O}(v^4)$. The effect of such higher order spin terms is investigated in [37].

The first of the four corrections, (2.35), comes from the expansion of the relativistic energy-momentum dispersion relation $E^2 = \mathbf{p}^2 + M^2$ to $\mathcal{O}(Mv^4)$. The second correction, (2.36), known as the Darwin term, accounts for the zero point energy caused by fluctuations in the quark's position. The fourth correction, (2.38), removes the degeneracy between states which have the same orbital angular momentum quantum number but differing spin, while the third correction, (2.37), is a spin-orbit coupling term and removes the degeneracy between states which have the same orbital angular momentum and spin quantum numbers but differing overall angular momentum.

To be able to use the non-relativistic Lagrangian composed of (2.22) and the four correction terms (2.35) to (2.38), the coupling constants g, M, c_1, c_2, c_3, c_4 must be evaluated. As discussed in section 1.8, g (rather than the lattice spacing a, since g is a function of a) is used to prescribe the lattice and a is subsequently determined by matching energy level splittings to their experimental values while the bare quark mass M_b^0 is tuned to match the Υ meson mass, determined from the dispersion relation, with its experimental value (see chapters 3 and 5). The artificial coupling constants c_1, c_2, c_3, c_4 all depend on the ultraviolet cut-off Λ. Taking Λ to infinity is not possible since these couplings contain power law divergences of type $\alpha_s\Lambda/M$, thereby rendering NRQCD non-renormalizable [18]. However with $\Lambda \sim M$, the couplings can be determined using perturbation theory. Tree-level values are obtained either by using the FWT transformation or by matching quantities such as scattering amplitudes in NRQCD with those of low energy QCD, described in the next section, while radiative corrections to these values are considered in section 2.6.4.

2.5 Establishing the Effective Field Theory

To establish the tree-level values of the couplings $c_1, \ldots, c_4$ requires matching results in NRQCD to those of low energy QCD through $\mathcal{O}(v^4)$ since the non-relativistic quark Lagrangian being considered is accurate to $\mathcal{O}(v^4)$. Examples are shown of how to calculate c_1, c_2 and c_3 following closely the work of [20].

For small momentum, the relativistic energy-momentum dispersion relation can be expanded as

$$E = (\mathbf{p}^2 + M^2)^{1/2} = M + \frac{\mathbf{p}^2}{2M} - \frac{\mathbf{p}^4}{8M^3} + \cdots \tag{2.42}$$

So to order v^4, the $\mathbf{p}^4$ shift in the energy is accounted for by the correction term (2.35). Since a shift in the energy $\delta\mathcal{H} = -\delta\mathcal{L}$ and the momentum operator $\mathbf{p} \equiv -i\boldsymbol{\nabla}$, c_1 is found to be 1/8.

The tree-level amplitude for a quark scattering off a static electric field in QCD is given by

$$\mathcal{M}(\mathbf{p}, \mathbf{q}) = ig\overline{u}(\mathbf{q})\gamma^0\phi(\mathbf{q} - \mathbf{p})u(\mathbf{p}) \tag{2.43}$$

where the Dirac spinor for the quark is written in terms of the Pauli spinor ψ as

$$u(\mathbf{p}) = \left(\frac{E_p + M}{2E_p}\right)^{\frac{1}{2}} \begin{bmatrix} \psi \\ \frac{\boldsymbol{\sigma}\cdot\mathbf{p}}{E_p+M}\psi \end{bmatrix} \tag{2.44}$$

and normalised non-relativistically such that $u^\dagger u = 1$. Inserting this spinor into the amplitude $\mathcal{M}(\mathbf{p}, \mathbf{q})$ and expanding the dispersion relation $E_p = (\mathbf{p}^2 + M^2)^{1/2}$ for small momenta, the amplitude can be divided into a spin-independent part and a spin-dependent part; $\mathcal{M}(\mathbf{p}, \mathbf{q}) = \mathcal{M}_{SI}(\mathbf{p}, \mathbf{q}) + \mathcal{M}_{SD}(\mathbf{p}, \mathbf{q})$ such that

$$\mathcal{M}_{SI}(\mathbf{p},\mathbf{q}) = \left(i - \frac{i(\mathbf{p}-\mathbf{q})^2}{8M^2}\right)\psi^\dagger g\phi(\mathbf{q}-\mathbf{p})\psi \qquad \text{and} \tag{2.45}$$

$$\mathcal{M}_{SD}(\mathbf{p},\mathbf{q}) = \left(\frac{-1}{4M^2} + \frac{3}{32M^4}(\mathbf{p}^2+\mathbf{q}^2)\right)\psi^\dagger \boldsymbol{\sigma}\cdot\mathbf{q}\times\mathbf{p}g\phi(\mathbf{q}-\mathbf{p})\psi. \tag{2.46}$$

Since $\mathbf{E}(\mathbf{x}) = -\boldsymbol{\nabla}\phi(\mathbf{x})$ for a static electric field, $\mathbf{E}(\mathbf{p}) \sim \mathbf{p}\phi(\mathbf{p})$ in momentum space and so the two parts contributing to $\mathcal{M}_{SI}(\mathbf{p},\mathbf{q})$ are accounted for by the NRQCD Lagrangian terms

$$\psi^\dagger(x)(iD_t)\psi(x) \qquad \text{and} \tag{2.47}$$

$$c_2\frac{g}{M^2}\psi^\dagger(x)(\mathbf{D}\cdot\mathbf{E}-\mathbf{E}\cdot\mathbf{D})\psi(x), \tag{2.48}$$

from which c_2 is found to be $1/8$. Likewise, the two parts contributing to $\mathcal{M}_{SD}(\mathbf{p},\mathbf{q})$ are accounted for by the terms

$$c_3\frac{ig}{M^2}\psi^\dagger(x)\boldsymbol{\sigma}\cdot(\mathbf{D}\times\mathbf{E}-\mathbf{E}\times\mathbf{D})\psi(x) \qquad \text{and} \tag{2.49}$$

$$f_2\frac{ig}{M^4}\psi^\dagger(x)\{\mathbf{D}^2,\boldsymbol{\sigma}\cdot(\mathbf{D}\times\mathbf{E}-\mathbf{E}\times\mathbf{D})\}\psi(x) \tag{2.50}$$

from which c_3 is also found to be $1/8$.

A similar analysis to the one above but with the quark scattering off a static vector potential gives a value of $1/2$ for c_4.

2.6 Lattice NRQCD

As explained in chapter 1, the lattice is a useful tool for studying low energy physics and so it is natural to study the Υ meson using NRQCD on the lattice. It is therefore better to work in Euclidean space and so the Euclidean space version of the NRQCD quark Lagrangian, developed in sections 2.4 and 2.5, is given by

$$\mathcal{L}_E = \psi^\dagger(x)\left(D_t - \frac{\mathbf{D}^2}{2M}\right)\psi(x) + \mathcal{L}_{SI} + \mathcal{L}_{SD} \tag{2.51}$$

where

$$\mathcal{L}_{SI} = -\frac{1}{8M^3}\psi^\dagger(x)\mathbf{D}^4\psi(x) + \frac{ig}{8M^2}\psi^\dagger(x)(\mathbf{D}\cdot\mathbf{E} - \mathbf{E}\cdot\mathbf{D})\psi(x), \tag{2.52}$$

$$\mathcal{L}_{SD} = -\frac{g}{8M^2}\psi^\dagger(x)(\boldsymbol{\sigma}\cdot\mathbf{D}\times\mathbf{E} - \boldsymbol{\sigma}\cdot\mathbf{E}\times\mathbf{D})\psi(x) - \frac{g}{2M}\psi^\dagger(x)\boldsymbol{\sigma}\cdot\mathbf{B}\psi(x). \tag{2.53}$$

The following sections discuss how to discretize the derivative operators and how to establish the chromomagnetic and chromoelectric fields in terms of the gauge field on the lattice.

2.6.1 Discretization

Outlined in section 1.7, covariant derivatives acting on the quark field are replaced on the lattice by either forward, backward or centred differences;

$$a\Delta_\mu\psi(x) = U_\mu(x)\psi(x+a\hat{\mu}) - \psi(x), \tag{2.54}$$

$$a\Delta_{-\mu}\psi(x) = \psi(x) - U_\mu^\dagger(x-a\hat{\mu})\psi(x-a\hat{\mu}), \tag{2.55}$$

$$\Delta_{\pm\mu}\psi(x) = \frac{1}{2}(\Delta_\mu + \Delta_{-\mu})\psi(x). \tag{2.56}$$

The inclusion of the gauge field matrices ensures that the gauge invariance of the Lagrangian is preserved. Likewise, the Laplacian operator $\mathbf{D}^2$ is replaced by the lattice Laplacian

$$\Delta^{(2)} = \sum_i \Delta_i\Delta_{-i} \tag{2.57}$$

and so the kinetic energy operator, H_0, is given by

$$H_0 = -\sum_i \frac{\Delta_i\Delta_{-i}}{2M}. \tag{2.58}$$

Retaining only the leading $\mathcal{O}(v^2)$ terms in the quark Lagrangian (2.51) gives a leading order discretized quark action

$$S_E^0 = a^3 \sum_x \psi^\dagger(x)\psi(x) - a^3 \sum_x \psi^\dagger(x+a\hat{t})U_4^\dagger(x)(1-aH_0)\psi(x) \tag{2.59}$$

and hence applying the equation $\sum_y K(x,y)G(y,0) = \delta_{\mathbf{x},\mathbf{0}}\delta_{t,0}$, where $K(x,y)$ is the bilinear term appearing in this action, yields the following evolution equation for the quark propagator[1]

$$G(\mathbf{x}, t+a) = U_4^\dagger(x)(1-aH_0)G(\mathbf{x},t) + \delta_{\mathbf{x},\mathbf{0}}\delta_{t+a,0}. \tag{2.60}$$

High momentum modes, however, cause this evolution equation to be unstable because

$$aH_0 = \sum_i \frac{4\sin^2\frac{p_i a}{2}}{2Ma}, \tag{2.61}$$

therefore $aH_0^{\max} = 6/Ma$ when $\mathbf{p} = (\frac{\pi}{a}, \frac{\pi}{a}, \frac{\pi}{a})$ and so $|1 - aH_0| \not< 1$ for $ma < 3$. Described in more detail in chapters 3 and 5 (sections 3.1 and 5.1), the range of dimensionless bare quark masses required for simulations at β values of 6.0 and 6.2 is $1 < aM_b^0 < 2$. Although the high momentum modes have little effect on Υ physics ($v^2 \sim 0.1$ for quarks in an Υ meson), they have to be modelled correctly. To do this, the quark action (2.59) is replaced by [20]

$$S_E^0 = a^3 \sum_x \psi^\dagger(x)\psi(x) - a^3 \sum_x \psi^\dagger(x+a\hat{t}) \left(1 - \frac{aH_0}{2n}\right)^n U_4^\dagger(x) \left(1 - \frac{aH_0}{2n}\right)^n \psi(x) \tag{2.62}$$

where n is a positive integer and so the evolution equation for the quark propagator becomes

$$G(\mathbf{x}, t+a) = \left(1 - \frac{aH_0}{2n}\right)^n U_4^\dagger(x) \left(1 - \frac{aH_0}{2n}\right)^n G(\mathbf{x},t) + \delta_{\mathbf{x},\mathbf{0}}\delta_{t+a,0}. \tag{2.63}$$

[1] Unless stated otherwise the quark Green's function or propagator is given by the implicit notation $G(\mathbf{x},t) \equiv G(\mathbf{x},t;\mathbf{x_0}=\mathbf{0},t_0=0)$.

The $U_4^\dagger(x)$ has been used to break the evolution into a more symmetrical form than that of (2.60), while the main change, that of introducing the parameter n, gives $|1 - aH_0/2n| < 1$ for $Ma > 3/2n$. Hence stability is achieved by using n values of 2 and 3 for simulations at $\beta = 6.0$ and 6.2. However the price for this stability is the introduction of unwanted terms which must be accounted for. This is dealt with in the next section.

To consider the $\mathcal{O}(v^4)$ terms in the quark Lagrangian (2.51) requires a definition of the chromomagnetic and chromoelectric fields on the lattice. This is achieved by defining the electromagnetic field in terms of plaquette operators using the standard cloverleaf representation [38],

$$F_{\mu\nu}^{(c)}(x) = -\frac{1}{4ga^2}\sum_P \mathcal{I}\left(U_{\mu\nu}(x)\right) \tag{2.64}$$

such that

$$\mathcal{I}\left(U_{\mu\nu}(x)\right) = \frac{U_{\mu\nu}(x) - U_{\mu\nu}^\dagger(x)}{2i} - \frac{I}{3}\mathrm{Im}(\mathrm{Tr}(U_{\mu\nu}(x))) \tag{2.65}$$

with the summation over the four plaquettes adjacent to point x lying in the $\mu\nu$ plane. This definition forces $F_{\mu\nu}^{(c)}(x)$ to be antihermitian and traceless, mimicking its continuum counterpart. The $\mathbf{E}$ and $\mathbf{B}$ fields are then defined at the lattice nodes by

$$E^i(x) = F_{0i}^{(c)}(x), \tag{2.66}$$

$$B^i(x) = \frac{1}{2}\varepsilon_{ijk}F_{jk}^{(c)}(x). \tag{2.67}$$

2.6.2 Discretization errors

With all lattice simulations, discretization inevitably leads to the introduction of systematic errors which must be accounted for or at least quantified if the predictions of a simulation are to be believed.

Taking the definitions of the difference operators, (2.54), (2.55) and (2.56), and Taylor expanding $\psi(x + a\hat{\mu})$ while expanding the gauge field $U_\mu(x) = e^{igaA_\mu(x)}$

as an exponential, the difference operators can be expanded as power series in the covariant derivative D_μ;

$$
\begin{aligned}
a\Delta_\mu &= aD_\mu + \frac{a^2}{2}D_\mu^2 + \ldots &(2.68)\\
a\Delta_{-\mu} &= aD_\mu - \frac{a^2}{2}D_\mu^2 + \ldots &(2.69)\\
a\Delta_{\pm\mu} &= aD_\mu + \frac{a^3}{6}D_\mu^3 + \ldots &(2.70)
\end{aligned}
$$

Therefore first order improvements on these differences, denoted by $\tilde{}$, are readily defined as

$$
\begin{aligned}
\tilde{\Delta}_\mu &= \Delta_\mu - \frac{a}{2}\Delta_\mu^2, &(2.71)\\
\tilde{\Delta}_{-\mu} &= \Delta_{-\mu} + \frac{a}{2}\Delta_{-\mu}^2, &(2.72)\\
\tilde{\Delta}_{\pm\mu} &= \Delta_{\pm\mu} - \frac{a^2}{6}\Delta_\mu\Delta_{\pm\mu}\Delta_{-\mu}. &(2.73)
\end{aligned}
$$

The Laplacian is similarly given by

$$a^2\Delta^{(2)} = \sum_i \left(a^2 D_i^2 + \frac{a^4}{12}D_i^4 + \ldots\right) \tag{2.74}$$

and so a corrected version is

$$\tilde{\Delta}^{(2)} = \Delta^{(2)} - \frac{a^2}{12}\sum_i (\Delta_i\Delta_{-i})^2. \tag{2.75}$$

The quark action (2.62) was obtained by replacing D_t in the continuum quark Lagrangian with Δ_{-4}. Improving this difference according to (2.72) would mean conceding the single time derivative nature of the NRQCD theory and hence the problem would cease to be an initial value one. As an alternative approach, the temporal covariant derivative may be written

$$aD_4 = a\Delta_{-4} + \frac{a^2}{2}D_4^2 - \frac{a^3}{6}D_4^3 + \frac{a^4}{24}D_4^4 - \ldots \tag{2.76}$$

and so when replacing aD_4 with $a\Delta_{-4}$, the extra terms can be absorbed (making use of the fact that $D_4 \approx \mathbf{D}^2/2M$ at lowest order) into an exponentiated H_0 factor. This improvement gives rise to the modified evolution equation

$$G(\mathbf{x}, t+a) = U_4^\dagger(x) e^{-aH_0} G(\mathbf{x}, t) + \delta_{\mathbf{x},\mathbf{0}}\delta_{t+a,0} \tag{2.77}$$

which can be implemented by expanding the exponential power series. However for reasons of stability discussed in the previous section, it is desirable to use equation (2.63) to evolve the quark propagator at lowest order. A comparison of the two evolution equations gives the effective Hamiltonian of the second in terms of the Hamiltonian of the first as

$$H_{\text{eff}} = -\frac{2n}{a}\ln\left(1 - \frac{aH_0}{2n}\right) \tag{2.78}$$

and so to compensate for the introduction of the stability parameter n, the lowest order Hamiltonian is replaced by the improved version

$$\tilde{H}_0 = H_0 - \frac{a}{4n}H_0^2. \tag{2.79}$$

The cloverleaf electromagnetic field $F_{\mu\nu}^{(c)}(x)$ can also be improved—this is detailed in [20]. However, as will shortly be seen, this improvement is unnecessary when working to $\mathcal{O}(v^4)$.

As established in section 2.4, the last four terms appearing in the quark Lagrangian (2.51) have magnitude $\mathcal{O}(Mv^4)$. Therefore any errors resulting from discretization which have magnitude $\mathcal{O}(Mv^4)$ or larger must be corrected for in order that the simulation be accurate to $\mathcal{O}(Mv^4)$. Immediately then, it will be noticed that improvements to the electromagnetic field, which are a factor $\mathcal{O}(a^2M^2v^2)$ smaller ($\mathcal{O}(v^2)$ smaller since $a \sim 1/M$) than the lowest order field, are unnecessary when working to $\mathcal{O}(Mv^4)$. Likewise, the term which improves the centred difference operator, given in (2.73), is $\mathcal{O}(a^2M^2v^2) \sim \mathcal{O}(v^2)$ smaller than the difference operator itself and since this difference operator is only needed in the $\mathcal{O}(Mv^4)$ terms of (2.52) and (2.53), the improved version is unnecessary.

Improvements to the Hamiltonian resulting from the time derivative and lattice Laplacian, however, evaluate according to

$$-\frac{a}{4n}H_0^2 \sim a(Mv^2)^2 \sim Mv^4, \tag{2.80}$$

$$\frac{a^2}{24M}\sum_i(\Delta_i\Delta_{-i})^2 \sim \frac{a^2}{M}(M^2v^2)^2 \sim Mv^4. \tag{2.81}$$

Therefore their inclusion is required and the way in which this is done is shown in the next section.

2.6.3 Evolution of the quark propagator

The evolution equation for the quark propagator (2.63) was sufficient for leading $\mathcal{O}(v^2)$ terms. Now that all corrections to $\mathcal{O}(v^4)$ have been established, the evolution equation can be modified to accommodate them;

$$G(\mathbf{x},t+a) = \left(1-\frac{aH_0}{2n}\right)^n U_4^\dagger(x)\left(1-\frac{aH_0}{2n}\right)^n(1-a\delta H)G(\mathbf{x},t) \tag{2.82}$$

was used for the $\beta = 6.0$ simulations in chapter 3, while

$$G(\mathbf{x},t+a) = \left(1-\frac{a\delta H}{2}\right)\left(1-\frac{aH_0}{2n}\right)^n U_4^\dagger(x)\left(1-\frac{aH_0}{2n}\right)^n\left(1-\frac{a\delta H}{2}\right)G(\mathbf{x},t) \tag{2.83}$$

was used for the $\beta = 6.2$ simulations in chapter 5. In either case, the initial condition is given by

$$G(\mathbf{x},0) = \delta_{\mathbf{x},\mathbf{0}}. \tag{2.84}$$

The kinetic energy operator H_0 is defined in (2.58) while δH contains all six relativistic and lattice spacing corrections[2],

[2]From here onwards the bare b quark mass is denoted by the more explicit notation M_b^0

$$\delta H = -\frac{(\Delta^{(2)})^2}{8(M_b^0)^3} + \frac{ig}{8(M_b^0)^2}(\mathbf{\Delta}_\pm \cdot \mathbf{E} - \mathbf{E} \cdot \mathbf{\Delta}_\pm) - \frac{g}{8(M_b^0)^2}\boldsymbol{\sigma} \cdot (\mathbf{\Delta}_\pm \times \mathbf{E} - \mathbf{E} \times \mathbf{\Delta}_\pm)$$
$$-\frac{g}{2M_b^0}\boldsymbol{\sigma} \cdot \mathbf{B} + \frac{a^2\Delta^{(4)}}{24M_b^0} - \frac{a(\Delta^{(2)})^2}{16n(M_b^0)^2}. \tag{2.85}$$

The centred difference operator as a three-vector is given by $\mathbf{\Delta}_\pm$ and so the first four terms correspond to those in (2.51). The last two terms are the spatial and temporal lattice spacing corrections such that $\Delta^{(4)} = \sum_i (\Delta_i \Delta_{-i})^2$. All difference operators act on everything to their right with their action on the propagator analogous to that of the wavefunction in equations (2.54), (2.55) and (2.56). The action of the centred difference operator on the $\mathbf{E}$ field however,

$$\mathbf{\Delta}_\pm \cdot \mathbf{E} = \frac{1}{2a}\sum_i \left\{U_i(x)E^i(x+a\hat{i})U_i^\dagger(x) - U_i^\dagger(x-a\hat{i})E^i(x-a\hat{i})U_i(x-a\hat{i})\right\}, \tag{2.86}$$

is different to that of (2.56) in order to preserve gauge invariance of the lattice Lagrangian.

For practical reasons, both quark evolution equations (2.82) and (2.83) are split into two parts; the gauge field matrices are read in by the simulation code and the part of the evolution to the left of the $U_4^\dagger(x)$ is performed first. Appropriate meson correlations are calculated at this point and then the quark propagators are evolved further according to the right hand part of equations (2.82) and (2.83), up to and including the $U_4^\dagger(x)$ so that effectively the evolution starts and ends at the $U_4^\dagger(x)$. Gauge field matrices for the next timeslice are then read in by the simulation code and the process repeated. The way in which the meson correlations are calculated and the types used in order to simulate particular states of the Υ system are described in section 2.7.

2.6.4 Dealing with radiative corrections to the coupling constants

In section 2.4.2 candidate relativistic correction terms to the non-relativistic quark Lagrangian (2.22) were considered each with its own coupling constant c_i. Tree-level values for these couplings were obtained in section 2.5 by matching results from NRQCD with low energy QCD, however radiative corrections to these tree-level values are believed to be large and must therefore be accounted for.

The reason for believing that the radiative corrections are large comes from the general disagreement between Monte Carlo estimates for short distance quantities on the lattice and lowest order lattice perturbation theory estimates. An example is the Monte Carlo estimate for the link operator in Landau gauge [39] which is given at $\beta = 6.0$ by

$$\left\langle 1 - \frac{1}{3}\mathrm{Tr}U_\mu \right\rangle_{\mathrm{MC}} = 0.139. \tag{2.87}$$

This is the lattice analogue of the expectation value of the square of the gauge field A_μ. Since $\langle A_\mu^2 \rangle$ is quadratically divergent, the loop integral is dominated by momenta close to the cut-off and so at $\beta = 6.0$ perturbation theory should be valid, giving

$$1 - \frac{1}{3}\mathrm{Tr}U_\mu = 0.97\alpha_L \tag{2.88}$$

where $\alpha_L \equiv g^2/4\pi$. At $\beta = 6.0$, $\alpha_L = 0.08$ and so 0.078 is obtained for the perturbative estimate of $1 - \frac{1}{3}\mathrm{Tr}U_\mu$, substantially different from the Monte Carlo estimate. Discrepancies such as these are caused by the nonlinear relation between the gauge link and the gauge field which when expanded does not converge to the continuum analogue with vanishing lattice spacing, as might naively be expected;

$$U_\mu(x) = e^{iagA_\mu(x)} \not\rightarrow 1 + iagA_\mu(x). \tag{2.89}$$

This is because in the quantum theory, higher order A_μ terms generate ultraviolet divergences which cancel the additional powers of a and so they are only suppressed by powers of g. These unwanted higher order contributions are tadpole contributions and they lead to large scale independent renormalizations between the bare lattice coupling α_L and continuum couplings such as α_V and $\alpha_{\overline{\rm MS}}$. This in turn leads to large coefficients for perturbative expansions in α_L and therefore poor convergence of these expansions.

There are many ways to get round the problem of having a poor expansion parameter for lattice perturbation theory [39]. Perhaps the most appropriate in the context of this thesis is the method whereby the ultraviolet modes in the link operator are integrated out and averaged over leaving only the continuum like infrared part of the gauge field

$$U_\mu(x) \approx u_0(1 + iagA_\mu(x)) \tag{2.90}$$

where the parameter u_0 contains the averaged ultraviolet contribution. u_0 can be defined in many ways, here it is chosen to be the fourth root of the plaquette expectation value

$$u_0 = \left\langle \frac{1}{3}\mathrm{Tr}U_P \right\rangle^{1/4} \tag{2.91}$$

and evaluates at around $0.8 \sim 0.9$ for simulations at $\beta \sim 6.0$. So for a more continuum-like behaviour, all gauge links appearing in operators are divided by this parameter u_0. For instance, since the chromoelectric and chromomagnetic fields are defined in terms of plaquette operators using the standard cloverleaf representation, they are replaced by

$$\mathbf{E} \rightarrow \frac{\mathbf{E}}{u_0^4} \tag{2.92}$$

$$\mathbf{B} \rightarrow \frac{\mathbf{B}}{u_0^4} \tag{2.93}$$

and therefore neglecting tadpole improvement results in severe underestimation of spin-dependent splittings.

Similarly, to obtain a more continuum-like gauge action, the bare lattice coupling g can be replaced by a modified lattice coupling $\tilde{g}$ such that [39]

$$\tilde{g}^2 = \frac{g^2}{u_0^4}. \tag{2.94}$$

Expanding in the coupling $\tilde{\alpha}_L = \tilde{g}^2/4\pi$ then gives perturbative series similar to those of the continuum couplings—in particular, perturbative series that are far more convergent. Hence using this tadpole improvement prescription gives radiative corrections to the coupling constants $c_1, \ldots, c_6$ that are believed to be $\sim 10\%$ of the tree-level values [40] and so are comparable with next order terms in the v^2 expansion (terms of order Mv^6). Since these terms were not included for the work in this thesis, it is reasonable to neglect the radiative corrections also, as was done.

2.7 Lattice Meson Correlations

As seen in section 2.3, the FWT transformation decouples the 4-component Dirac spinor Ψ into a 2-component Pauli spinor ψ describing the quark dynamics and a 2-component Pauli spinor χ describing the antiquark dynamics. The quark action, developed in the preceeding sections, can be written as

$$S_Q = \sum_{x,y} \psi^\dagger(x) K_Q(x,y) \psi(y) \tag{2.95}$$

where $K_Q(x,y)$ denotes the bilinear term from which the quark propagator can be subsequently derived. Similarly the antiquark action can be written as

$$S_A = \sum_{x,y} \chi^\dagger(x) K_A(x,y) \chi(y) \tag{2.96}$$

such that, as a consequence of the decoupling, $K_A(x,y) = K_Q^*(x,y)$. This important connection between the quark and antiquark dynamics means that it is unnecessary to recalculate the work of the preceeding sections to obtain the antiquark propagator; instead the antiquark propagator is given simply by the complex conjugate of the quark propagator.

Since $\psi^\dagger(x)$ creates a b quark and $\chi^\dagger(x)$ creates a b antiquark, combining these gives an operator that creates an Υ meson with momentum $\mathbf{p}$;

$$O^\dagger(\mathbf{p},t) = \sum_{\mathbf{x_1},\mathbf{x_2}} \psi^\dagger(\mathbf{x_1},t)\Gamma(\mathbf{x_1}-\mathbf{x_2})\chi^\dagger(\mathbf{x_2},t)e^{i\frac{\mathbf{p}}{2}\cdot(\mathbf{x_1}+\mathbf{x_2})}. \tag{2.97}$$

The sum over spatial sites and the exponential factor effectively Fourier transform the convolution lying between them to ensure that the meson has definite momentum $\mathbf{p}$, while the factor $\Gamma(\mathbf{x_1}-\mathbf{x_2})$, known as a meson operator, maximises the overlap of the meson with a particular desired channel. These meson operators will be described in sections 2.7.1 and 2.7.2.

An Υ meson propagating with momentum $\mathbf{p}$ between the times $t=0$ and $t=t$ in the Heisenberg picture can then be represented by the correlation

$$_H\langle 0,t=t|O(\mathbf{p},t)O^\dagger(\mathbf{p},0)|0,t=0\rangle_H \tag{2.98}$$

$$\begin{aligned} = {}& _H\langle 0,t=t| \sum_{\mathbf{y_1},\mathbf{y_2}} \chi_{k;\beta}(\mathbf{y_2},t)\Gamma^{(sk)\dagger}_{k,l}(\mathbf{y_1}-\mathbf{y_2})\psi_{l;\beta}(\mathbf{y_1},t)e^{-i\frac{\mathbf{p}}{2}\cdot(\mathbf{y_1}+\mathbf{y_2})} \\ &\times \sum_{\mathbf{x_1},\mathbf{x_2}} \psi^\dagger_{i;\alpha}(\mathbf{x_1},0)\Gamma^{(sc)}_{i,j}(\mathbf{x_1}-\mathbf{x_2})\chi^\dagger_{j;\alpha}(\mathbf{x_2},0)e^{i\frac{\mathbf{p}}{2}\cdot(\mathbf{x_1}+\mathbf{x_2})}|0,t=0\rangle_H \end{aligned} \tag{2.99}$$

where the spin and colour indices have been made explicit and the meson operators at the source and sink have been distinguished. Using translational invariance to eliminate the sum over the initial antiquark position and then rearranging gives

$$\begin{aligned} & _H\langle 0,t=t| \sum_{\mathbf{y_1},\mathbf{y_2}} \chi_{k;\beta}(\mathbf{y_2},t)\chi^\dagger_{j;\alpha}(\mathbf{0},0)\Gamma^{(sk)\dagger}_{k,l}(\mathbf{y_1}-\mathbf{y_2})e^{-i\frac{\mathbf{p}}{2}\cdot(\mathbf{y_1}+\mathbf{y_2})} \\ &\quad \times \sum_{\mathbf{x}} \psi_{l;\beta}(\mathbf{y_1},t)\psi^\dagger_{i;\alpha}(\mathbf{x},0)\Gamma^{(sc)}_{i,j}(\mathbf{x})e^{i\frac{\mathbf{p}}{2}\cdot\mathbf{x}}|0,t=0\rangle_H. \end{aligned} \tag{2.100}$$

Since the quark and antiquark propagators are given by

$$
\begin{aligned}
G_{i,j;\alpha,\beta}(\mathbf{y},t;\mathbf{x},0) &= {}_H\langle 0,t=t|\psi_{i;\alpha}(\mathbf{y},t)\psi^{\dagger}_{j;\beta}(\mathbf{x},0)|0,t=0\rangle_H, & (2.101)\\
G^{A}_{i,j;\alpha,\beta}(\mathbf{y},t;\mathbf{x},0) &= {}_H\langle 0,t=t|\chi_{i;\alpha}(\mathbf{y},t)\chi^{\dagger}_{j;\beta}(\mathbf{x},0)|0,t=0\rangle_H & (2.102)
\end{aligned}
$$

and since $G^A = G^*$, (2.100) can be written as

$$
\begin{aligned}
&\sum_{\mathbf{y_1},\mathbf{y_2}} G^*_{k,j;\beta,\alpha}(\{U\},\mathbf{y_2},t;\mathbf{0},0)\Gamma^{(sk)\dagger}_{k,l}(\mathbf{y_1}-\mathbf{y_2})e^{-i\frac{\mathbf{p}}{2}\cdot(\mathbf{y_1}+\mathbf{y_2})}\\
&\qquad\sum_{\mathbf{x}} G_{l,i;\beta,\alpha}(\{U\},\mathbf{y_1},t;\mathbf{x},0)\Gamma^{(sc)}_{i,j}(\mathbf{x})e^{i\frac{\mathbf{p}}{2}\cdot\mathbf{x}} \qquad (2.103)
\end{aligned}
$$

where it has been made explicit that in practice the propagators are not averaged over gauge configurations (unlike equation (1.114)) but instead are calculated for each gauge configuration of an ensemble $\{U\}$.

Interpreting the quark propagator as an operator, it will be noticed that the right hand part of the last equation,

$$
\sum_{\mathbf{x}} G(\{U\},\mathbf{y_1},t;\mathbf{x},0)\Gamma^{(sc)}(\mathbf{x})e^{i\frac{\mathbf{p}}{2}\cdot\mathbf{x}}, \qquad (2.104)
$$

is by Huygen's principle the propagation of the source term $\Gamma^{(sc)}(\mathbf{x})e^{i\frac{\mathbf{p}}{2}\cdot\mathbf{x}}$ to the point $\mathbf{y_1}$ at time t [26, 41]. This smeared propagator, denoted by $\tilde{G}$, can be obtained directly by replacing the initial condition (2.84) with

$$
\tilde{G}(\{U\},\mathbf{x},0) = \Gamma^{(sc)}(\mathbf{x})e^{i\frac{\mathbf{p}}{2}\cdot\mathbf{x}}. \qquad (2.105)
$$

The meson correlation can therefore be written as

$$
\begin{aligned}
&\sum_{\mathbf{y_1},\mathbf{y_2}} G^*_{k,j;\beta,\alpha}(\{U\},\mathbf{y_2},t;\mathbf{0},0)\Gamma^{(sk)\dagger}_{k,l}(\mathbf{y_1}-\mathbf{y_2})e^{-i\frac{\mathbf{p}}{2}\cdot(\mathbf{y_1}+\mathbf{y_2})}\tilde{G}_{l,j;\beta,\alpha}(\{U\},\mathbf{y_1},t;\mathbf{x},0)\\
=&\sum_{\mathbf{y_1},\mathbf{y_2}} \mathrm{Tr}\left\{G^{\dagger}(\{U\},\mathbf{y_2},t;\mathbf{0},0)\Gamma^{(sk)\dagger}(\mathbf{y_1}-\mathbf{y_2})\tilde{G}(\{U\},\mathbf{y_1},t;\mathbf{x},0)\right\}e^{-i\frac{\mathbf{p}}{2}\cdot(\mathbf{y_1}+\mathbf{y_2})}
\end{aligned}
$$

(2.106)

where the trace is taken over both spin and colour indices. In practice, the convolution (2.106) is calculated for each gauge configuration of an ensemble $\{U\}$ using fast Fourier transforms and the average meson correlation is found from

$$\frac{1}{N_{conf}}\sum_{i=1}^{N_{conf}}\sum_{\mathbf{y_1},\mathbf{y_2}}\mathrm{Tr}\left\{G^{\dagger}(\{U\}_i,\mathbf{y_2},t;\mathbf{0},0)\Gamma^{(sk)\dagger}(\mathbf{y_1}-\mathbf{y_2})\tilde{G}(\{U\}_i,\mathbf{y_1},t;\mathbf{x},0)\right\}$$
$$\times e^{-i\frac{\mathbf{p}}{2}\cdot(\mathbf{y_1}+\mathbf{y_2})}. \qquad (2.107)$$

2.7.1 Lattice meson operators

Before discussing the operators used to create particular meson channels, it is necessary to be able to name these channels. Conventionally, a meson state with spin S, orbital angular momentum L and total angular momentum J is labelled by ${}^{2S+1}L_J$. Of these three quantum numbers, only the total angular momentum J is conserved. However two other quantum numbers, the intrinsic parity P and the charge conjugation C which are given for mesons by $P = (-1)^{L-1}$ and $C = (-1)^{L+S}$, are conserved and so as an alternative, meson states can be labelled by J^{PC}. Immediately then it will be noticed that states with the same J^{PC}, for example the ${}^3S_1$ and ${}^3D_1$, will mix with each other, however investigation of this effect is beyond the scope of this thesis.

Various types of meson operators have been used in the past [18, 23, 25]. For the work of this thesis, the meson operators were formed from two individual operators, Ω and $\phi(r)$, Ω being a matrix in spin space incorporating derivatives acting on the radial smearing function $\phi(r)$, such that

$$\Gamma(\mathbf{x}) = \Omega\phi(|\mathbf{x}|). \qquad (2.108)$$

Essentially, the job of the radial smearing function $\phi(r)$ is to create states with differing principal (or energy) quantum number n, while the job of the operator Ω is to create states with the specified quantum numbers S, L and J. The types

Meson state $^{2S+1}L_J$ (J^{PC})	Lattice Representation	Ω
$^1S_0$ (0^{-+})	A_1^{-+}	I
$^3S_1$ (1^{--})	$T_{1(i)}^{--}$	σ_i
$^1P_1$ (1^{+-})	$T_{1(i)}^{+-}$	Δ_i
$^3P_0$ (0^{++})	A_1^{++}	$\sum_j \Delta_j \sigma_j$
$^3P_1$ (1^{++})	$T_{1(k)}^{++}$	$\Delta_i\sigma_j - \Delta_j\sigma_i$
$^3P_2$ (2^{++})	$E_{(k)}^{++}$	$\Delta_i\sigma_i - \Delta_j\sigma_j$
	$T_{2(ij,i\neq j)}^{++}$	$\Delta_i\sigma_j + \Delta_j\sigma_i$

Table 2.2: Various Υ meson states, their lattice cubic group representations and the operators used to create these states.

of $\phi(r)$ used are discussed in the next section, while the types of operator Ω used to create various states are shown in table (2.2) along with the lattice cubic group representations of these states [26].

For instance to create the $^3S_1$ state where $L = 0$, $S = 1$ and $J = 1$, in order to keep $L = 0$ it is required that no derivatives act on the spherically symmetric smearing function, while to give $S = 1$, the Pauli spin matrices are used where

$$\boldsymbol{\sigma} = (\sigma_x, \sigma_y, \sigma_z) \tag{2.109}$$

and

$$\sigma_x = \begin{pmatrix} 0 & 1 \\ 1 & 0 \end{pmatrix}, \quad \sigma_y = \begin{pmatrix} 0 & -i \\ i & 0 \end{pmatrix}, \quad \sigma_z = \begin{pmatrix} 1 & 0 \\ 0 & -1 \end{pmatrix}. \tag{2.110}$$

Having the vector $\boldsymbol{\sigma}$ ensures that $J = 1$. On the other hand, the individual polarizations of the $^3S_1$ state; ^3S_1x, ^3S_1y and ^3S_1z can be projected by using the individual Pauli spin matrices σ_x, σ_y and σ_z respectively.

As another example, the $^1P_1$ state where $L = 1$, $S = 0$ and $J = 1$ requires no spin matrices since $S = 0$. However to obtain $L = 1$, a derivative is required to act on the spherically symmetric smearing function in order to obtain the familiar P state lobes (see next section for the way in which this is done). These derivatives; Δ_x, Δ_y and Δ_z together form a vector ensuring $J=1$, while in a similar manner to the $^3S_1$ state, the individual polarizations of the $^1P_1$ state; ^1P_1x, ^1P_1y and ^1P_1z can be projected by using appropriate individual derivatives.

2.7.2 Radial smearing functions

For the work of this thesis, smearings were required to reproduce ground, first and second excited S states and ground and first excited P states. These smearings are denoted by n_{sc} or n_{sk}, depending on whether the smearing is at the source or sink. $n_{sc}=1$ denotes a ground state smearing, $n_{sc}=2$ denotes a first excited state smearing and so on with $n_{sc}=loc$ denoting a delta function (local) smearing.

Smearings for the S states, at integral values of the radius from the origin r, were obtained using a Richardson potential model [42] and values in between were obtained using linear interpolation. These smearing functions are shown in the left hand plot of figure (2.1) where it can be seen that they mimick well the behaviour of the typical Laguerre polynomial functions associated with non-relativistic systems in a Coulomb potential (see for instance [43]).

For P states, the derivatives acting on the radial functions were not explicitly included in the Ω operators as suggested in table (2.2). Instead, symmetric smearing values $\phi(r)$, at integral values of the radius from the origin r, were obtained using the same Richardson potential model as above [42] and centred differences of these values were taken to produce $\mathrm{d}\phi/\mathrm{d}r$ values at integral values of r. The smearings used for P states; $\partial\phi/\partial x$, $\partial\phi/\partial y$ and $\partial\phi/\partial z$ were subsequently obtained by linearly interpolating the $\mathrm{d}\phi/\mathrm{d}r$ values and multiplying by $\partial r/\partial x$, $\partial r/\partial y$ or $\partial r/\partial z$ as appropriate. Shown in the right hand plot of figure (2.1), are the symmetric smearing functions $\phi(r)$ which behave as expected for P states of non-relativistic systems.

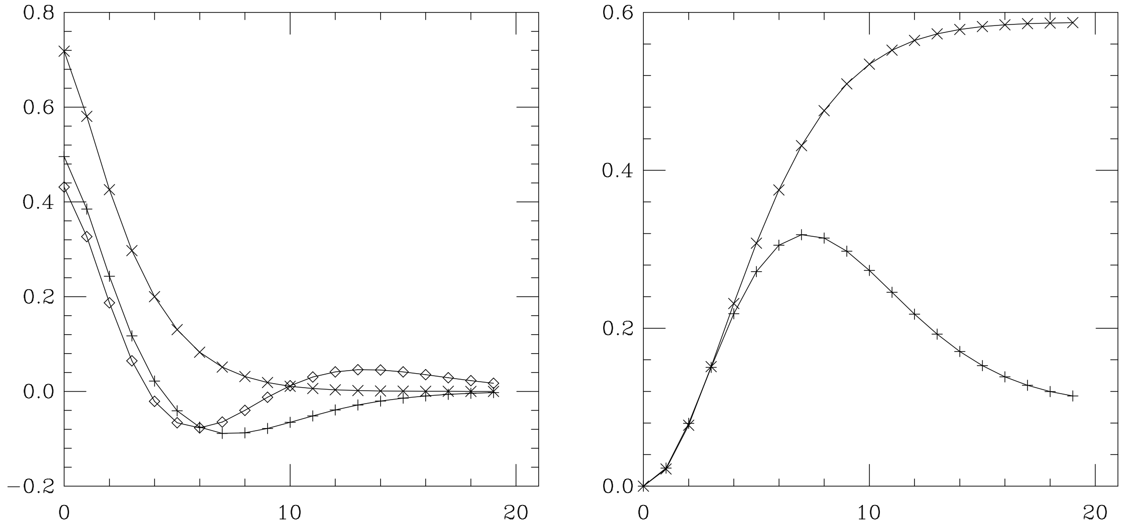

Figure 2.1: Symmetric smearing functions $\phi(r)$ for S states (left figure) and for P states (right figure). Ground and first excited smearings are denoted by crosses and plusses respectively, while the second excited S smearing is denoted by diamonds.

For the $\beta = 6.0$ simulations of chapter 3, statistics were increased by simulating Υ mesons at eight equally spaced spatial origins and four equally spaced starting timeslices on each gauge configuration, however on separate runs. This was made possible by the fact that the Υ is so small and so negligible correlation is incurred in results from different origins and different starting timeslices on the same gauge configuration. The simulation results were then binned over starting timeslices giving an overall eightfold increase in statistics. CPU time was also saved for the $\beta = 6.0$ simulations by setting the initial quark and antiquark source spins to be 1.

For the $\beta = 6.2$ simulations of chapter 5, the initial quark and antiquark source spins were similarly set to 1 to save CPU time. Eight spatial origins were also used to obtain an eightfold increase in statistics, however a method different to that of above was employed to do this saving CPU time. This new method [44] involved the generation of eight random numbers for each configuration, $\eta_i(\{U\}_j)$, $i = 1, \ldots, 8$, which were equally likely to assume the values 1 or -1. Sums of eight delta functions or eight source smearings were then formed with each delta function or source smearing centred at one of eight maximally spaced spatial origins and weighted in the sum by the factor $\eta_i(\{U\}_j)$ corresponding to that particular origin;

$$\Gamma^{(sc)}_{tot}(\mathbf{x}) = \sum_{i=1}^{8} \eta_i(\{U\}_j)\Gamma^{(sc)}(\mathbf{x_i} - \mathbf{x}) \tag{2.111}$$

$$\delta_{tot}(\mathbf{x}) = \sum_{i=1}^{8} \eta_i(\{U\}_j)\delta_{\mathbf{x},\mathbf{x_i}}. \tag{2.112}$$

When propagated, these smearing sums give rise to smeared and quark propagators which are the same weighted sums of the individual smeared and quark propagators;

$$\tilde{G}_{tot}(\{U\}_j) = \sum_{i=1}^{8} \eta_i(\{U\}_j)\tilde{G}_i(\{U\}_j) \tag{2.113}$$

$$G_{tot}(\{U\}_j) \quad = \quad \sum_{i=1}^{8} \eta_i(\{U\}_j) G_i(\{U\}_j). \tag{2.114}$$

Mesons, such as the $^1S_0$, are then composed according to

$$G^\dagger_{tot}(\{U\}_j)\tilde{G}_{tot}(\{U\}_j) = \sum_{i,k=1}^{8} \eta_i(\{U\}_j)\eta_k(\{U\}_j)G^\dagger_i(\{U\}_j)\tilde{G}_k(\{U\}_j) \tag{2.115}$$

$$= \sum_{i=1}^{8} \eta_i^2(\{U\}_j)G^\dagger_i(\{U\}_j)\tilde{G}_i(\{U\}_j) + \sum_{\substack{i,k=1 \\ i\neq k}}^{8} \eta_i(\{U\}_j)\eta_k(\{U\}_j)G^\dagger_i(\{U\}_j)\tilde{G}_k(\{U\}_j) \tag{2.116}$$

The first sum gives the eightfold increase in statistics since $\eta_i^2 = 1$ while the second sum vanishes when averaged over gauge configurations on account of the fact that $\langle \eta_i \eta_j \rangle = 0$. The price for this relatively cheap increase in statistics is paid by the second sum, since although it vanishes when averaged over configurations, it introduces an element of noise on any given configuration.

2.8 Extraction of Energies and Amplitudes from Meson Correlations

When analysed, meson correlation functions provide valuable information such as energies of particular states and amplitudes coupling the correlations to these states. Before looking at multi-correlation fitting, a simple procedure for analysing a single correlation, known as an effective mass plot will be introduced. Before doing this however, the functional form of the meson propagator is investigated.

If $O^\dagger_H(\mathbf{x}, t)$ is an operator creating an Υ meson in a particular channel at position $\mathbf{x}$ and time t in the Heisenberg picture, then the correlation $\sum_{\mathbf{x}} {}_H\langle 0, t = t|O_H(\mathbf{x}, t)O^\dagger_H(\mathbf{0}, 0)|0, t = 0\rangle_H$ represents an Υ meson propagating between the times $t = 0$ and $t = t$. Defining the Euclidean space evolution operator $U = e^{i\mathbf{p}\cdot\mathbf{x}-Ht}$, the correlation can be transformed into the Schrödinger picture as follows

$$\sum_{\mathbf{x}} {}_H\langle 0, t = t | O_H(\mathbf{x}, t) O_H^\dagger(\mathbf{0}, 0) | 0, t = 0 \rangle_H \tag{2.117}$$

$$\rightarrow \sum_{\mathbf{x}} {}_H\langle 0, t = t | U^\dagger O_S U O_S^\dagger | 0, t = 0 \rangle_H \tag{2.118}$$

$$\rightarrow \sum_{\mathbf{x}} {}_S\langle 0, t = t | O_S U O_S^\dagger | 0, t = 0 \rangle_S \tag{2.119}$$

Inserting a complete set of energy eigenstates, $\sum_{m,\mathbf{q}} |m\mathbf{q}\rangle\langle m\mathbf{q}| = 1$ with normalisation $\langle m\mathbf{q}|n\mathbf{p}\rangle = \delta_{m,n}\delta_{\mathbf{q},\mathbf{p}}$, then gives

$$\sum_{\mathbf{x},\mathbf{q},m} {}_S\langle 0, t = t | O_S U | m\mathbf{q}\rangle\langle m\mathbf{q}| O_S^\dagger | 0, t = 0 \rangle_S \tag{2.120}$$

$$= \sum_{\mathbf{x},\mathbf{q},m} {}_S\langle 0, t = t | O_S e^{i\mathbf{q}\cdot\mathbf{x} - E_m t} | m\mathbf{q}\rangle\langle m\mathbf{q}| O_S^\dagger | 0, t = 0 \rangle_S \tag{2.121}$$

$$= \sum_{\mathbf{x},\mathbf{q},m} \left|\langle 0 | O_S | m\mathbf{q}\rangle\right|^2 e^{i\mathbf{q}\cdot\mathbf{x} - E_m t} \tag{2.122}$$

$$= \sum_{\mathbf{q},m} \delta_{\mathbf{q},\mathbf{0}} \left|\langle 0 | O_S | m\mathbf{q}\rangle\right|^2 e^{-E_m t} \tag{2.123}$$

$$= \sum_{m} \left|\langle 0 | O_S | m\rangle\right|^2 e^{-E_m t} \tag{2.124}$$

Hence, the functional form of the meson correlation at time t is a weighted sum of decaying exponentials, each having as its exponent the product of t and the energy E_m of the energy eigenstates $|m\rangle$. The weights are seen to be the square of the modulus of the overlap of the meson state vector $O_S^\dagger|0\rangle$ with the eigenstates $|m\rangle$.

Since $E_1 < E_2 < E_3 < \ldots$, contributions from high energy eigenstates decay faster than those from lower energy eigenstates and so for large enough t values, it should be possible to see correlations falling off as the resulting ground state decaying exponential thereby allowing the ground state energy to be isolated—this is the idea behind the effective mass plot. Defining the effective mass function as

$$m_{eff}(t) = -\ln\left(\frac{G(t+1)}{G(t)}\right) \tag{2.125}$$

and plotting this against time t, a plateau at large time values is obtained having the value of the ground state energy. Examples are shown in chapters 3 and 5 where effective mass plots are used to determine how well the smearing functions are working and also to obtain estimates of input parameters for more sophisticated correlation analysis routines.

2.8.1 Multi-correlation fitting routines

The effective mass function is a naive but effective model. However a better method of determining the ground and subsequent excited state energies is obtained by fitting to more than one correlation simultaneously, constraining the energy parameters for each of the radial excitations to have the same value, and by assigning errors to the correlation data-points thereby allowing an assessment of the quality of the fit. This improved method[3], described in [26, 25, 45], involves fitting correlation data to one of two functional forms; the functional form for a matrix fit is given by

$$C_{theo}(n_{sc}, n_{sk}; t) = \sum_{k=1}^{N_{exp}} a(n_{sc}, k) a^*(n_{sk}, k) e^{-E_k t} \tag{2.126}$$

where the smearing numbers n_{sc} and n_{sk} at the source and sink have been identified while the functional form for a row fit is given by

$$C_{theo}(n_{sc}, loc; t) = \sum_{k=1}^{N_{exp}} b(n_{sc}, k) e^{-E_k t} \tag{2.127}$$

Typically the group of correlations used for the matrix fit have (n_{sc}, n_{sk}) given by $(1,1)$, $(1,2)$, $(2,1)$ and $(2,2)$ while those used for the row fit have (n_{sc}, loc) given by $(1, loc)$, $(2, loc)$, $(3, loc)$, ... In the limit of an infinite number of exponentials, comparison of (2.126) with (2.124) yields the identification

$$a(n_{sc}, k) = \langle k|O^\dagger_{sc}|0\rangle \quad \text{and} \quad a(n_{sk}, k) = \langle k|O^\dagger_{sk}|0\rangle \tag{2.128}$$

[3]The improved method described here is used even if fitting to only one correlation.

while putting $n_{sk} = loc$ in (2.126) gives the relation[4]

$$b(n_{sc}, k) = a(n_{sc}, k)a(loc, k) \tag{2.129}$$

Taking account of the correlation between data-points from different meson correlations as well as the correlation from different time values, the chi-square function for the multi-correlation fitting is defined as

$$\chi^2 = \sum_{\substack{1<\alpha,\beta<N_{corr} \\ t_{min}<t,t'<t_{max}}} \left(C^{\alpha}_{theo}(t;a_i) - \langle C^{\alpha}(t)\rangle\right) (\sigma^2)^{-1}_{\alpha\beta}(t,t') \left(C^{\beta}_{theo}(t';a_i) - \langle C^{\beta}(t')\rangle\right) \tag{2.130}$$

where different meson correlations are represented by the α and β indices and $\langle\rangle$ denotes the average over gauge configurations. Here C_{theo} can be either of the matrix or row types, equations (2.126) and (2.127) respectively, and a_i denotes the fitting parameters $a(1,1), \ldots$ (or $b(1,1), \ldots$), $E_1, E_2, \ldots$. The matrix $\sigma^2_{\alpha\beta}(t,t')$ is known as the covariance matrix and for $\alpha = \beta$ and $t = t'$, measures the likely error on each of the data-points from statistical fluctuations. It is defined by

$$\sigma^2_{\alpha\beta}(t,t') = \frac{1}{N_{conf}} \sum_{i=1}^{N_{conf}} \left(C_{\alpha}(t) - \langle C_{\alpha}(t)\rangle\right) \left(C_{\beta}(t') - \langle C_{\beta}(t')\rangle\right) \tag{2.131}$$

where N_{conf} is the number of gauge configurations.

The procedure for obtaining the best fit is as follows; initial guesses for the parameters are given and χ^2 is calculated. It is then minimised by varying each of the parameters using routines detailed in [46] until the χ^2 per degree of freedom is less than or close to one. In calculating χ^2, it is necessary to invert the covariance matrix. This is a square matrix whose side is $N_{corr} \times N_t$, N_{corr} being the number of correlations in the simultaneous fit and N_t being the time range over which fitting takes place. Provided that the number of gauge configurations

[4] The amplitudes can be chosen to be real, hence the omission of the *.

N_{conf} is much greater than $N_{corr} \times N_t$, the covariance matrix will in general be invertible. However if this is not so, or if the eigenvalues of the covariance matrix become smaller than the machine precision, singular value decomposition routines, detailed in [46], are used to invert a submatrix instead.

Once the χ^2 is minimised, errors on the fitting parameters are determined such that the value of χ^2 is shifted by one from its minimum value—i.e. shifted to the edge of the one sigma confidence region. If a_i^{fit} are the values of the fitting parameters at χ^2_{min}, then Taylor expanding χ^2 about these values (with implicit summation over j and k indices) gives

$$\begin{aligned} \Delta\chi^2 &= \chi^2(a_i^{fit} + \Delta a_i) - \chi^2_{min}(a_i^{fit}) \\ &= \chi^2_{min}(a_i^{fit}) + \Delta a_j \left.\frac{\partial \chi^2}{\partial a_j}\right|_{a_i^{fit}} + \frac{1}{2}\Delta a_j \Delta a_k \left.\frac{\partial^2 \chi^2}{\partial a_j \partial a_k}\right|_{a_i^{fit}} - \chi^2_{min}(a_i^{fit}) \\ &= \frac{1}{2}\Delta a_j \Delta a_k \left.\frac{\partial^2 \chi^2}{\partial a_j \partial a_k}\right|_{a_i^{fit}} \end{aligned} \tag{2.132}$$

since χ^2 is minimised at $a_i = a_i^{fit}$. There then exists sets of Δa_i values for which $\Delta\chi^2 = 1$ and infinitesimal changes in Δa_i, $i \neq j$ still allow $\Delta\chi^2 = 1$ while an infinitesimal change in Δa_j shifts $\Delta\chi^2$ from 1. From each of these sets of values, the error on parameter j is taken to be $\sigma_j \equiv \Delta a_j$.

Finally, a measure of the quality of fit (or goodness of fit), Q, can be determined using routines in [46] and is generally a function of both χ^2 and the number of degrees of freedom. The quality of fit determines the probability that the χ^2_{min} obtained occurred by chance and so a value greater than 0.1 is generally desired in order that the fit be acceptable. Values less than 0.1 may still be acceptable, however, if it is believed that underestimation of errors or some other systematic error has occurred.

Bootstrap multi-correlation row and matrix fitting routines can also be used to determine fitting parameters and their associated errors. These routines involve the preparation of many, say one hundred, Monte Carlo ensembles of gauge configurations, with replacement, from the original ensemble such that the new ensembles are the same size as the original. Subsequent fitting to these new ensembles with the optimal parameters obtained from the ordinary row and matrix fits is undertaken yielding one hundred values for the ground state energy, one hundred values for the first excited state energy and so on. From the set of values of a given parameter, a better statistical estimate can be obtained for both the parameter and its error by taking the mean and the standard error. This bootstrap method also enables better determinations to be made of ratios of splittings, such as the ratio of the $2S - 1S$ splitting to the $1P - 1S$ splitting (see chapter 6). For instance, from the sets of a hundred values of the parameters $1S$, $2S$ and $1P$, a hundred values of the ratio $2S - 1S\ /1P - 1S$ can be made and so the mean and standard error of this set give a better statistical estimate for this quantity since most of the correlation between the states is removed by preparing the set of ratios in this way.

Chapter 3

Upsilon Spectroscopy at $\beta = 6.0$

Following the arguments of chapter 2, a lattice suitable for simulating the Υ meson should have a lattice spacing small enough to be able to see the length scale associated with the typical quark momentum, $\mathcal{O}(1/Mv) \sim 0.15\,\text{fm}$, and should have a side length large enough to be able to see the length scale associated with the typical quark kinetic energy, $\mathcal{O}(1/Mv^2) \sim 0.48\,\text{fm}$. The lattice spacing should also be small enough so as to minimise lattice spacing errors to the Lagrangian, discussed in section 2.6.2 which are $\mathcal{O}(a^2M^3v^4)$ and $\mathcal{O}(aM^2v^4)$, in particular higher order lattice spacing errors, which are neglected, must be smaller than the lowest order relativistic corrections, which are included, i.e.

$$a^4M^5v^6 < a^2M^3v^4 \tag{3.1}$$

and so aM must be less than 1.8. However the lattice spacing should not be too small since this would cause the perturbative expansions of the coupling constants, discussed in section 2.6.4, to be divergent. A compromise is to choose $a \sim 1/M$. Since $M_b \sim M_b^0 \sim 4.1$ GeV (see for instance [27]), the inverse lattice spacing should be around 4.1 GeV for b quarks. The lattices that were actually used for the work in this thesis have β values of 6.0 and 6.2 and so are expected to have inverse lattice spacings of between 2.4 to 3.3 GeV, equivalent to lattice spacings of 0.06 $\sim$ 0.08 fm. They also have side lengths of around 1.4 fm and so meet all the criteria needed for Υ simulation.

The work in this chapter was performed on $16^3 \times 32$ lattices at $\beta = 6.0$. 149 quenched configurations using the standard Wilson gluonic action [47] were used, gauge fixed to Coulomb gauge, with simulations beginning on 8 different origin sites and 4 different starting timeslices per configuration as described in section 2.7.2. Equation (2.82), discussed in section 2.6.3, was used to evolve the quark propagators.

3.1 Tuning the Bare Quark Mass

Mentioned in chapter 2, the parameters of the NRQCD theory must be tuned to match experiment. The lattice spacing $a(g)$ is dealt with in section 3.5 while the bare quark mass M_b^0 is dealt with here.

While there is much evidence to show that spin-independent splittings such as $1P - 1S$ do not depend strongly on the bare heavy quark mass in NRQCD theory [26, 31, 32], clearly the spin-dependent splittings do—indeed the hyperfine splitting ($^3S_1 - {}^1S_0$) seems to be inversely proportional to M_b^0 (see for example [26]), so it is vital to tune this mass to its correct value.

As described in [26], the method for tuning the bare quark mass involves two simulations of the Υ—one with small momentum, the other with zero momentum—in the $^3S_1$ channel. The difference between these non-relativistic energies is equated to the kinetic energy of the dynamical meson,

$$E_\Upsilon(\mathbf{p}) - E_\Upsilon(\mathbf{0}) = \frac{\mathbf{p}^2}{2M_{kin}} \tag{3.2}$$

and hence the mass obtained, known as the kinetic mass, is matched to the experimental Υ rest mass value of 9.46 GeV[1]. This was done in [26] and a dimensionless bare b quark mass of $aM_b^0 = 1.71$ was found to give a kinetic Υ mass of 3.94(3)

[1] To do this requires multiplying the kinetic mass by a value for the inverse lattice spacing

which when multiplied by $a^{-1} = 2.4(1)\,\mathrm{GeV}$ (determined in [26]) gives $9.5(4)\,\mathrm{GeV}$, i.e. equal to the experimental value within error. Since the simulations in [26] had a β value of 6.0, $aM_b^0 = 1.71$ was considered appropriate for the simulations in this chapter.[2]

3.2 Fitting Results for S and P States

In this section the multi-correlation fitting procedures of the section 2.8.1 have been applied to extract values for the ground and first excited states of the ${}^1S_0$, ${}^3S_1$ and ${}^1P_1$ and for a second excited state of the ${}^3S_1$. The procedure followed was to use effective mass plots as a preliminary guide to the quality of the data and to determine expected values for input fitting parameters. Then the multi-correlation routines were used to extract accurate values of the energies and amplitudes. Occasionally t_{min} plots[3] were used to determine a plateau in one particular energy or amplitude.

In figure (3.1) effective masses are plotted against time t for all possible (source, sink) combinations of the ${}^3S_1$ state. The (loc,1), (1,loc) and (1,1) plots have very good plateaux indicating good ground state smearing. The (loc,2), (1,2), (2,loc) and (2,1) plots rise sharply, indicating the sharp decay of a prominent excited state, then switch to low values before terminating in good ground state plateaux. The near zero effective mass values indicate a flat region of the propagator, which is explained by the results in table (3.14) where it can be seen that the ground state amplitudes for $n_{sc} = 2$ are negative while those for the excited state ($m = 2$) are positive. Hence the rising ground state and the decaying excited state have

which, because it is obtained from spin-independent splittings, depends very weakly on the bare heavy quark mass as must be the case to enable the mass tuning to be practicable.

[2] The simulations of this chapter are intended to be more accurate than those previously undertaken in [26].

[3] t_{min} plots have one particular parameter, obtained from multi-correlation fits by varying the value of t_{min} keeping t_{max} constant, plotted against this value of t_{min}.

a cancelling effect. The (2,2) plot has a steady excited state plateau, masked at later time by noise.

Similar plots for the $^1P_1$ state are shown in figure (3.2). Good ground state plateaux can be seen in the (loc, loc), (loc,1), (1,loc) and (1,1) plots, while reasonably good excited state plateaux were obtained for the (loc,2), (2,loc) and (2,2) combinations.

Multi-correlation fitting routines were used to extract energies and amplitudes for the $^1S_0$, $^3S_1$ and $^1P_1$ states. Table (3.1) shows results obtained from row fits to the $^1S_0$ ground and excited state energies over various t_{min}/t_{max} ranges as well as the quality of fit, Q. For the upper part of the table, two correlation functions with $(n_{sc}, n_{sk}) = (1, loc)$ and $(2, loc)$ were fitted to both a two exponential ansatz and a three exponential ansatz in turn. It can be seen that the ground state mass obtained is very accurate and steady and that the addition of the third exponential allows for a more accurate determination of the first excited state mass by removing any contamination from higher excited states. The Q value of 0.15 corresponding to $t_{min} = 8$ indicates a particularly good fit and for this reason the ground state mass value was taken at this t_{min}. For the lower part of the table a third correlation with $(n_{sc}, n_{sk}) = (3, loc)$ was added allowing a determination of the second excited state. However what is interesting is the fact that fitting to three correlations gave first excited state masses that are about one sigma lower than those obtained from the two correlation fits. Although one sigma is not statistically significant, it was decided to average results from both groups. With the best Q values, the $t_{min} = 8$ result for the two correlation case and the $t_{min} = 6$ result for the three correlation case give an average of 0.684(8), taken for the first excited state mass.

Table (3.2) shows similar results obtained from matrix fits to four $^1S_0$ correlations with $(n_{sc}, n_{sk}) = (1, 1), (1, 2), (2, 1)$ and $(2, 2)$. Obtaining decent Q values for the matrix fits was found to be more difficult than for the row fits and so for this reason the time range over which fitting took place was reduced some-

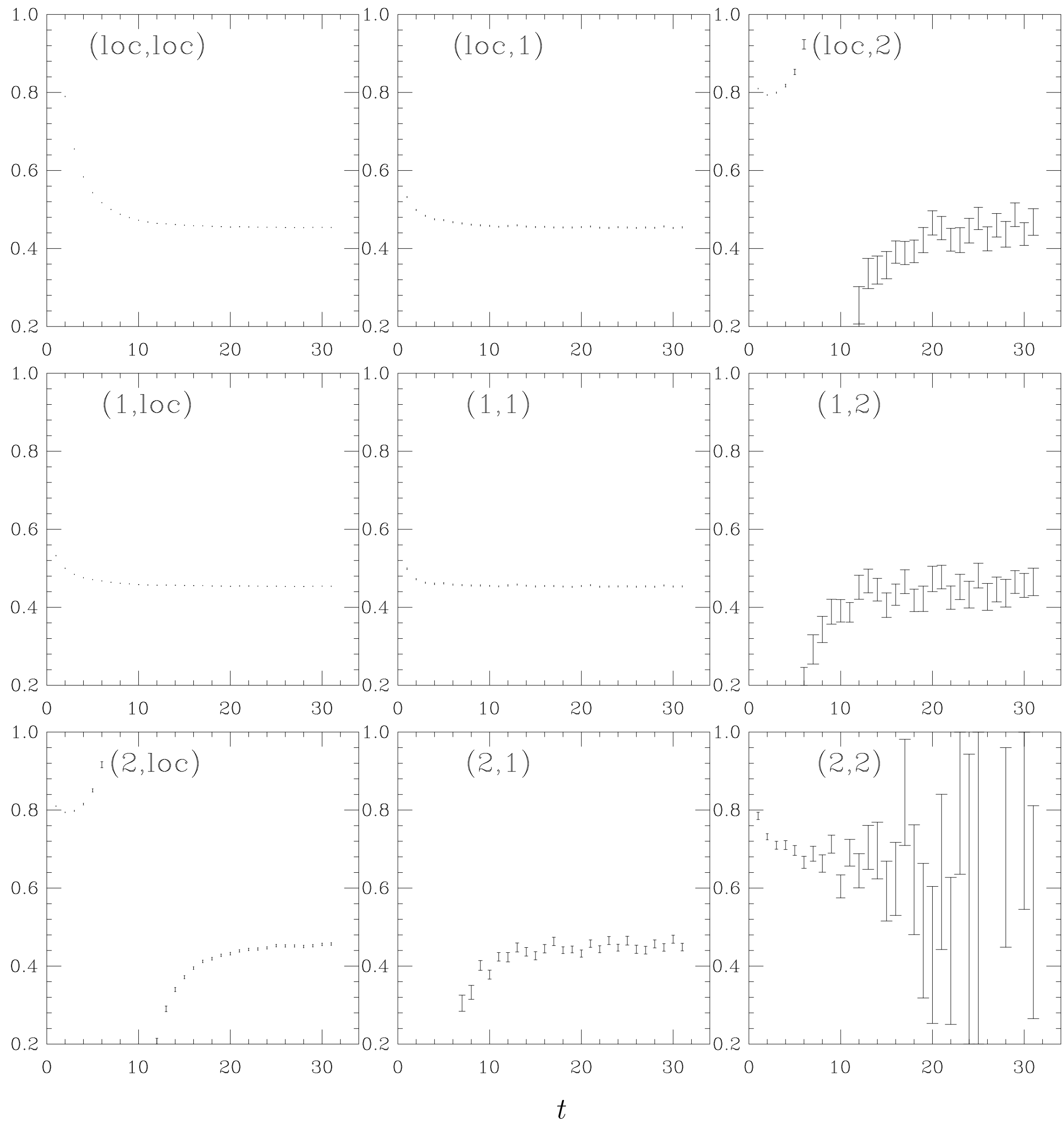

Figure 3.1: Effective masses of $^3S_1$ states given by their smearings, (n_{sc}, n_{sk}).

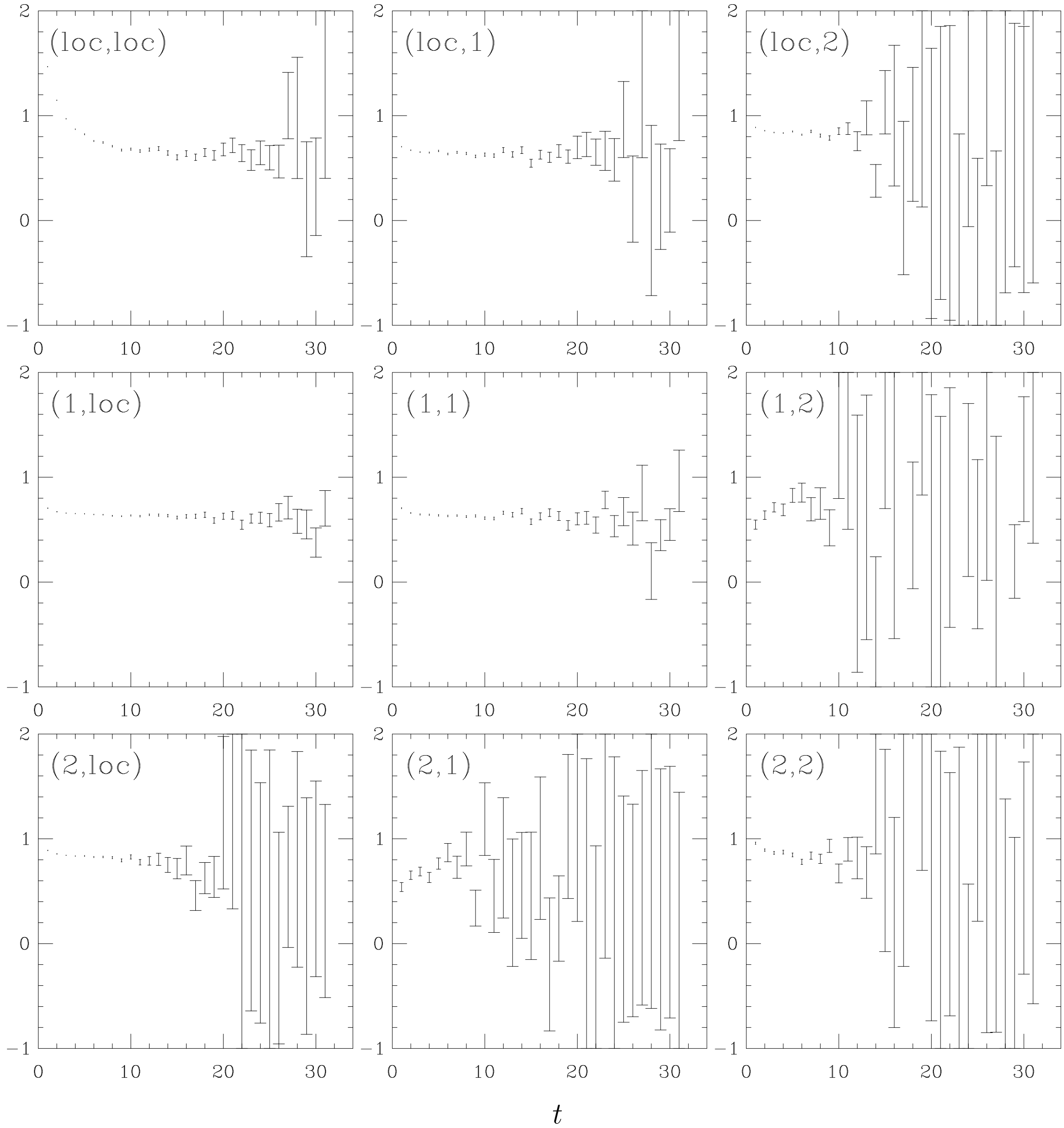

Figure 3.2: Effective masses of $^1P_1$ states given by their smearings, (n_{sc}, n_{sk}).

	N_{exp}	t_{min}/t_{max}	aE_1	aE_2	aE_3	Q
fits to (1,loc)	2	8/32	0.4416(2)	0.696(4)		0.10
and (2,loc)		9/32	0.4416(2)	0.688(5)		0.18
correlations		10/32	0.4417(2)	0.687(6)		0.14
		11/32	0.4416(2)	0.682(7)		0.13
		12/32	0.4416(2)	0.677(9)		0.11
		13/32	0.4415(2)	0.688(11)		0.20
		14/32	0.4415(2)	0.690(15)		0.16
	3	3/32	0.4417(2)	0.701(4)	1.5(3)	1×10^{-2}
		4/32	0.4416(2)	0.697(7)	1.4(5)	0.14
		5/32	0.4416(2)	0.695(5)	1.5(9)	0.14
		6/32	0.4416(2)	0.694(2)	1.5(5)	0.13
		7/32	0.4416(2)	0.689(5)	1.5(3)	0.10
		8/32	0.4416(2)	0.686(8)	1.5(2)	0.15
		9/32	0.4416(2)	0.683(8)	1.5(2)	0.11
fits to (1,loc),	3	4/32	0.4415(2)	0.681(5)	0.881(7)	0.12
(2,loc) and		5/32	0.4415(2)	0.681(6)	0.877(10)	0.15
(3,loc)		6/32	0.4416(2)	0.681(8)	0.871(13)	0.17
correlations		7/32	0.4416(2)	0.674(8)	0.920(21)	0.14
		8/32	0.4416(2)	0.675(11)	0.921(33)	0.16

Table 3.1: Examples of simultaneous row fits to two and three ${}^1S_0$ correlations.

	N_{exp}	t_{min}/t_{max}	aE_1	aE_2	Q
fits to (1,1)	2	5/16	0.4427(3)	0.683(3)	8×10^{-2}
(1,2),(2,1)		5/24	0.4421(2)	0.682(3)	4×10^{-2}
and (2,2)		5/32	0.4418(2)	0.681(2)	6×10^{-3}
correlations		6/16	0.4425(3)	0.682(4)	0.24
		6/24	0.4420(2)	0.681(3)	0.14
		6/32	0.4418(2)	0.681(3)	4×10^{-2}
		7/16	0.4425(3)	0.686(5)	0.27
		7/24	0.4420(2)	0.684(4)	0.13
		7/32	0.4418(2)	0.684(4)	5×10^{-2}
		8/16	0.4424(4)	0.684(6)	0.22
		8/24	0.4419(3)	0.682(5)	0.13
		8/32	0.4417(2)	0.682(5)	6×10^{-2}

Table 3.2: Examples of simultaneous 2×2 matrix fits to $^1S_0$ correlations.

what. The values for the first excited mass are within one or two sigma of the corresponding row fit values and the 0.684(8) value taken from the row fit table easily encompasses all the matrix fit values. The ground state masses differ from those of the row fit by one sigma for $t_{max} = 32$, two sigma for $t_{max} = 24$ and three sigma for $t_{max} = 16$. This is not entirely unexpected since fitting over a smaller time range allows more flexibility in the functional form being fitted to and so the results obtained are therefore less trustworthy. For this reason, the ground state mass obtained from the row fit was taken as the best determination.

Results from similar row fit analyses to the $^3S_1$ ground and excited state energies are shown in table (3.3). The upper part of the table reveals an accurate and steady ground state mass and the addition of the third exponential, by removing higher excited state contamination, yields a steady first excited state mass. In particular, with $N_{exp} = 3$ and $t_{min} = 4, 5$ and 6, the Q values are relatively good and so a value for the ground state mass was taken from here. For the lower part of table (3.3) a correlation with $(n_{sc}, n_{sk}) = (3, loc)$ was included allowing a determination of the second excited state, a value for which was taken at $t_{min} = 5$. As was the case for the $^1S_0$ state, the three correlation fits gave first excited state masses that are about one sigma lower than those obtained from the two correlation fits. Similarly to the $^1S_0$ case, it was decided to average results from both groups with the best Q values; the $t_{min} = 4$ result for the two correlation case and the $t_{min} = 5$ result for the three correlation case give an average of 0.695(9) and so this was taken as the best determination of the first excited state mass. Tables (3.4) and (3.5) show results from similar row and matrix fit analyses applied to $^1P_1$ correlations. Both the matrix and row fits are in excellent agreement over the ground state mass value while a one to two sigma difference exists between corresponding first excited state masses. The Q values in table (3.4) for $N_{exp} = 2$ and t_{min} of 6 onwards are particularly good and so the ground state mass was taken from here. Likewise, the Q values for $N_{exp} = 3$ and t_{min} of 4 onwards are good allowing a determination of the first excited state mass.

	N_{exp}	t_{min}/t_{max}	aE_1	aE_2	aE_3	Q
fits to (1,loc)	2	5/32	0.4540(2)	0.717(2)		2×10^{-3}
and (2,loc)		6/32	0.4539(2)	0.710(3)		0.14
correlations		7/32	0.4539(2)	0.708(3)		0.14
		8/32	0.4539(3)	0.705(4)		0.13
		9/32	0.4539(3)	0.701(5)		0.15
		10/32	0.4539(3)	0.697(6)		0.14
		11/32	0.4539(3)	0.690(7)		0.14
		12/32	0.4538(3)	0.682(10)		0.13
		13/32	0.4537(3)	0.691(12)		0.30
		14/32	0.4537(3)	0.698(16)		0.24
	3	2/32	0.4541(2)	0.699(6)	1.11(6)	7×10^{-2}
		3/32	0.4539(3)	0.700(7)	1.1(1)	0.16
		4/32	0.4538(3)	0.699(9)	1.1(2)	0.21
		5/32	0.4538(3)	0.697(15)	1.1(4)	0.17
		6/32	0.4539(3)	0.698(12)	1.1(5)	0.18
fits to (1,loc),	3	3/32	0.4538(2)	0.683(3)	0.932(5)	3×10^{-2}
(2,loc) and (3,loc)		4/32	0.4538(3)	0.690(5)	0.901(7)	0.12
correlations		5/32	0.4538(3)	0.690(6)	0.900(10)	0.16
		6/32	0.4539(3)	0.683(8)	0.881(14)	0.19

Table 3.3: Examples of simultaneous row fits to two and three $^3S_1$ correlations.

	N_{exp}	t_{min}/t_{max}	aE_1	aE_2	aE_3	Q
fits to (1,*loc*)	2	3/32	0.628(2)	0.858(3)		3×10^{-2}
and (2,*loc*)		4/32	0.626(2)	0.850(4)		0.33
correlations		5/32	0.624(2)	0.847(5)		0.37
		6/32	0.626(3)	0.845(7)		0.42
		7/32	0.626(3)	0.850(11)		0.35
		8/32	0.628(4)	0.860(17)		0.33
		9/32	0.626(4)	0.84(2)		0.36
		10/32	0.625(5)	0.84(3)		0.28
		11/32	0.619(6)	0.82(4)		0.34
	3	2/32	0.625(3)	0.81(2)	1.11(12)	0.15
		3/32	0.622(3)	0.839(11)	1.11(14)	0.22
		4/32	0.623(3)	0.839(12)	1.1(5)	0.26
		5/32	0.628(4)	0.84(2)	1.1(4)	0.34
		6/32	0.626(2)	0.85(3)	1.1(14)	0.31

Table 3.4: Examples of simultaneous row fits to two $^1P_1$ correlations.

	N_{exp}	t_{min}/t_{max}	aE_1	aE_2	Q
fits to (1,1)	2	4/16	0.6317(16)	0.834(5)	3×10^{-2}
(1,2),(2,1)		4/24	0.6318(16)	0.835(5)	3×10^{-3}
and (2,2)		5/16	0.6290(18)	0.825(6)	0.24
correlations		5/24	0.6288(17)	0.826(6)	4×10^{-2}
		6/16	0.627(2)	0.814(8)	0.45
		6/24	0.627(2)	0.816(8)	0.11
		7/16	0.629(2)	0.821(11)	0.43
		7/24	0.629(2)	0.825(11)	0.10
		8/16	0.628(3)	0.818(16)	0.30
		8/24	0.628(3)	0.821(15)	7×10^{-2}
		9/24	0.628(3)	0.83(2)	4×10^{-2}
		10/24	0.627(3)	0.81(3)	3×10^{-2}

Table 3.5: Examples of simultaneous 2×2 matrix fits to $^1P_1$ correlations.

state	simulation result	bootstrap result
1^1S_0	0.4416(3)	0.4417(2)
2^1S_0	0.684(8)	0.683(7)
1^3S_1	0.4539(3)	0.4539(2)
2^3S_1	0.695(9)	0.697(5)
3^3S_1	0.90(2)	0.904(7)
1^1P_1	0.627(3)	0.626(3)
2^1P_1	0.84(2)	0.84(1)

Table 3.6: Dimensionless masses.

All the simulation mass results are collected together in table (3.6). Bootstrap row fits were also used on the ${}^1S_0$, ${}^3S_1$ and ${}^1P_1$ states yielding the results in the third column of table (3.6), however the ${}^1S_0$ and ${}^3S_1$ first excited state bootstrap results correspond only to the ordinary row fit values taken from the two correlation cases. The errors and central values are consistent with the ordinary row and matrix fit results, the bootstrap errors being slightly smaller as expected. The one notable exception being the error on the 3^3S_1 result, which for the ordinary row fit, was increased artificially to account for the lack of second excited state fitted energies in the lower part of table (3.3).

3.3 Fitting Results for Spin Splittings

Spin splittings for S and P states arise from terms in the Lagrangian of equation (2.51) which involve the spin $\boldsymbol{\sigma}$, namely

$$-c_3\frac{g}{8(M_b^0)^2}\boldsymbol{\sigma}\cdot(\boldsymbol{\Delta}\times\mathbf{E}-\mathbf{E}\times\boldsymbol{\Delta}) \qquad \text{and} \qquad -c_4\frac{g}{2M_b^0}\boldsymbol{\sigma}\cdot\mathbf{B} \tag{3.3}$$

In particular, as was seen in section 2.1.1, the first term gives rise to the P fine structure while the second accounts for the hyperfine S splitting. An order of magnitude for these terms can be made following the arguments of section 2.4.1. Using tree-level values for the couplings, $c_3 = c_4 = 1$ and putting $\boldsymbol{\sigma} = \frac{1}{2}$ and $M_b^0 \sim M$, the spin terms are evaluated as

$$-c_3 \frac{g}{8(M_b^0)^2} \boldsymbol{\sigma} \cdot (\boldsymbol{\Delta} \times \mathbf{E} - \mathbf{E} \times \boldsymbol{\Delta}) \sim \frac{1}{8(M)^2} \cdot \frac{1}{2} \cdot (Mv)(M^2 v^3) = \frac{Mv^4}{16}$$

$$-c_4 \frac{g}{2M_b^0} \boldsymbol{\sigma} \cdot \mathbf{B} \sim \frac{1}{2M} \cdot \frac{1}{2} \cdot (M^2 v^4) = \frac{Mv^4}{4}$$

Taking the dimensionless mass as $aM = 1.71$ and with $v^2 \sim 0.1$, the first term has a dimensionless order of magnitude 0.001 while that of the second spin term is 0.004. As can be seen from tables (3.4) and (3.5), the typical error for ground state masses for both row and matrix fits is around 0.003/0.005, therefore the conventional row and matrix fitting routines would not be able to distinguish these splittings adequately. To achieve a reduction in fitting errors, jackknife ensembles of ratios of meson correlation functions, with the same orbital angular momentum, were fitted to a single exponential having the form

$$\mathrm{Ratio}(t) = Ae^{-\delta E t} \tag{3.4}$$

where δE is the difference between the ground state energies of both the mesons involved. Known as ratio fitting, this method of fitting to jackknife ensembles bridges the need to take into account statistical correlations from different configurations for each of the meson correlations individually and the need to take into account, for each configuration, statistical correlations between the meson correlations themselves. It is because of this last reason that typical fitting errors are reduced substantially from those that would be expected from a single exponential row fit to an ordinary ensemble of correlation ratios.

Shown in table (3.7) are splitting energies and Q values from ratio fits over various t_{min}/t_{max} ranges to the ${}^3S_1 - {}^1S_0$ hyperfine splitting. The results are

	N_{exp}	t_{min}/t_{max}	$a\delta E$	Q
fits to ratio	1	7/32	0.01264(6)	0.11
of (1,1)		8/32	0.01260(6)	0.23
correlations		9/32	0.01257(7)	0.30
		10/32	0.01251(7)	0.68
		11/32	0.01248(7)	0.73
		12/32	0.01247(8)	0.70
		13/32	0.01244(8)	0.75
		14/32	0.01239(8)	0.90
		15/32	0.01240(9)	0.87
		16/32	0.01237(9)	0.89
		17/32	0.01233(9)	0.96
		18/32	0.01231(10)	0.95
		19/32	0.01230(10)	0.93
		20/32	0.01229(11)	0.89

Table 3.7: Examples of ratio fits to the $^3S_1 \; - {}^1S_0$ splitting.

very accurate indeed and in figure (3.3) the fitted dimensionless splitting is plotted against t_{min} as described in section 3.2. The determination of the hyperfine splitting was taken at the t_{min} value of 19, where the dimensionless splitting begins to plateau.

For evaluation of P state splittings, advantage was taken of the maximum correlation between particular polarizations of the $^1P_1$ state with those of the $^3P_1$ and $^3P_2$ states. For example, the $^3P_1 y$ polarization state is formed using the smearing spin matrix, $\Omega = \Delta_z\sigma_x - \Delta_x\sigma_z$ (see table (2.2)). Since the initial source spinors only have an upper spin component and since the action of σ_z preserves this, the $^3P_1 y$ state will be maximally correlated with the particular polarization

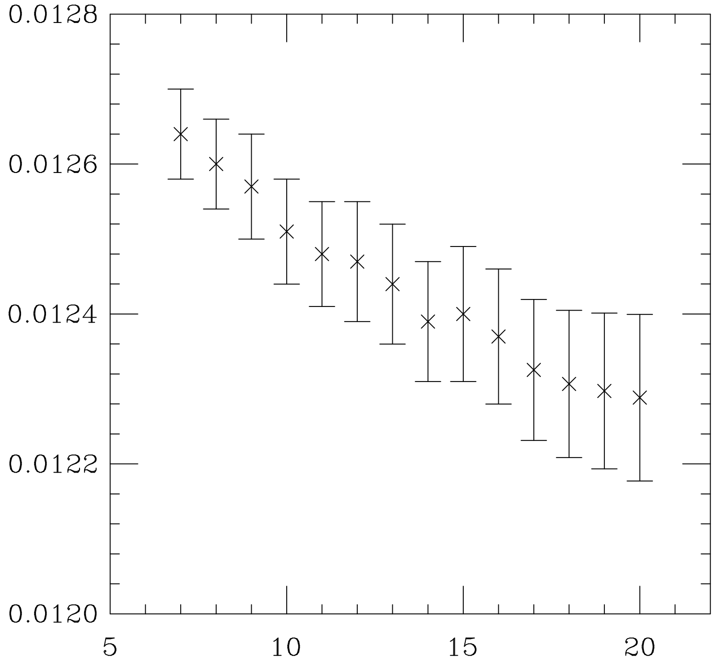

Figure 3.3: $^3S_1 \; - {}^1S_0$ splitting against t_{min} (t_{max} =32).

of the $^1P_1$ state having $\Omega = \Delta_x$ as its smearing spin matrix, namely the ^1P_1x state. Using similar arguments, the ^3P_2Tzx state is maximally correlated with the ^1P_1x state; the ^3P_1x and ^3P_2Tyz states with the ^1P_1y state and the $^3P_0$ and ^3P_2E states with the ^1P_1z state.

As a preliminary assessment of the quality of the data, however, use was made of effective mass plots of $^3P_2$ and $^3P_1$ polarization states, some of which are shown in figure (3.4). Noise can be seen in some of the states in figure (3.4) beginning at times of $15 \sim 20$ and for this reason, a t_{max} value of 15 was chosen for ratio fits to P state splittings.

Shown in tables (3.8), (3.9), (3.10), (3.11) are example results from ratio fits to splittings, which are given in the relevant captions. The results are quite accurate and from figure (3.5), where the dimensionless splittings have been plotted against t_{min}, reasonable plateaux can be observed. Estimations for the splittings were taken at the t_{min} values for which the splittings began to plateau and for which

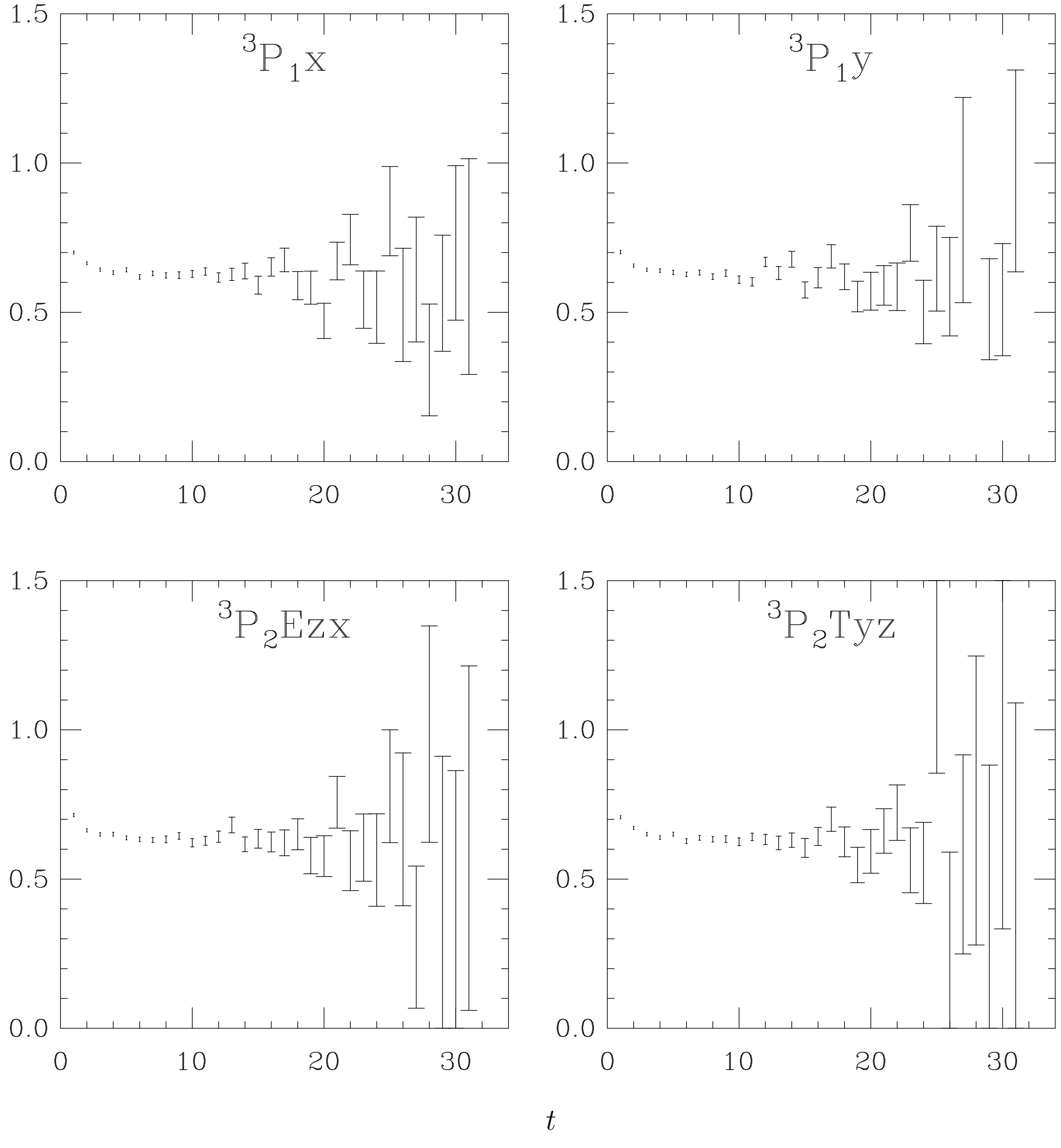

Figure 3.4: Effective masses of some $^3P_1$ and $^3P_2$ polarization states, all of which have the $(1,1)$ smearing combination.

	N_{exp}	t_{min}/t_{max}	$a\delta E$	Q
fits to ratio	1	2/15	0.0027(2)	0.83
of (1,1)		3/15	0.0027(3)	0.77
correlations		4/15	0.0026(4)	0.71
		5/15	0.0026(5)	0.62
		6/15	0.0026(7)	0.52
		7/15	0.0021(9)	0.48
		8/15	0.0022(11)	0.37
		9/15	0.0009(14)	0.55
		10/15	0.0013(18)	0.43
		11/15	0.0014(24)	0.28

Table 3.8: Examples of ratio fits to the ${}^1P_1x - {}^3P_1y$ splitting.

	N_{exp}	t_{min}/t_{max}	$a\delta E$	Q
fits to ratio	1	2/15	0.0044(2)	0.74
of (1,1)		3/15	0.0048(3)	0.87
correlations		4/15	0.0048(4)	0.81
		5/15	0.0052(5)	0.86
		6/15	0.0048(7)	0.86
		7/15	0.0048(9)	0.79
		8/15	0.0046(11)	0.70
		9/15	0.0037(14)	0.72
		10/15	0.0035(18)	0.59
		11/15	0.0038(24)	0.42
		12/15	0.0019(34)	0.33

Table 3.9: Examples of ratio fits to the ${}^3P_2Tyz - {}^1P_1y$ splitting.

	N_{exp}	t_{min}/t_{max}	$a\delta E$	Q
fits to ratio	1	4/15	0.0075(4)	9×10^{-3}
of (1,loc)		5/15	0.0065(5)	0.11
correlations		6/15	0.0063(6)	7×10^{-2}
		7/15	0.0050(8)	0.47
		8/15	0.0048(10)	0.38
		9/15	0.0052(12)	0.30
		10/15	0.0050(16)	0.20
		11/15	0.0058(21)	0.12
		12/15	0.0071(28)	7×10^{-2}

Table 3.10: Examples of ratio fits to the $^3P_2Ezx - {}^1P_1z$ splitting.

	N_{exp}	t_{min}/t_{max}	$a\delta E$	Q
fits to ratio	1	4/15	0.0139(5)	1×10^{-6}
of (1,loc)		5/15	0.0117(6)	0.10
correlations		6/15	0.0111(8)	0.10
		7/15	0.0097(10)	0.45
		8/15	0.0092(12)	0.38
		9/15	0.0099(15)	0.32
		10/15	0.0086(18)	0.35
		11/15	0.0094(24)	0.24
		12/15	0.0111(31)	0.18

Table 3.11: Examples of ratio fits to the $^1P_1z - {}^3P_0$ splitting.

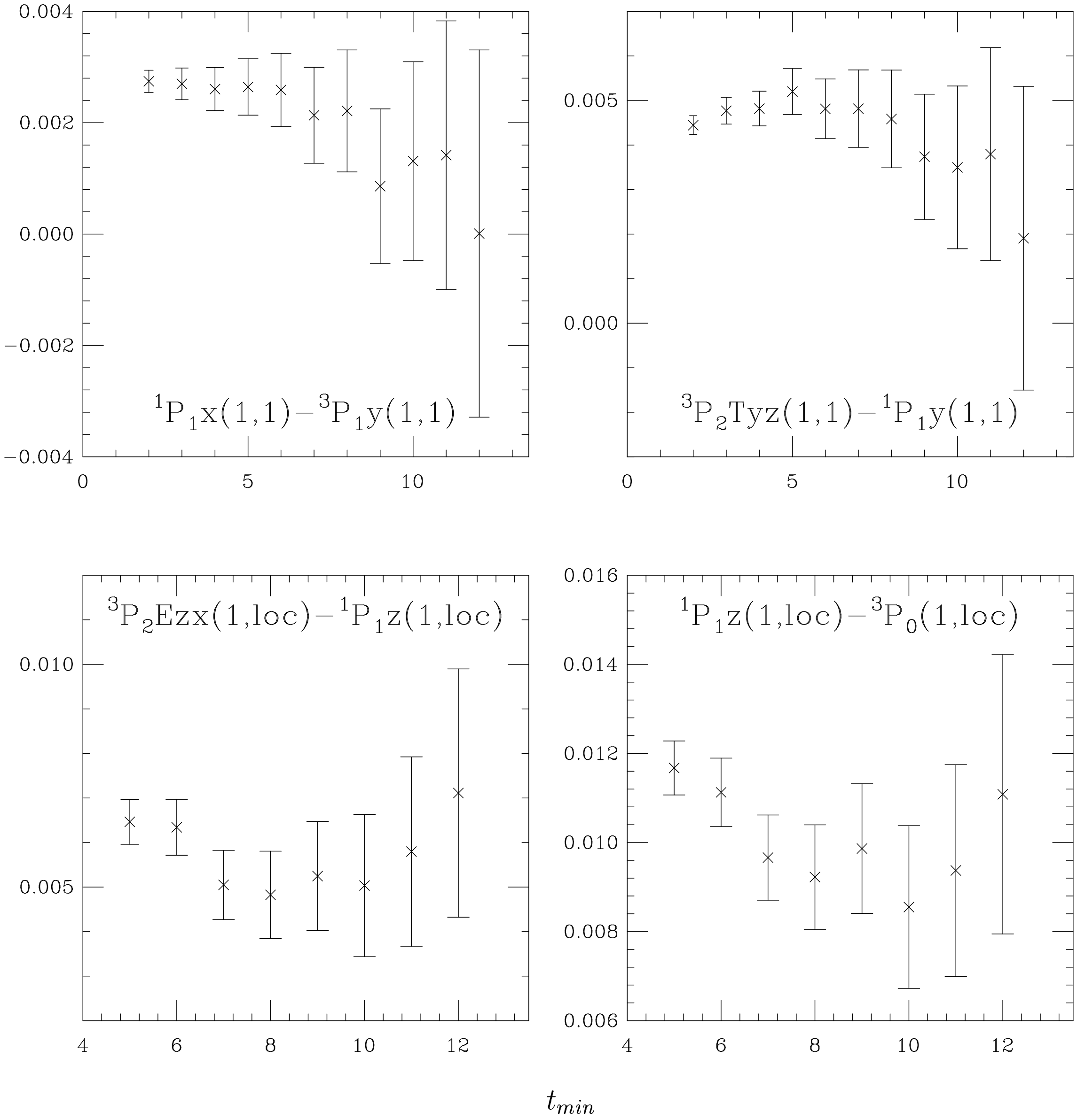

Figure 3.5: Examples of P state splittings against t_{min} ($t_{max} = 15$).

the Q factors rose sharply.

It should be noticed from tables (3.8), (3.9), (3.10), (3.11) that some of the meson correlations used were smeared-smeared, i.e. had $(n_{sc}, n_{sk}) = (1, 1)$ and some were smeared-local, having $(n_{sc}, n_{sk}) = (1, loc)$. Both smeared-smeared and smeared-local meson correlations were used in obtaining splittings thus providing a determination of the systematic error involved in using correlations of a particular smearing type. Results for all the ratio fits are given in table (3.12) along with average splittings between particular channels. The statistical error on this average was taken as the typical statistical error of the individual splittings, while a systematic error was also included to account for the range of the individual splittings.

With the spin-average of the ${}^3P$ states defined as

$$ {}^3P_{\mathrm{CM}} = \frac{5 \times {}^3P_2 \ + 3 \times {}^3P_1 \ + 1 \times {}^3P_0}{9} \tag{3.5} $$

combinations of the averaged ${}^3P_2 - {}^1P_1$, ${}^1P_1 - {}^3P_1$ and ${}^1P_1 - {}^3P_0$ splittings of table (3.12) were used to obtain splittings within the ${}^3P$ states. For instance

$$ {}^3P_{\mathrm{CM}} - {}^3P_0 = \frac{5}{9}({}^3P_2 - {}^1P_1) - \frac{3}{9}({}^1P_1 - {}^3P_1) + \frac{8}{9}({}^1P_1 - {}^3P_0) \tag{3.6} $$

was used to calculate the ${}^3P_{\mathrm{CM}} - {}^3P_0$ splitting. The results for this and similar calculated splittings are shown in table (3.13), where the final errors were obtained by taking all contributing errors in quadrature. These results will be compared with experiment in section 3.5.

3.4 Wavefunctions at the Origin

A quantity of interest which may be used to calculate values for the lattice spacing and which provides a check on the S state hyperfine splitting is the mesonic wavefunction at the origin (i.e. zero separation between the quark and antiquark). From equation (2.97), $\sum_{\mathbf{x}} \psi^\dagger(\mathbf{x})\chi^\dagger(\mathbf{x})$ acting on the vacuum creates a local meson

splitting	simulation result	average result
${}^3P_2Tzx(1,loc) - {}^1P_1x(1,loc)$	0.0065(8)	0.0050(7)(12)
${}^3P_2Tzx(1,1) - {}^1P_1x(1,1)$	0.0045(7)	
${}^3P_2Tyz(1,loc) - {}^1P_1y(1,loc)$	0.0060(7)	
${}^3P_2Tyz(1,1) - {}^1P_1y(1,1)$	0.0048(7)	
${}^3P_2Ezx(1,loc) - {}^1P_1z(1,loc)$	0.0050(8)	
${}^3P_2Ezx(1,1) - {}^1P_1z(1,1)$	0.0046(7)	
${}^3P_2Eyz(1,loc) - {}^1P_1z(1,loc)$	0.0048(8)	
${}^3P_2Eyz(1,1) - {}^1P_1z(1,1)$	0.0039(5)	
${}^1P_1x(1,loc) - {}^3P_1y(1,loc)$	0.0032(4)	0.0028(4)(4)
${}^1P_1x(1,1) - {}^3P_1y(1,1)$	0.0026(5)	
${}^1P_1y(1,loc) - {}^3P_1x(1,loc)$	0.0031(3)	
${}^1P_1y(1,1) - {}^3P_1x(1,1)$	0.0024(4)	
${}^1P_1z(1,loc) - {}^3P_0(1,loc)$	0.0097(10)	0.0097(10)

Table 3.12: Individual dimensionless splittings with quantum numbers, polarizations and smearing combinations specified. For the results in the third column the first error is statistical while the second error is systematic, accounting for the range of individual splittings.

splitting	calculated result
${}^3P_2 - {}^3P_{\rm CM}$	0.0042(7)
${}^3P_{\rm CM} - {}^3P_1$	0.0036(9)
${}^3P_{\rm CM} - {}^3P_0$	0.0105(12)
${}^3P_{\rm CM} - {}^1P_1$	0.0008(8)

Table 3.13: Dimensionless splittings to the ${}^3P_{\rm CM}$.

(zero quark/antiquark separation) with zero momentum in the $^1S_0$ state, $|loc\rangle$. If $|m\rangle$ is the quantum state of an η_b with radial excitation m, then the overlap of $|m\rangle$ and the $|loc\rangle$ state selects the wavefunction at the origin for the $^1S_0$ meson with radial excitation m;

$$\begin{aligned}\Psi_m(0) &= \left\langle m \left| \sum_{\mathbf{x}} \psi^\dagger(\mathbf{x})\chi^\dagger(\mathbf{x}) \right| 0 \right\rangle \\ &= \langle m|loc\rangle \end{aligned} \tag{3.7}$$

If $O_H^\dagger$ is an operator creating a $^1S_0$ meson at position $\mathbf{x}$ and time t in the Heisenberg picture, then the correlation $\sum_{\mathbf{x}} {}_H\langle 0, t=t|O_H(\mathbf{x},t)O_H^\dagger(\mathbf{0},0)|0,t=0\rangle_H$ represents a $^1S_0$ meson propagating between the times $t=0$ and $t=t$. Following the argument of equations (2.117) to (2.124), this meson correlation is transformed into the Schrödinger picture as

$$\sum_m \langle loc|m\rangle\langle m|loc\rangle e^{-E_m t} \tag{3.8}$$

Comparing this with equation (2.126), after putting $(n_{sc}, n_{sk}) = (loc, loc)$ and in the limit of an infinite number of exponentials, $\langle m|loc\rangle$ is equal to $a(loc, m)$ and hence from equation (3.7), so is $\Psi_m(0)$. Then using equation (2.129),

$$a^{3/2}\Psi_m(0) = a^{3/2}\frac{b(n_{sc}, m)}{a(n_{sc}, m)} = \frac{a^3 b(n_{sc}, m)}{a^{3/2}a(n_{sc}, m)} \tag{3.9}$$

where both sides of the equation have been made dimensionless.

Amplitudes from row fits, $a^3 b(n_{sc}, m)$, and from matrix fits, $a^{3/2}a(n_{sc}, m)$, were obtained for both the ground and excited $^3S_1$ and $^1S_0$ states. The results for both states are shown in table (3.14). It is noticeable that the diagonal entries, $m = n_{sc}$, are much larger than the off-diagonal entries. This is evidence that the smearing process is giving the meson correlations a strong overlap with the appropriate radially excited state.

For historical reasons the fitting code fits to $e^{-M(t-1)}$ instead of e^{-Mt} and so the ratio $a^{3/2}b(n_{sc}, m)/a(n_{sc}, m)$ must be multiplied by $e^{aM/2}$, where aM is

	$a^3b(n_{sc},m)$			$a^{3/2}a(n_{sc},m)$	
m^3S_1	$n_{sc}=loc$	$n_{sc}=1$	$n_{sc}=2$	$n_{sc}=1$	$n_{sc}=2$
$m=1$	0.02344(19)	0.0853(4)	−0.0061(2)	0.7011(13)	−0.0540(8)
$m=2$	0.0194(20)	0.0192(9)	0.0569(4)	0.132(4)	0.526(6)
	$a^3b(n_{sc},m)$			$a^{3/2}a(n_{sc},m)$	
m^1S_0	$n_{sc}=loc$	$n_{sc}=1$	$n_{sc}=2$	$n_{sc}=1$	$n_{sc}=2$
$m=1$	0.02625(15)	0.0912(5)	−0.0039(2)	0.7033(12)	−0.0326(7)
$m=2$	0.0187(16)	0.0141(15)	0.0556(9)	0.103(3)	0.530(6)

Table 3.14: Examples of dimensionless amplitudes obtained from multi-exponential fits to $^1S_0$ and $^3S_1$ correlations.

the appropriate state dimensionless mass, to obtain $a^{3/2}\Psi_m(0)$. For instance, for $^3S_1$ with $m = 1$ and $n_{sc} = 1$, $a^{3/2}\Psi_m(0)$ is calculated using values from tables (3.14) and (3.6) as

$$\frac{0.0853(4)}{0.7011(13)} \cdot e^{0.4539(3)/2} = 0.1527(7)$$

Multiplication by the factor $e^{aM/2}$ is not required for values of $a^3b(loc,m)$, however, as an updated fitting code fitting to e^{-Mt} was used to extract these values. The results for all the dimensionless wavefunctions at the origin are collected in table (3.15). They will be investigated in section 5.5 and chapter 6.

3.5 Comparison with Experiment

In section 3.1, the bare quark mass M_b^0 was tuned to match experiment. With the bare coupling g specified in order to generate the gauge configurations, the inverse lattice spacing $a^{-1}(g)$ was determined by matching both the $2S-1S$ and $1P-1S$ dimensionless splittings to experiment (see example calculation (4.2) and

meson(mS)	obtained from $a^{3/2}\sqrt{b(loc,m)}$	$a^{3/2}b(1,m)/a(1,m)$	$a^{3/2}b(2,m)/a(2,m)$
$\Upsilon(1S)$	0.1531(6)	0.1527(7)	0.142(5)
$\Upsilon(2S)$	0.139(7)	0.206(10)	0.1532(18)
$\eta_b(1S)$	0.1620(5)	0.1617(9)	0.149(8)
$\eta_b(2S)$	0.137(6)	0.187(20)	0.144(2)

Table 3.15: Dimensionless wavefunctions at the origin for ground and excited $^1S_0$ and $^3S_1$ states.

table of a inverses (4.1)). These splittings have the advantage of being insensitive to the bare quark mass.

Other Υ research was carried out by the NRQCD collaboration on $16^3 \times 32$ configurations at $\beta = 5.6$ which had two flavours of staggered dynamical quarks having mass $am_q^0 = 0.01$ [48]. This research gave the opportunity to study the effects of quenching on the Υ spectrum and allowed an investigation into the flavour dependency of quantities such as the Peskin ratio and S state hyperfine splitting. The results for various quantities from this dynamical analysis are shown in table (3.16) alongside similar final results for the $\beta = 6.0$ quenched analysis of this chapter.

An average inverse lattice spacing of $a^{-1} = 2.4\,\mathrm{GeV}$ was taken for both $\beta = 5.6$ and 6.0 and used to make the energies and splittings of tables (3.6) and (3.16) dimensionful. The spin-independent energies are shown in figure (3.6), where the simulation energies have been shifted in order to match the 1^3S_1 energies with that of experiment since the rest mass is not included in the NRQCD simulation. Figure (3.7) shows the spin-dependent states. The P state fine structure energies are shown relative to the spin-average of the P states, $^3P_{\mathrm{CM}}$. The errors shown in both figures reflect statistical errors and some systematic fitting errors. Other

quantity	simulation $\beta = 5.6$	result $\beta = 6.0$
1^1S_0		0.4416(3)
2^1S_0		0.684(8)
1^3S_1	0.4937(5)	0.4539(3)
2^3S_1	0.733(10)	0.695(9)
3^3S_1	0.88(3)	0.90(2)
1^1P_1	0.678(5)	0.627(3)
2^1P_1	0.82(3)	0.84(2)
1^3P_{CM}	0.679(5)	0.628(3)
$1^3P_2 - 1^3P_0$	0.019(2)	0.0147(17)
$1^3P_2 - 1^3P_1$	0.0081(10)	0.0078(15)
$1^3P_1 - 1^3P_0$	0.011(2)	0.0069(11)
$1^3P_2 - 1^3P_{\mathrm{CM}}$	0.0048(10)	0.0042(7)
$1^3P_{\mathrm{CM}} - 1^3P_1$	0.0033(10)	0.0036(9)
$1^3P_{\mathrm{CM}} - 1^3P_0$	0.014(2)	0.0105(12)
$1^3P_{\mathrm{CM}} - 1^1P_1$	0.0012(5)	0.0008(8)
$1^3S_1 - 1^1S_0$	0.0154(1)	0.01230(10)
wave func. at		
origin for $\Upsilon(1S)$	0.179(2)	0.1531(6)
for $\Upsilon(2S)$	0.14(2)	0.139(7)

Table 3.16: Dimensionless results from both the dynamical simulation ($n_f = 2$) at $\beta = 5.6$ [48] and the quenched simulation ($n_f = 0$) at $\beta = 6.0$ of this chapter.

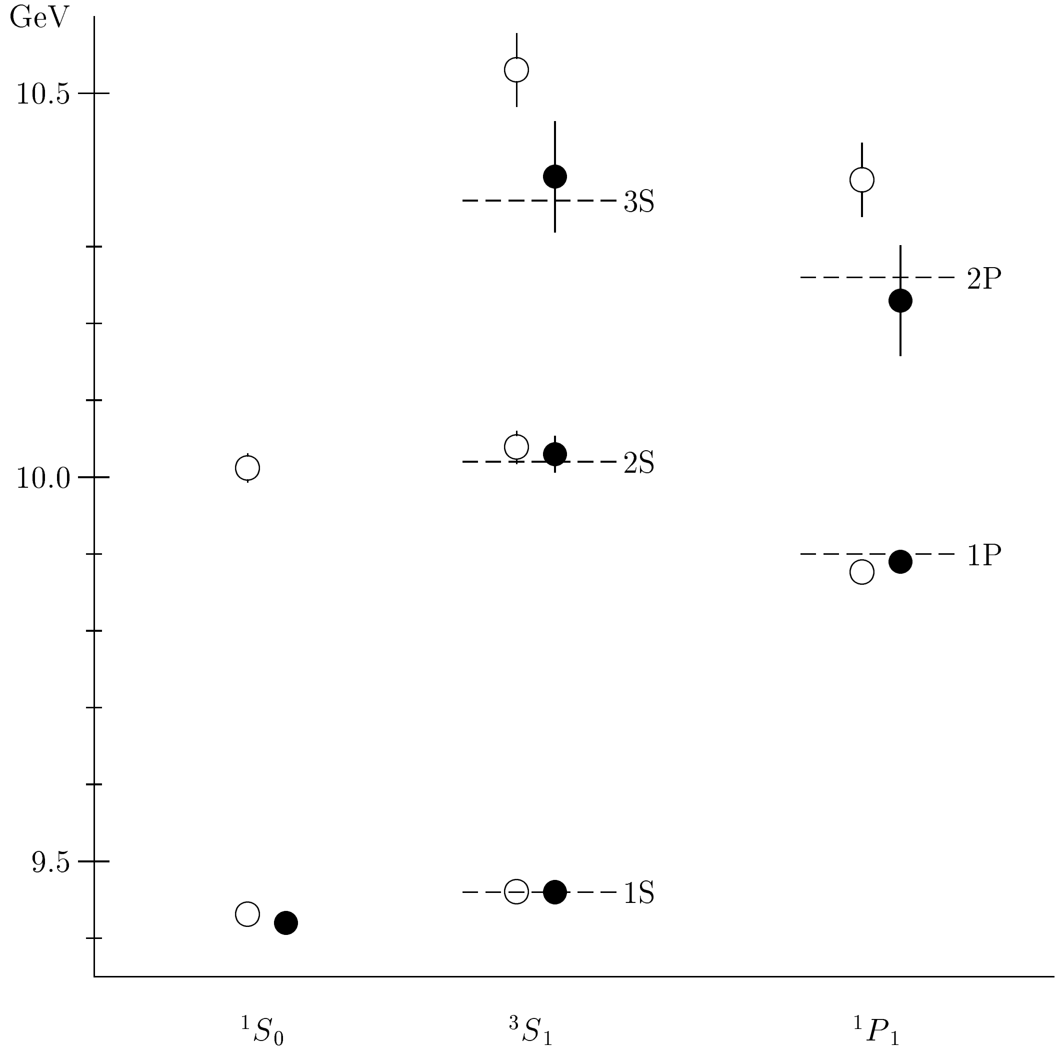

Figure 3.6: Υ **spin-independent spectrum** for $\beta = 6.0$, $n_f = 0$ (open circles) and $\beta = 5.6$, $n_f = 2$ (full circles). The dashed horizontal lines denote experimental values. The energy zero has been shifted such that the 1^3S_1 states coincide with experiment.

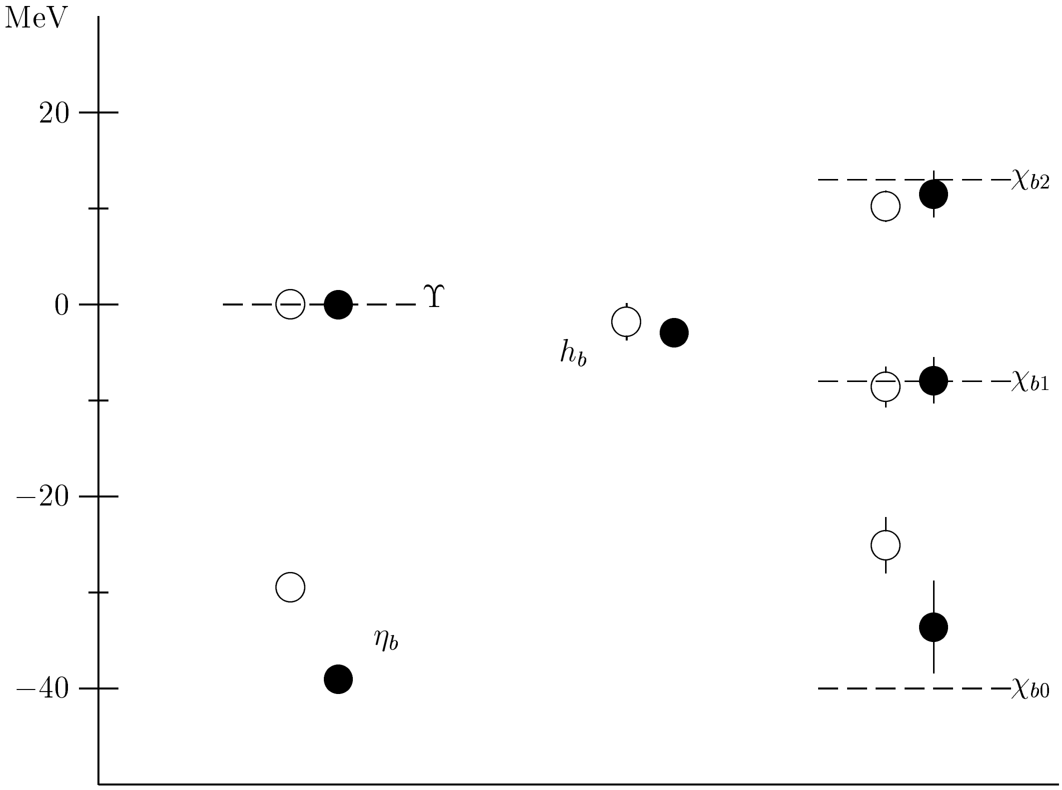

Figure 3.7: Υ **spin-dependent spectrum** for $\beta = 6.0$, $n_f = 0$ (open circles) and $\beta = 5.6$, $n_f = 2$ (full circles). The dashed horizontal lines denote experimental values. Splittings are shown relative to the Υ or ${}^3P_{\rm CM}$ as appropriate.

systematic uncertainties in the value of a^{-1} are not shown.

Good agreement with experiment can be seen in both figures, particularly so for the $\beta = 5.6$ dynamical simulation results. The $\beta = 6.0$ quenched results for the 3^3S_1 and 2^1P_1 states and for the χ_{b0} state show evidence of systematic quenching errors.

In chapter 5, the scaling behaviour of both the spin-dependent spin splittings and the spin-independent radial and orbital splittings with respect to the lattice spacing is established while in chapter 6, the n_f dependencies of these splittings are investigated. Firstly however, in chapter 4, a^{-1} values extracted from the $2S - 1S$ and $1P - 1S$ splittings are used to set the scale for the determination of α_s values.

Chapter 4

Lattice QCD determination of α_s

4.1 Introduction

One of the most important parameters of the Standard Model is the strong coupling constant, α_s. Comparison of accurately determined α_s values from low energy lattice simulations with values obtained from high energy experimental work provides a crucial test of the Standard Model and also gives an insight into any new physics beyond this model.

There are two basic steps in making a determination of the coupling constant from lattice simulations [49, 7]. Section 4.2 deals with the first of these, which is to accurately determine the parameters of the NRQCD Lagrangian, in particular the lattice spacing a, so that it correctly describes continuum QCD. Section 4.3 deals with the second which is to use this Lagrangian to compute nonperturbatively an appropriate short distance quantity. Comparison with the perturbative expansion for this quantity then gives a value for the coupling. Finally in section 4.4, the coupling is converted to the $\overline{\mathrm{MS}}$ scheme to facilitate comparison with other determinations. Various sources of systematic error are also investigated in this section.

4.2 Determination of the Lattice Spacing a

As was mentioned in section 3.5, the inverse lattice spacing was obtained by matching both the $\Upsilon' - \Upsilon$ ($2^3S_1 - 1^3S_1$) and $\chi_b - \Upsilon$ ($1^3P_{\rm CM} - 1^3S_1$) dimensionless splittings to experiment, χ_b representing the spin-average of the 1^3P states, $1^3P_{\rm CM}$. This was done for both the $\beta = 6.0$ quenched ($n_f = 0$) and $\beta = 5.6$ dynamical ($n_f = 2$) simulation results of section 3.5. Before this was done however, the dimensionless splittings were shifted by making $\mathcal{O}(a^2)$ corrections, to account for finite lattice spacing errors in the gluonic action. Being sensitive to short distances, the gluonic mass shift $a\Delta M_g$ can be estimated using the perturbative expansion [49]

$$a\Delta M_g = \frac{4\pi\alpha_P(q_\delta)}{15} a^3 |\Psi_m(0)|^2 \tag{4.1}$$

with $q_\delta \sim 5\,$GeV being the typical momentum transferred through the interaction. (α_P is the coupling constant in the plaquette scheme, defined in the next section).

As an example, using the most accurate values of $a^{3/2}\Psi_m(0)$ from table (3.15) and putting $\alpha_P(q_\delta) = 0.19$ (obtained from a previous simulation [49]), $a\Delta M_g$ was found to be 0.0037 for the quenched Υ state and 0.0031 for the quenched Υ' state, while for the quenched χ_b state, $a\Delta M_g = 0$ since the wavefunction falls to zero at the origin for P states.

With the experimental value for the $\chi_b - \Upsilon$ splitting [3] given as $\Delta M =$ 439.8MeV, the inverse lattice spacing was found from the quenched $\chi_b - \Upsilon$ splitting as follows

$$a\Delta M(\chi_b - \Upsilon) = 0.628(3) - 0.4539(3) - 0.0036 = 0.170(3)$$

$$\text{hence} \qquad a^{-1} = \frac{439.8\,\text{MeV}}{0.170(3)} = 2.59(5)\ \text{GeV}. \tag{4.2}$$

Similar calculations for the other splittings produced the results shown in table (4.1).

β	n_f	splitting	$a\Delta M$	$a\Delta M_g$	a^{-1}(GeV)
6.0	0	$\Upsilon' - \Upsilon$	0.242(5)	-0.001	2.34(9)
		$\chi_b - \Upsilon$	0.174(3)	-0.004	2.59(5)
5.6	2	$\Upsilon' - \Upsilon$	0.239(10)	-0.002	2.37(10)
		$\chi_b - \Upsilon$	0.185(5)	-0.005	2.44(7)

Table 4.1: Results for mass spittings $a\Delta M$, gluonic corrections $a\Delta M_g$ and inverse lattice spacings a^{-1} (in GeV) for both quenched and dynamical simulations. (Experimental values for ΔM are 562.9 MeV for $\Upsilon' - \Upsilon$ and 439.8 MeV for $\chi_b - \Upsilon$).

It will be noticed from table (4.1) that estimates of a^{-1} from different splittings can be very different, particularly for $n_f = 0$. For instance values from $\Upsilon' - \Upsilon$ and $\chi_b - \Upsilon$ splittings for $n_f = 0$ differ by five standard deviations. Such discrepancies are expected in simulations with the wrong number n_f of light quark flavours in the vacuum polarization. Since the typical momentum exchanged between the b quarks in an Υ is 0.5–1 GeV, ruling out vacuum polarization of the c, b and t quarks, inverse lattice spacings should only agree when $n_f = 3$. This will be shown to be true in the next section, indirectly, through the plaquette coupling α_P.

4.3 The Plaquette Coupling α_P

The short distance quantity mentioned in section 4.1 was chosen to be the 1×1 Wilson loop operator, $W_{1,1}$, which is the expectation value of one third the trace of the plaquette, $\langle \frac{1}{3} \mathrm{Tr} U_P \rangle$ (for definition of the plaquette, see chapter 1, section 1.7.3). This is the smallest and therefore most perturbative gauge-invariant quantity in lattice QCD and also among the simplest to compute nonperturbatively in Monte Carlo simulations since it requires only the gauge part of the Lagrangian.

β	n_f	$-\ln W_{1,1}$	$\alpha_P^{(n_f)}(3.40/a)$
6.0	0	0.5214	0.1519
5.6	2	0.5709	0.1788

Table 4.2: Expectation values of the 1×1 Wilson loop and the corresponding $\alpha_P^{(n_f)}$ values for both quenched and dynamical simulations.

The coupling α_P is defined in terms of the logarithm of $W_{1,1}$ by [7]

$$-\ln W_{1,1} \equiv \frac{4\pi}{3}\alpha_P^{(n_f)}(3.40/a)\left\{1-(1.190+0.070\,n_f)\alpha_P^{(n_f)}\right\} \tag{4.3}$$

and is chosen to coincide through order $(\alpha_P^{(n_f)})^2$ with the coupling α_V, defined in [39][1]. The scale $3.40/a$ indicates the important momentum scale in $W_{1,1}$ and was obtained using the technique described in [39], whereby the coupling can be extracted from the appropriate loop momentum integral and expanded in terms of an arbitrary scale thereby allowing a determination of the optimal scale involved. The scale $3.40/a$ corresponds to 8–9 GeV for $\beta = 5.6 \sim 6.0$ confirming that $W_{1,1}$ is very ultraviolet.

Simulation results for $-\ln W_{1,1}$ [47, 8] are given in table (4.2) along with the corresponding $\alpha_P^{(n_f)}$ values extracted using equation (4.3). Using the a^{-1} values of table (4.1) obtained from the $\Upsilon' - \Upsilon$ splitting to scale the $\alpha_P^{(n_f)}$ values,

$$\alpha_P^{(0)}(7.96(31)\text{ GeV}) = 0.1519$$

$$\alpha_P^{(2)}(8.06(34)\text{ GeV}) = 0.1788$$

[1]It is interesting to note the relationship between α_P (or α_V) and β. It is

$$\alpha_P(q) = \frac{3}{2\pi\beta}\left\{1+\frac{6}{\beta}\left(2b_0\ln\left(\frac{\pi/a}{q}\right)+d_{V,L}\right)\right\}+\mathcal{O}\left(\frac{1}{\beta^3}\right). \tag{4.4}$$

The three-loop beta function appropriate to the plaquette scheme[2] was used to evolve the couplings to a common scale of 8.2 GeV, giving

$$\alpha_P^{(n_f)}(8.2\,\mathrm{GeV}) = \begin{cases} 0.1506(17) & \text{for } n_f = 0 \\ 0.1778(23) & \text{for } n_f = 2 \end{cases}$$

It should be noticed that the original statistical a^{-1} errors in the scale determination are now manifested in the values of the couplings themselves. For extrapolation to $n_f = 3$, perturbation theory suggests that $1/\alpha_P^{(n_f)}$ is more nearly linear for small changes in n_f than $\alpha_P^{(n_f)}$ itself, hence extrapolation of the inverse coupling gave

$$\alpha_P^{(3)}(8.2\,\mathrm{GeV}) = 0.1955(44) \qquad \text{for} \quad \Upsilon' - \Upsilon \text{ splitting}$$

The above analysis was repeated using a^{-1} values from $\chi_b - \Upsilon$ splittings giving

$$\alpha_P^{(n_f)}(8.2\,\mathrm{GeV}) = \begin{cases} 0.1552(9) & \text{for } n_f = 0 \\ 0.1795(16) & \text{for } n_f = 2 \end{cases}$$

and so

$$\alpha_P^{(3)}(8.2\,\mathrm{GeV}) = 0.1947(30) \qquad \text{for} \quad \chi_b - \Upsilon \text{ splitting}$$

The concordance of this result with that for the $\Upsilon' - \Upsilon$ splitting is more readily appreciated in figure (4.1), where the five standard deviations difference in the inverse couplings at $n_f = 0$ (resulting from the five standard deviations difference in the two estimates of a^{-1} at $n_f = 0$) and the one standard deviation difference in the inverse couplings at $n_f = 2$ (resulting from the one standard deviation difference in the two estimates of a^{-1} at $n_f = 2$) disappear on extrapolation to $n_f = 3$.

[2]This was obtained by adding to the universal two-loop beta function [50] a three-loop coefficient (with incomplete n_f dependence) as calculated by [51].

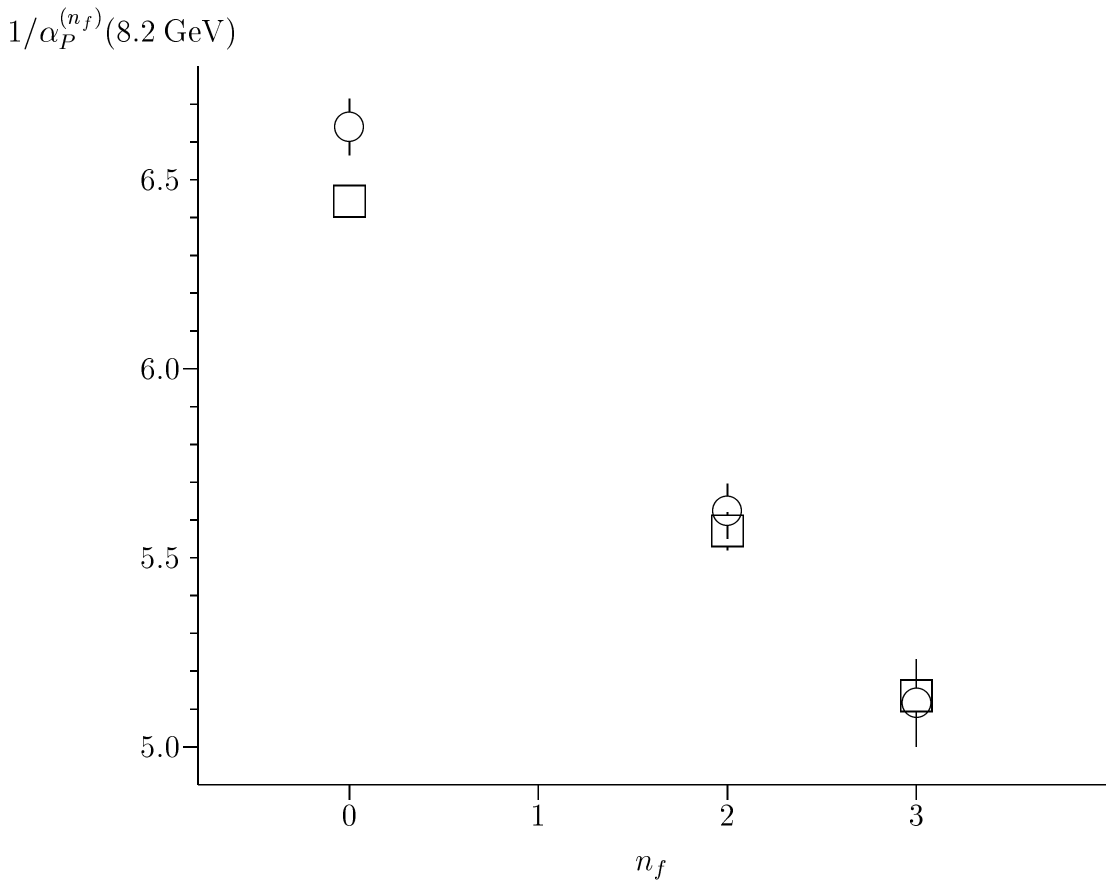

Figure 4.1: Inverse plaquette couplings at 8.2 GeV against number of flavours of vacuum polarization quarks. Couplings are scaled by $\Upsilon' - \Upsilon$ splitting (circles) and $\chi_b - \Upsilon$ splitting (boxes).

4.4 Investigation of α_P Results

To facilitate comparison with other α_s determinations, conversion to the $\overline{\mathrm{MS}}$ scheme was undergone using the formula (obtained by combining expressions from [52, 53, 54])

$$\alpha_{\overline{\mathrm{MS}}}^{(n_f)}(Q) = \alpha_P^{(n_f)}(e^{5/6}Q)\left\{1 + \frac{2}{\pi}\alpha_P^{(n_f)} + 0.95(\alpha_P^{(n_f)})^2 + \mathcal{O}\left((\alpha_P^{(n_f)})^3\right)\right\} \tag{4.5}$$

with $n_f = 3$. Here the $e^{5/6}$ factor in the scale is chosen to remove the n_f dependence of the $(\alpha_P^{(n_f)})^2$ coefficient. The n_f dependence of the $(\alpha_P^{(n_f)})^3$ coefficient, however, is not known and only the $n_f = 0$ part is given in equation (4.5). The error for $\alpha_{\overline{\mathrm{MS}}}^{(3)}(e^{-5/6} \times 8.2\,\mathrm{GeV})$ was obtained by taking the error on $\alpha_P^{(3)}(8.2\,\mathrm{GeV})$ in quadrature with the leading truncated term $(\alpha_P^{(n_f)})^4$, assuming a coefficient of one for this term. The absence of n_f dependence in the $(\alpha_P^{(n_f)})^3$ coefficient was not incorporated into this error.

Subsequent $\alpha_{\overline{\mathrm{MS}}}^{(5)}$ values were obtained at the Z^0 mass, M_Z, by running the coupling $\alpha_{\overline{\mathrm{MS}}}^{(3)}$ using the $\overline{\mathrm{MS}}$ three-loop beta function down to the c quark threshold, applying appropriate matching conditions[3] to obtain $\alpha_{\overline{\mathrm{MS}}}^{(4)}$ at this threshold, running up to the b quark threshold, applying appropriate matching conditions [50] to obtain $\alpha_{\overline{\mathrm{MS}}}^{(5)}$ at this threshold and finally running up to M_Z. (The $\overline{\mathrm{MS}}$ c quark mass at a scale equal to this mass was taken to be 1.3 GeV [50] while the $\overline{\mathrm{MS}}$ b quark mass at a scale equal to this mass was taken from section 4.4.3 to be 4.1 GeV). Values for $\alpha_{\overline{\mathrm{MS}}}$ at both the c and b thresholds and at M_Z for both the $\Upsilon' - \Upsilon$ and $\chi_b - \Upsilon$ splittings are shown in table (4.3). The results in the last column are extremely accurate and encouraging since they agree with the world average of $\alpha_{\overline{\mathrm{MS}}}^{(5)}(M_Z) = 0.118(3)$, obtained from a variety of determinations shown in figure (4.2).

[3]These matching conditions, described in [50], allow the coupling in a theory with n_f quark flavours to be expanded in terms of the coupling in a theory with $n_f - 1$ quark flavours.

splitting	$\alpha^{(3)}_{\overline{\rm MS}}(e^{-5/6}\times 8.2\,{\rm GeV})$	$\alpha^{(3,4)}_{\overline{\rm MS}}(M_c)$	$\alpha^{(4,5)}_{\overline{\rm MS}}(M_b)$	$\alpha^{(5)}_{\overline{\rm MS}}(M_Z)$
$\Upsilon' - \Upsilon$	0.2269(62)	0.371(18)	0.2234(62)	0.1174(17)
$\chi_b - \Upsilon$	0.2258(43)	0.369(13)	0.2224(43)	0.1171(11)

Table 4.3: Values of $\alpha_{\overline{\rm MS}}$ at various scales with appropriate number of light quarks incorporated. M_c and M_b are the c and b $\overline{\rm MS}$ quark masses (evaluated at scales equal to the masses), taken to be 1.3 GeV and 4.1 GeV respectively. $M_Z = 91.2\,{\rm GeV}$ is the mass of the Z boson.

A more pessimistic and perhaps realistic error estimate can be made by allowing the n_f dependent piece of the $(\alpha_P^{(n_f)})^3$ coefficient to have a value in the range -1 to 1 and combining this in quadrature with the error on $\alpha_P^{(3)}(8.2\,{\rm GeV})$ to produce an error for $\alpha^{(3)}_{\overline{\rm MS}}(e^{-5/6}\times 8.2\,{\rm GeV})$. A similar analysis to the above subsequently gave

$$\alpha^{(5)}_{\overline{\rm MS}}(M_Z) = \begin{cases} 0.1174(27) & \text{for } \Upsilon' - \Upsilon \text{ splitting} \\ 0.1171(23) & \text{for } \chi_b - \Upsilon \text{ splitting} \end{cases}$$

These final results are 1σ higher than the previous NRQCD quoted results from [49] due entirely to the inclusion of the two-loop coefficient in the conversion to the $\overline{\rm MS}$ scheme (4.5).

Various sources of systematic error contributing to the results in table (4.3) were investigated and are discussed in the following subsections.

4.4.1 Conversion to $\overline{\rm MS}$ scheme using the same scale

The α_P results of section 4.3 were converted to $\alpha_{\overline{\rm MS}}$ values this time using the formula (obtained by combining expressions from [52, 53, 54])

$$\alpha^{(n_f)}_{\overline{\rm MS}}(Q) = \alpha_P^{(n_f)}(Q)\left\{1 + \left(\frac{5\,n_f}{18\pi} - \frac{31}{12\pi}\right)\alpha_P^{(n_f)} + 0.17(\alpha_P^{(n_f)})^2 + \mathcal{O}\left((\alpha_P^{(n_f)})^3\right)\right\}$$

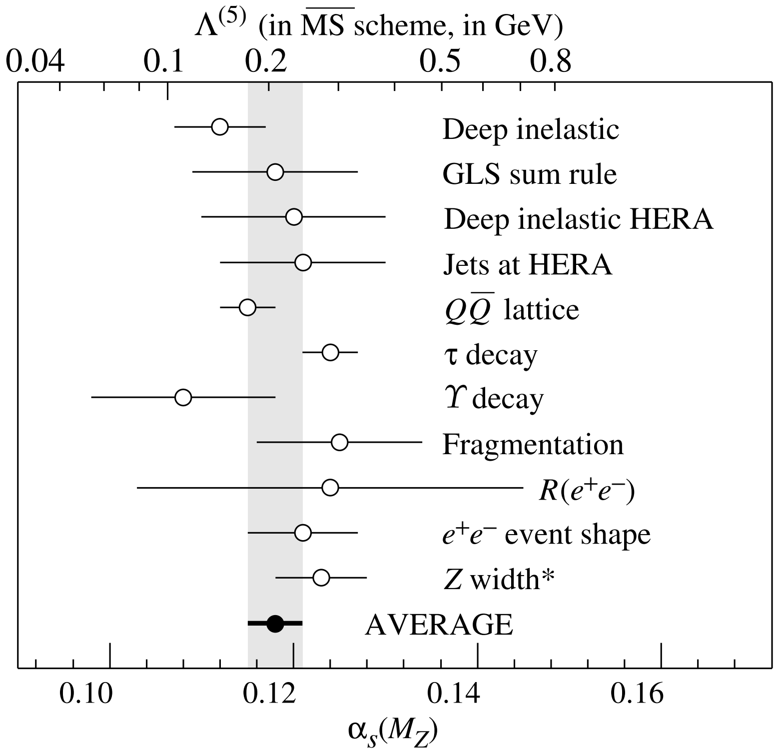

Figure 4.2: $\alpha_{\overline{\mathrm{MS}}}(M_Z)$ values obtained from a variety of determinations along with their average, 0.118(3) [3]. The $Q\overline{Q}$ lattice result shown here is 0.115(3) obtained from a previous NRQCD determination [49].

with $n_f = 3$. This is similar to equation (4.5) but has equal scales for α_P and $\alpha_{\overline{\rm MS}}$. As a consequence, the omission of the $e^{5/6}$ factor gives an n_f dependent coefficient for the $(\alpha_P^{(n_f)})^2$ term. Similar to equation (4.5), the n_f dependence of the $(\alpha_P^{(n_f)})^3$ coefficient is not known and only the $n_f = 0$ part is given.

A similar running and matching analysis to that of section 4.4 gave the results

$$\alpha_{\overline{\rm MS}}^{(5)}(M_Z) = \begin{cases} 0.1179(18) & \text{for } \Upsilon' - \Upsilon \text{ splitting} \\ 0.1176(13) & \text{for } \chi_b - \Upsilon \text{ splitting} \end{cases}$$

Even with error estimates that neglect the n_f dependence of the $(\alpha_P^{(n_f)})^3$ term, the results only differ by $\frac{1}{3} \sim \frac{1}{2}\sigma$ from those of the last column of table (4.3), confirming that the choice of scale factor in converting to the $\overline{\rm MS}$ scheme essentially does not affect the final $\alpha_{\overline{\rm MS}}^{(5)}(M_Z)$ results.

4.4.2 Effect of changing the c quark mass

The value of the $\overline{\rm MS}$ charm mass is generally determined from heavy quark studies of the J/ψ and D mesons and is believed to lie in the region $1.1 \sim 1.5$ GeV when quoted at a scale equal to the mass. To test the effect of this uncertainty on the final $\alpha_{\overline{\rm MS}}^{(5)}(M_Z)$ values, the analysis of section 4.4 was repeated substituting, in turn, for the charm mass and its corresponding matching threshold, the values 1.1 GeV to 1.5 GeV in steps of 0.05 GeV, the b quark mass and its matching threshold remaining unchanged at 4.1 GeV.

Figure (4.3) shows the consequent $\alpha_{\overline{\rm MS}}^{(5)}(M_Z)$ values and gives a clear indication that the charm mass uncertainty has a negligible influence on the $\alpha_{\overline{\rm MS}}^{(5)}(M_Z)$ results.

4.4.3 Determination of the b quark mass

The value of the $\overline{\rm MS}$ bottom mass can be determined from heavy quark studies of the Υ. One such determination [27] used the formulae

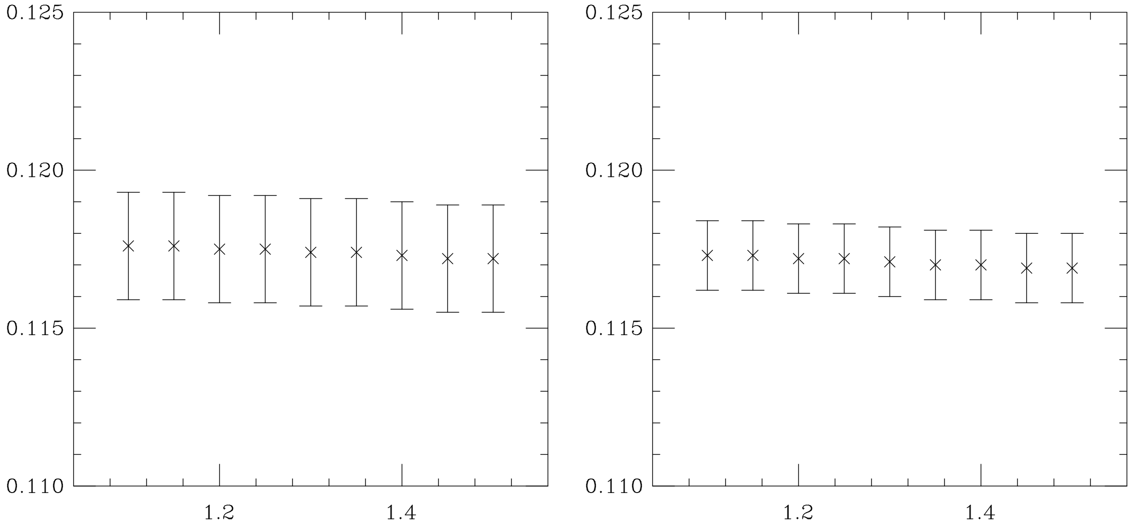

Figure 4.3: Values of $\alpha^{(5)}_{\overline{\rm MS}}(M_Z)$ against charm quark mass (in GeV) obtained from [55]. Initial scaling from $\Upsilon' - \Upsilon$ splitting (left figure) and $\chi_b - \Upsilon$ splitting (right figure).

$$M_b = \frac{1}{2}(M_\Upsilon - (E_\Upsilon(\mathbf{0}) - 2E_0)) \tag{4.6}$$

$$M_b = Z_m M_\Upsilon \frac{aM_b^0}{aM_{kin}} \tag{4.7}$$

to obtain values for the pole mass[4] of the b quark. Here $M_\Upsilon = 9.46$ GeV is the experimental Υ mass, $E_\Upsilon(\mathbf{0})$ is the non-relativistic energy of an Υ with zero momentum, M_{kin} is the kinetic mass as discussed in section 3.1 and E_0 and Z_m are the effective quark binding energy and mass renormalization constant respectively, determined from perturbation theory. The value obtained by [27] for this pole mass was 5.0(2) GeV and for the $\overline{\rm MS}$ mass, at a scale equal to this pole mass, 4.0(1) GeV;

[4]In perturbation theory the running mass $M_b(q)$ stops running when q falls below $M_b(q)$. When this happens $M_b(q)$ is equal to the b quark pole mass, defined in terms of the quark propagator.

$$M_b^{\overline{\rm MS}}(5.0(2)\ \mathrm{GeV}) = 4.0(1)\ \mathrm{GeV} \tag{4.8}$$

However matching at the b quark threshold [50] requires a mass value at a scale equal to itself. To obtain this value, the two-loop renormalization group equation for the running mass

$$\frac{\mathrm{d}m^2}{\mathrm{d}t} = -4\pi\left\{\gamma_0\left(\frac{\alpha_s}{\pi}\right) + \gamma_1\left(\frac{\alpha_s}{\pi}\right)^2\right\}m^2 \tag{4.9}$$

where

$$t = \frac{1}{2\pi}\log\left(\frac{\mu}{\mu_0}\right) \quad , \qquad \gamma_0 = 2 \qquad \text{and} \qquad \gamma_1 = \frac{101}{12} - \frac{5}{18}n_f$$

can be integrated by making use of the three-loop renormalization group equation for the running coupling constant

$$\frac{\mathrm{d}\alpha_s}{\mathrm{d}t} = -\alpha_s^2\left\{\beta_0 + \frac{\beta_1}{4\pi}\alpha_s + \frac{\beta_2}{(4\pi)^2}\alpha_s^2\right\} \tag{4.10}$$

where

$$\beta_0 = 11 - \frac{2}{3}n_f, \qquad \beta_1 = 102 - \frac{38}{3}n_f \qquad \text{and} \qquad \beta_2 = \frac{1}{2}(2857 - \frac{5033}{9}n_f + \frac{325}{27}n_f^2)$$

and t is the same as above. In both equations (4.9) and (4.10), the mass and coupling constant are evaluated at the scale μ (which is suppressed for clarity), μ_0 being an arbitrary reference scale. The coefficients β_0 and β_1 are universal while β_2 is given for the $\overline{\rm MS}$ scheme.

To illustrate the integration, equations (4.9) and (4.10) for the $\overline{\rm MS}$ scheme can be rearranged to give[5]

$$-\frac{\mathrm{d}m^2}{4\pi m^2} = \frac{\gamma_0}{\pi}\alpha_s\,\mathrm{d}t + \frac{\gamma_1}{\pi^2}\alpha_s^2\,\mathrm{d}t \tag{4.11}$$

$$\frac{-\mathrm{d}\alpha_s}{\alpha_s\left(\beta_0 + \frac{\beta_1}{4\pi}\alpha_s + \frac{\beta_2}{(4\pi)^2}\alpha_s^2\right)} = \alpha_s\,\mathrm{d}t \tag{4.12}$$

[5] In the equations that follow, both the scale and the $\overline{\rm MS}$ subscript are omitted for clarity

and so substitution of the second into the first gives

$$\int \frac{\mathrm{d}m^2}{4m^2} = \gamma_0 \int \frac{\mathrm{d}\alpha_s}{\alpha_s \left(\beta_0 + \frac{\beta_1}{4\pi}\alpha_s + \frac{\beta_2}{(4\pi)^2}\alpha_s^2\right)} + \frac{\gamma_1}{\pi} \int \frac{\mathrm{d}\alpha_s}{\left(\beta_0 + \frac{\beta_1}{4\pi}\alpha_s + \frac{\beta_2}{(4\pi)^2}\alpha_s^2\right)} \tag{4.13}$$

The term on the left hand side is readily integrated, while the first term on the right hand side can be made integrable using partial fractions. The integration (4.13) then becomes

$$\begin{aligned} \frac{1}{4}\ln(m^2) &= \frac{\gamma_0}{\beta_0}\ln(\alpha_s) - \frac{\gamma_0}{2\beta_0} \int \frac{\left(\frac{2\beta_2}{(4\pi)^2}\alpha_s + \frac{\beta_1}{4\pi}\right)\mathrm{d}\alpha_s}{\left(\beta_0 + \frac{\beta_1}{4\pi}\alpha_s + \frac{\beta_2}{(4\pi)^2}\alpha_s^2\right)} \\ &\quad + \left(\frac{\gamma_1}{\pi} - \frac{\beta_1\gamma_0}{8\pi\beta_0}\right) \int \frac{\mathrm{d}\alpha_s}{\left(\beta_0 + \frac{\beta_1}{4\pi}\alpha_s + \frac{\beta_2}{(4\pi)^2}\alpha_s^2\right)} \end{aligned} \tag{4.14}$$

and so the full solution is

$$\begin{aligned} \frac{1}{2}\ln(m) &= \frac{\gamma_0}{\beta_0}\ln(\alpha_s) - \frac{\gamma_0}{2\beta_0}\ln\left(\beta_0 + \frac{\beta_1}{4\pi}\alpha_s + \frac{\beta_2}{(4\pi)^2}\alpha_s^2\right) \\ &\quad + \frac{4\pi}{(\beta_0\beta_2 - \beta_1^2)^{1/2}}\left(\frac{\gamma_1}{\pi} - \frac{\beta_1\gamma_0}{8\pi\beta_0}\right)\tan^{-1}\left(\frac{\beta_2\alpha - s + 2\pi\beta_1}{4\pi(\beta_0\beta_2 - \beta_1^2)^{1/2}}\right) \\ &\quad + \text{constant} \end{aligned} \tag{4.15}$$

The constant was evaluated by putting, for m and α_s, the values $M_b^{\overline{\mathrm{MS}}}(5.0(2)\mathrm{GeV}) = 4.0(1)\,\mathrm{GeV}$ (equation (4.8)) and $\alpha^{(4)}_{\overline{\mathrm{MS}}}(5.0\,\mathrm{GeV}) = 0.2023(73)$ (obtained by running results in section 4.4 using the three-loop beta function). An iterative procedure was then used to obtain the scale for which the mass equaled this scale. It was found to be

$$M_b^{\overline{\mathrm{MS}}}(4.1(1)\ \mathrm{GeV}) = 4.1(1)\ \mathrm{GeV}. \tag{4.16}$$

To test the effect of the uncertainty in this value on final $\alpha^{(5)}_{\overline{\mathrm{MS}}}(M_Z)$ values, an analysis similar to that of section 4.4.2 was performed, only this time the b quark mass and its corresponding matching threshold were varied from 3.9 GeV

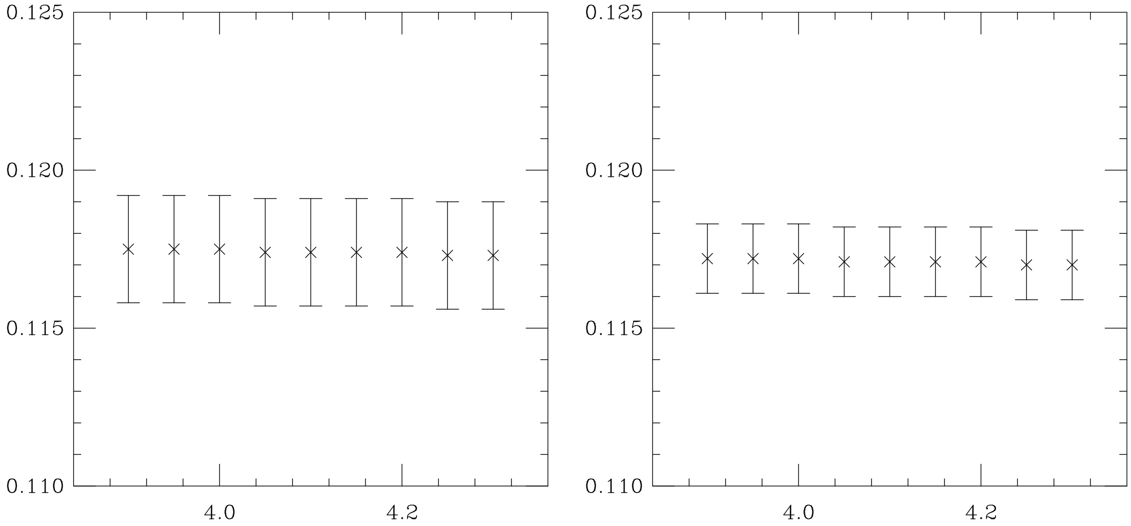

Figure 4.4: Values of $\alpha^{(5)}_{\overline{\rm MS}}(M_Z)$ against bottom quark mass (in GeV) obtained from [55]. Initial scaling from $\Upsilon' - \Upsilon$ splitting (left figure) and $\chi_b - \Upsilon$ splitting (right figure).

to 4.3 GeV in steps of 0.05 GeV, the c quark mass and its matching threshold remaining unchanged at 1.3 GeV. As can be clearly seen from figure (4.4), the bottom mass uncertainty also has a negligible influence on the $\alpha^{(5)}_{\overline{\rm MS}}(M_Z)$ results.

4.4.4 Extrapolation of α_P to $n_f = 4$

The extrapolation of the inverse coupling against n_f in figure (4.1) and the apparent concordance at $n_f = 3$ of the couplings obtained from two different splittings lends weight to the argument of section 4.2; that vacuum polarization of the c, b and t quarks should be ignored when extrapolating quantities scaled by lattice spacings obtained from Υ spin-independent radial and orbital splittings.

To test this argument further, the $\alpha_P^{(n_f)}(8.2\text{ GeV})$ values of section 4.3 for $n_f = 0, 2$, scaled by both the $\Upsilon' - \Upsilon$ and $\chi_b - \Upsilon$ splittings, were extrapolated inversely to $n_f = 4$ giving

$$\alpha_P^{(4)}(8.2\,\mathrm{GeV}) = \begin{cases} 0.2170(77) & \text{for } \Upsilon' - \Upsilon \text{ splitting} \\ 0.2128(50) & \text{for } \chi_b - \Upsilon \text{ splitting} \end{cases}$$

The fact that these two values are only 1σ apart makes it plausible that 4 is the correct number of flavours of vacuum polarization quarks to include when extrapolating quantities scaled by the a^{-1} values of table (4.1). Converting to the $\overline{\mathrm{MS}}$ scheme using (4.5), running up to the b quark threshold using the three-loop beta function, applying appropriate matching conditions to obtain $\alpha_{\overline{\mathrm{MS}}}^{(5)}$ at this threshold and then running up to M_Z yielded the results

$$\alpha_{\overline{\mathrm{MS}}}^{(5)}(M_Z) = \begin{cases} 0.1224(24) & \text{for } \Upsilon' - \Upsilon \text{ splitting} \\ 0.1211(16) & \text{for } \chi_b - \Upsilon \text{ splitting} \end{cases}$$

Comparing to the last column of table (4.3), it is immediately noticed that the errors here are much larger owing to extra extrapolation (18% instead of 9%). However it is also apparent that the central values here are larger by about $2 \sim 2\frac{1}{2}\sigma$, making it therefore important to know which n_f value is the correct one for extrapolation of α_P. Although $n_f = 3$ is believed to be correct, this will only be confirmed when NRQCD simulations are undertaken having four flavours of dynamical quarks. This will allow values of $\alpha_P^{(4)}$ to be obtained directly, without extrapolation, and so from the smaller errors a discrepancy should be seen for values scaled by different Υ splittings.

4.4.5 Extraction of α_P at a lower scale

As mentioned in section 4.3, the scale at which α_P was extracted from $-\ln W_{1,1}$ was determined using a technique from [39]. Often, however, it is enough to guess approximately the important scale involved and so to test this theory α_P values were extracted at the lower scale of $2/a$.

To obtain an appropriate expansion of $-\ln W_{1,1}$ in terms of $\alpha_P(2/a)$, the equation connecting the V scheme with the bare lattice scheme L [53],

$$g_V^2(q) = g_L^2 \left\{ 1 + g_L^2 \left(2b_0 \ln \left(\frac{\pi/a}{q} \right) + d_{V,L} \right) \right\} + \mathcal{O}(g_L^6), \tag{4.17}$$

was rearranged, setting $q = 2/a$, to give

$$\begin{aligned} \alpha_L &= \alpha_V(2/a) \left\{ 1 - \alpha_V(2/a) \left[\left(\frac{31}{12\pi} - \frac{11}{2\pi} \ln 2 + 12\pi P - \frac{\pi}{6} \right) \right. \right. \\ &\quad \left. \left. + \left(\frac{\ln 2}{3\pi} - 4\pi P_4 - \frac{5}{18\pi} \right) n_f \right] \right\} + \mathcal{O}(\alpha_V^3) \end{aligned} \tag{4.18}$$

where $P = 0.169956$ and $P_4 = 0.0026248$. The bare lattice coupling expansion of $-\ln W_{1,1}$ (obtained using [53, 54]) is

$$-\ln W_{1,1} = \frac{4\pi}{3} \alpha_L + (4\pi)^2 \left(\frac{13}{144} - 8x_1 - \frac{8}{3} x_2 n_f \right) \alpha_L^2 + 74.0794\, \alpha_L^3, \tag{4.19}$$

where $x_1 = 1.01404 \times 10^{-4}$ and $x_2 = 6.12401 \times 10^{-4}$, and so substitution of (4.18) into this expression gives

$$\begin{aligned} -\ln W_{1,1} &= \frac{4\pi}{3} \alpha_V(2/a) \left\{ 1 - \alpha_V \left[\left(\frac{31}{12\pi} - \frac{11}{2\pi} \ln 2 - \frac{\pi}{6} - 12\pi \left(\frac{13}{144} - 8x_1 - P \right) \right) \right. \right. \\ &\quad \left. \left. + \left(\frac{\ln 2}{3\pi} - 4\pi P_4 - \frac{5}{18\pi} + 32\pi x_2 \right) n_f \right] \right\} \end{aligned} \tag{4.20}$$

to order $(\alpha_V)^2$. This equation is then taken to be the exact definition of $\alpha_P(2/a)$. When solving this quadratic equation complex roots are obtained and so the real part must be taken for α_P. Table (4.4) shows NRQCD simulation results for $-\ln W_{1,1}$ and subsequent values of $\alpha_P^{(n_f)}(2/a)$.

In a similar manner to that of section 4.3, the three-loop beta function appropriate to the plaquette scheme was used to evolve the couplings to the scale 8.2 GeV, after which extrapolation of the inverse couplings in n_f gave

$$\alpha_P^{(3)}(8.2\,\text{GeV}) = \begin{cases} 0.1918(44) & \text{for } \Upsilon' - \Upsilon \text{ splitting} \\ 0.1909(30) & \text{for } \chi_b - \Upsilon \text{ splitting} \end{cases}$$

β	n_f	$-\ln W_{1,1}$	$\alpha_P^{(n_f)}(2/a)$
6.0	0	0.5214	0.2359
5.6	2	0.5709	0.2329

Table 4.4: Expectation values of the 1×1 Wilson loop and corresponding $\alpha_P^{(n_f)}$ values at scale $2/a$ for both quenched and dynamical simulations.

Conversion to the $\overline{\mathrm{MS}}$ scheme using (4.5), followed by a similar running and matching analysis to that of section 4.4 gave the results

$$\alpha_{\overline{\mathrm{MS}}}^{(5)}(M_Z) = \begin{cases} 0.1161(17) & \text{for } \Upsilon' - \Upsilon \text{ splitting} \\ 0.1158(12) & \text{for } \chi_b - \Upsilon \text{ splitting} \end{cases}$$

Even with error estimates that neglect the n_f dependence of the $(\alpha_P^{(n_f)})^3$ term in the conversion to the $\overline{\mathrm{MS}}$ scheme, the results here only differ within 1σ from those of the last column of table (4.3) which is remarkable considering that the momentum scale $2/a$ is almost half of $3.40/a$. This then confirms that using the exact appropriate scale when extracting the plaquette coupling is not crucial to obtaining accurate results and in fact probably any scale close to $3.40/a$ would suffice.

4.4.6 Summary

The method for obtaining α_s detailed in this chapter is amongst the most accurate there is. The final quoted result from this analysis is

$$\alpha_{\overline{\mathrm{MS}}}^{(5)}(M_Z = 91.2\,\mathrm{GeV}) = 0.1171(23) \tag{4.21}$$

and is in superb agreement with the world average shown in figure (4.2). Various sources of error contributing to the final result were investigated in this section and are summarised in table (4.5). It is encouraging that the uncertainties in this table

source	uncertainty
scale factor for conversion to $\overline{\text{MS}}$ scheme	0.4%
c quark mass	0.2%
b quark mass	0.1%
correct n_f for $1/\alpha_P$ extrapolation	3.4%
scale for extraction of α_P from plaquette	1.1%

Table 4.5: Sources of systematic error and their effect on the determination of $\alpha^{(5)}_{\overline{\text{MS}}}(M_Z)$.

are so small, bordering on negligible. The only exception being the extrapolation of $1/\alpha_P$ to the correct value of n_f which can only be properly investigated when dynamical runs are undertaken having $n_f = 4$. Sources of error not investigated in this analysis, such as the dependence on the light quark mass, are dealt with in [7].

Chapter 5

Upsilon Spectroscopy at $\beta = 6.2$

The work in this chapter was performed on $24^3 \times 48$ lattices at $\beta = 6.2$. 216 quenched configurations using the standard Wilson gluonic action [56] were used, gauge fixed to Coulomb gauge, with simulations beginning on 8 origin sites per configuration as described in section 2.7.2. Equation (2.83), discussed in section 2.6.3, was used to evolve the quark propagators.

5.1 Tuning the Bare Quark Mass

Since the simulations in this chapter were performed on a lattice with a different beta value to that used for chapter 3, the lattice spacing $a(g)$ and the bare quark mass M_b^0 must be retuned. The lattice spacing is dealt with in section 5.5 while the bare quark mass is dealt with here.

An initial guess for the bare mass was obtained by equating the renormalized physical b mass, $M_b = Z_m M_b^0$, at both $\beta = 6.0$ and 6.2, i.e.

$$(Z_m M_b^0)_{6.2} = (Z_m M_b^0)_{6.0} \tag{5.1}$$

and so

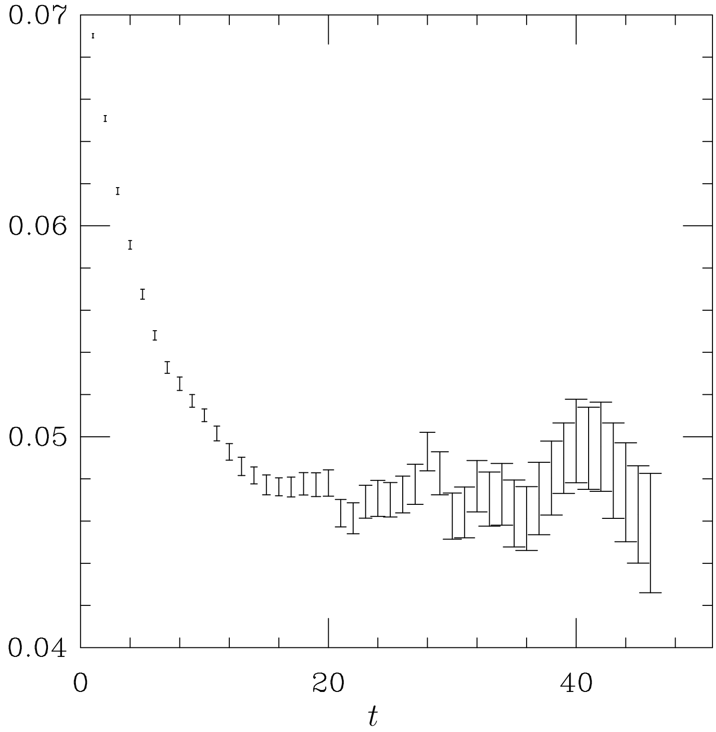

Figure 5.1: Effective mass of the ratio of a finite momentum $^3S_1$ to a zero momentum $^3S_1$.

$$(aM_b^0)_{6.2} = \frac{(a^{-1})_{6.0}}{(a^{-1})_{6.2}} \times (aM_b^0)_{6.0} \times \frac{(Z_m)_{6.0}}{(Z_m)_{6.2}}. \tag{5.2}$$

Using the value $(a^{-1})_{6.2} = 3.4$ from the $1P - 1S$ splitting obtained in a previous determination [25] along with the values $(a^{-1})_{6.0} = 2.59$ and $(aM_b^0)_{6.0} = 1.71$ from chapter 3 and values of Z_m, the mass renormalization constant, given in [57, 58], the initial guess for $(aM_b^0)_{6.2}$ was found to be 1.22.

Similar to the method in section 3.1, the bare mass was tuned from two simulations of the Υ in the $^3S_1$ channel—one having zero momentum, the other having small lattice momenta of $(1,0,0)$, $(-1,0,0)$, $(0,1,0)$, $(0,-1,0)$, $(0,0,1)$ and $(0,0,-1)$ in units of $4\pi/24a$. From the two ensembles of correlations (the dynamical one having being averaged over directions) an ensemble of correlation ratios was produced and its effective mass plot obtained, shown in figure (5.1). The plateau value reached in figure (5.1) was taken to be $4.75(8) \times 10^{-2}$. The lattice momentum of $4\pi/24a$ gives a dimensionless continuum momentum of

$$\begin{aligned} a^2\mathbf{p}^2 &= \sum_i 4\sin^2\frac{p_i a}{2} \\ &= 4\sin^2\frac{2\pi}{24} \\ &= 0.2679 \end{aligned}$$

and so using equation (3.2) the kinetic mass was found to be $aM_{kin} = 2.82(5)$. Estimating for a^{-1} the value found in [25], namely 3.4(2) GeV, yields a physical kinetic mass of 9.6(6) GeV. Since this agrees with the experimental Υ rest mass value of 9.46 GeV, $aM_b^0 = 1.22$ was considered acceptable for the simulations in this chapter.

5.2 Fitting Results for S and P States

In this section values for energies and amplitudes were extracted using the procedure discussed in section 3.2, i.e. effective mass plots were used to obtain approximate input fitting parameters for the multi-correlation routines of section 2.8.1.

In figure (5.2) effective masses are plotted against time for eight (source,sink) smearing combinations of the $^3S_1$ state. The $(loc, 1)$, $(1, loc)$ and $(1, 1)$ plots have good plateaux indicating very good ground state smearing with an approximate ground state energy value of 0.3. The $(2, loc)$ and $(3, loc)$ plots fall slowly to ground state plateaux at 0.3, indicative of good excited state smearing, while the $(2, 2)$ plot seems to plateau at around 0.5, giving an approximate value for the first excited state energy, before being masked by noise at later times. The $(3, 3)$ plot is too noisy to be able to predict the second excited state energy.

Similar plots for the $^1P_1$ state are shown in figure (5.3). Excellent ground state plateaux were obtained for the $(1, loc)$ and $(1, 1)$ plots indicating an approximate

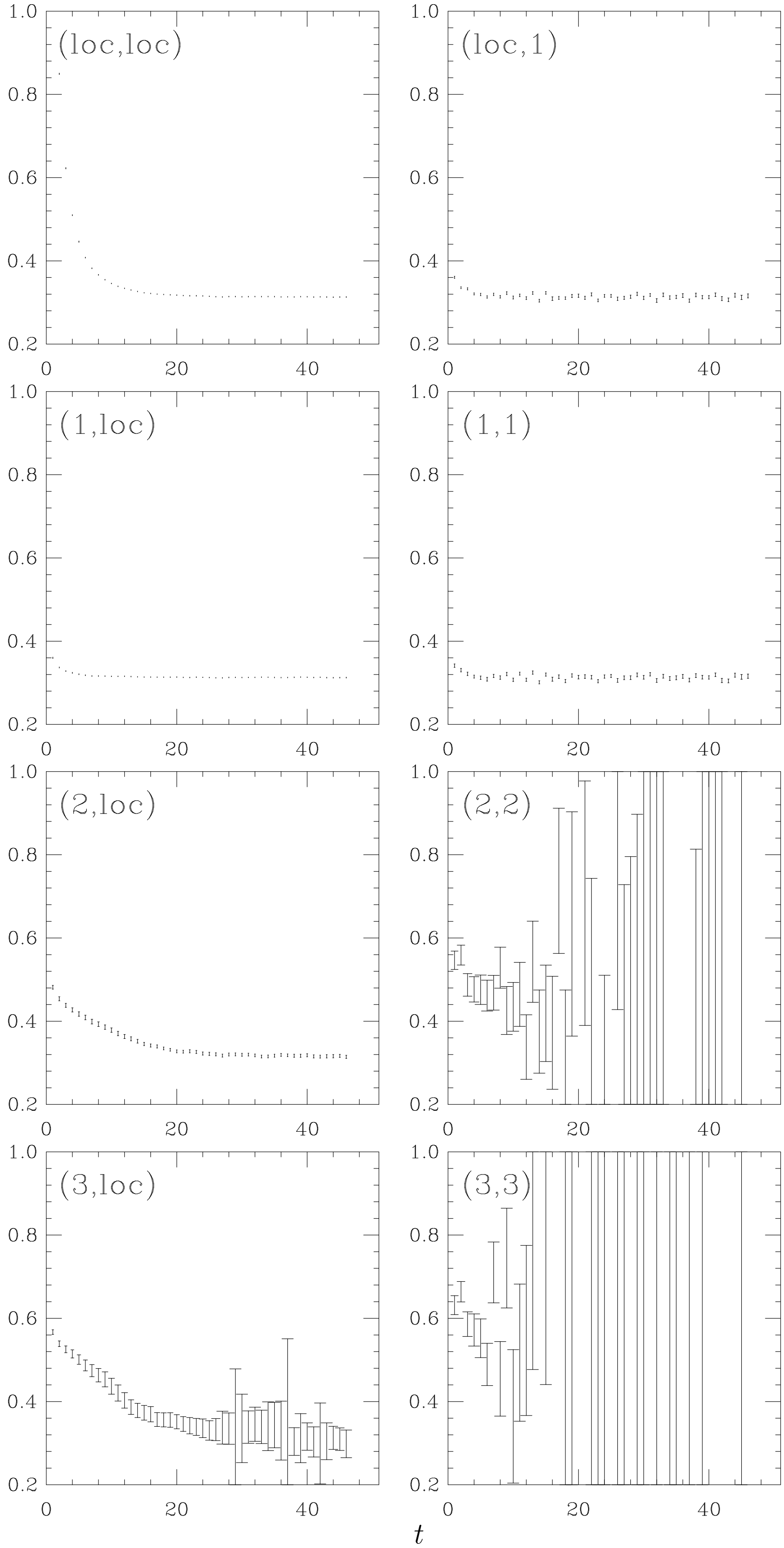

Figure 5.2: Effective masses of ${}^3S_1$ states given by their smearings, (n_{sc}, n_{sk}).

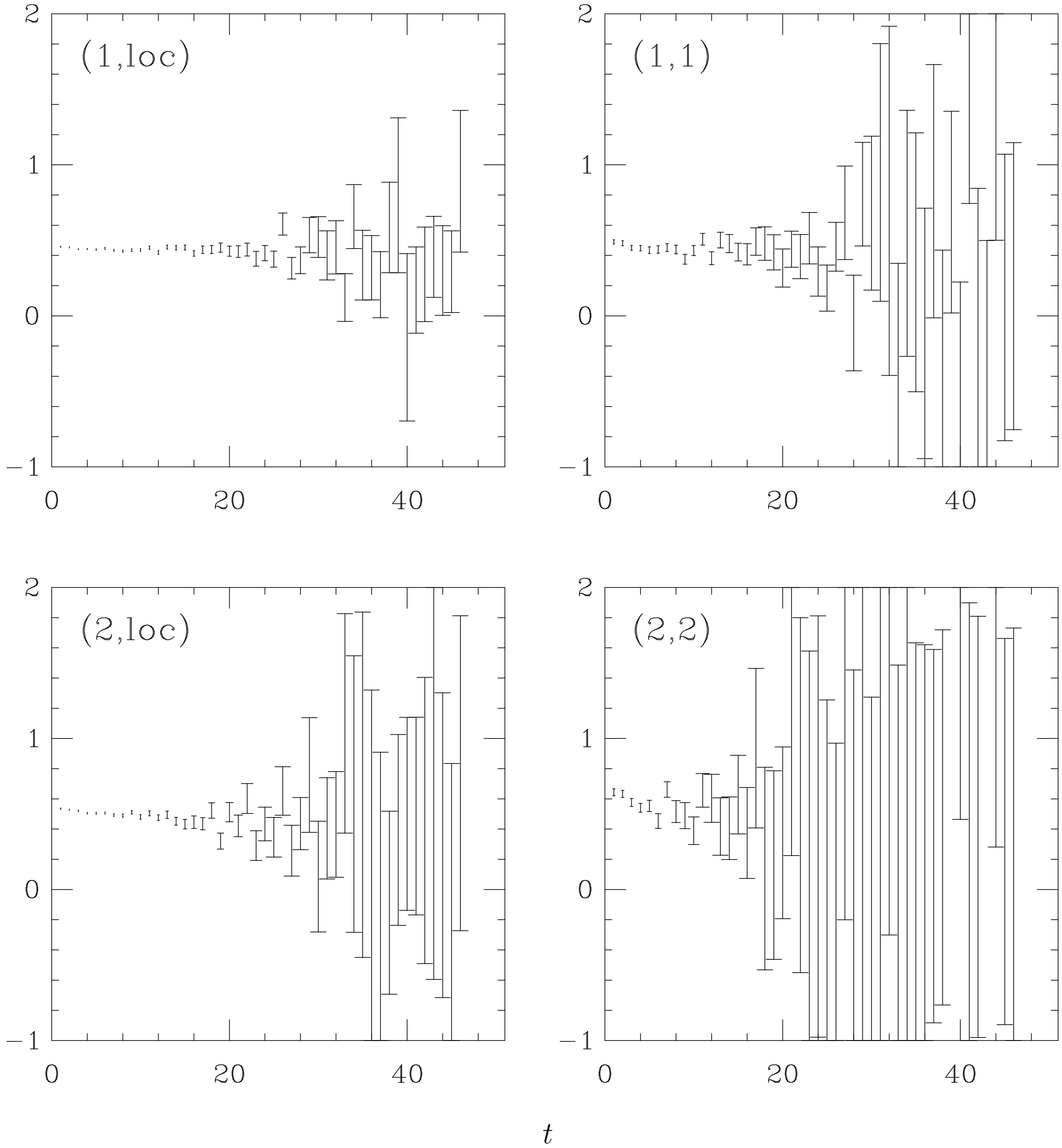

Figure 5.3: Effective masses of $^1P_1$ states given by their smearings, (n_{sc}, n_{sk}).

ground state energy of 0.4, while good excited state plateaux were obtained for the $(2, loc)$ and $(2,2)$ plots giving an approximate excited state energy value of 0.6.

The smearing combinations given in figures (5.2) and (5.3) were the only ones used for these particular states, for the simulations in this chapter, and so the multi-correlation row fitting routine was relied upon to extract energies and amplitudes for the $^1S_0$, $^3S_1$ and $^1P_1$ states.

Table (5.1) shows results obtained from row fits to the $^1S_0$ ground and excited state energies over various t_{min}/t_{max} ranges as well as the quality of fit, Q. From $t_{min} = 18$ to $t_{min} = 40$, excellent results were obtained for the ground state energy in complete agreement with each other, some of which are shown in the lower part of the table. With one correlation and with t_{min} values less than 18, the energy and amplitude results no longer form plateaux indicating the need for a second exponential to be added. This along with the addition of a second correlation with excited state smearing was done and the results for both energies are shown in the upper part of the table. Again excellent results were obtained for the ground state energy while good results were obtained for the first excited state energy. This is shown more explicitly in the t_{min} plots of figure (5.4), constructed for the two correlation case. Here, the top left diagram shows the steady ground state energy obtained throughout, while the bottom left diagram shows excellent results for the excited state energy up until $t_{min} = 17$. Beyond this point the signal for the first excited state has died away and so poor fits were obtained for t_{min} values in the region 18 to 26, as can be seen in the bottom left diagram, where the excited state energy is inconclusive in this region, and the bottom right diagram, where the Q values within the region are poor. From t_{min} of 27 onwards the amplitudes $a^3b(2,1)$ and $a^3b(2,2)$ coupling the $(2, loc)$ correlation with the ground and first excited states, respectively, change noticeably; $a^3b(2,2)$ becomes consistent with zero while $a^3b(2,1)$, shown in the top right diagram, increases to incorporate the decaying excited state which has now become flat in this region. With the change

	N_{exp}	t_{min}/t_{max}	aE_1	aE_2	Q
fits to (1,loc)	2	2/47	0.3028(2)	0.480(3)	0.34
and (2,loc)		3/47	0.3027(2)	0.480(3)	0.33
correlations		4/47	0.3027(2)	0.480(3)	0.28
		5/47	0.3028(2)	0.481(4)	0.26
		6/47	0.3028(2)	0.481(4)	0.34
		7/47	0.3028(2)	0.476(5)	0.41
		8/47	0.3028(2)	0.478(6)	0.38
		9/47	0.3027(3)	0.479(7)	0.38
		10/47	0.3027(3)	0.474(9)	0.40
		11/47	0.3026(3)	0.471(10)	0.37
		12/47	0.3027(3)	0.465(12)	0.31
		13/47	0.3026(3)	0.459(14)	0.27
		14/47	0.3026(3)	0.461(15)	0.31
		15/47	0.3027(3)	0.443(16)	0.38
		16/47	0.3027(3)	0.438(18)	0.24
		17/47	0.3028(3)	0.461(26)	0.25
fits to (1,loc)	1	18/47	0.3027(3)		0.82
correlation		19/47	0.3027(3)		0.78
		20/47	0.3027(3)		0.75
		21/47	0.3027(3)		0.80
		22/47	0.3027(3)		0.77
		23/47	0.3027(3)		0.73
		24/47	0.3027(3)		0.68
		25/47	0.3027(3)		0.62

Table 5.1: Examples of simultaneous row fits to one and two $^1S_0$ correlations.

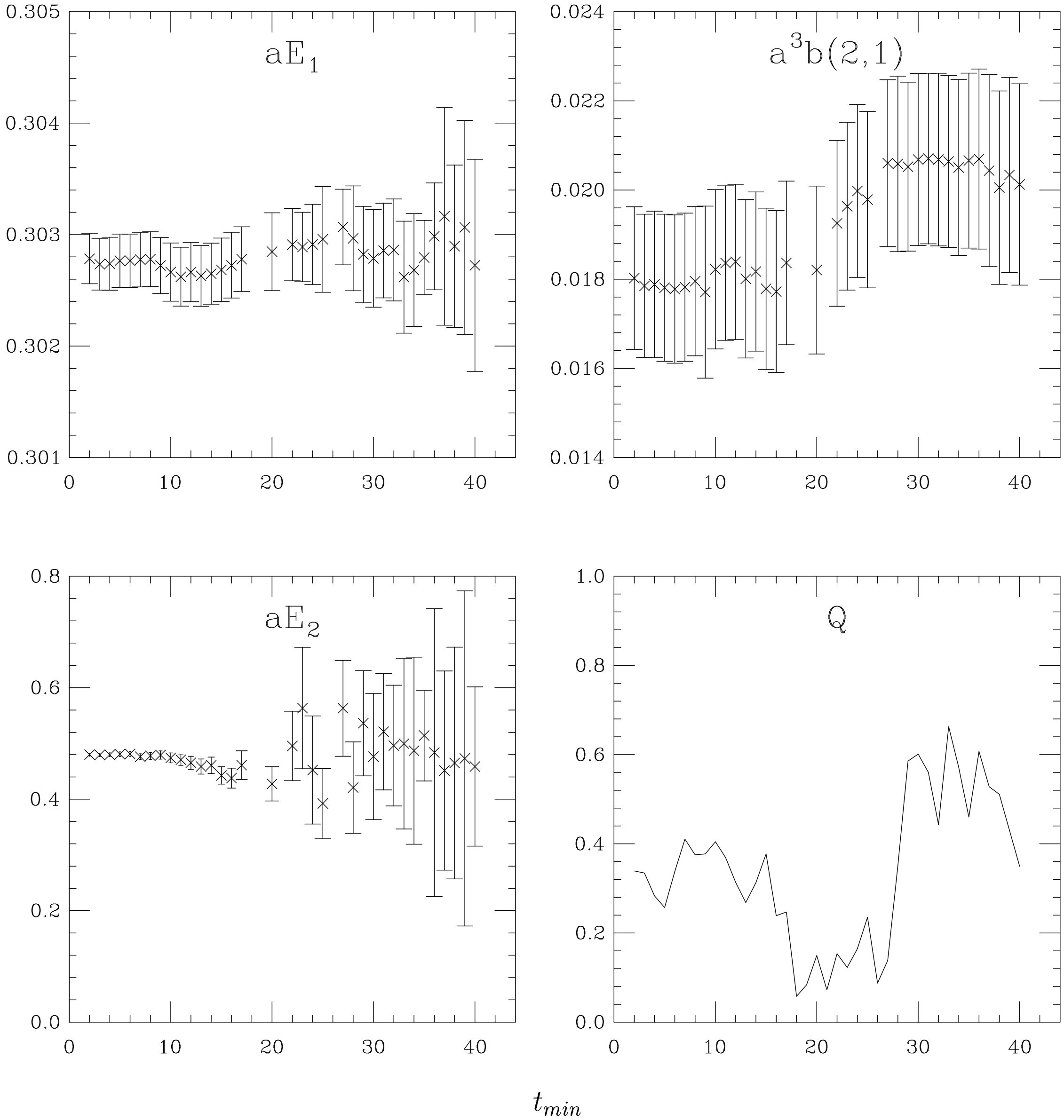

Figure 5.4: From top left to bottom right; ground state energy aE_1, amplitude $a^3b(2,1)$, first excited state energy aE_2 and quality of fit Q; obtained from fits to two ${}^1S_0$ correlations, a ll plotted against t_{min} ($t_{max} = 47$). Points are omitted if the corresponding Q is less than 0.1.

in these amplitude values, the data became easier to fit to resulting in high Q values as can be seen in the latter part of the Q plot. Although with no excited state signal, the fits in this region are untrustworthy and so the fit with $t_{min} = 8$ was taken as the best determination of the ground and first excited state energies.

Table (5.2) shows similar results obtained from row fits to the $^3S_1$ ground and excited state energies. Excellent results were obtained fitting to one correlation using one exponential, some of which are given in the lower part of the table. Again, the energy and amplitude values began to rise for values of t_{min} less than 20 necessitating a second exponential. The upper part of the table shows results obtained with two correlations and two exponentials for t_{min} values between 2 and 19. Excellent ground state results were obtained as can be seen in the top left t_{min} plot of figure (5.5), constructed for the two correlation case, while good excited state results can be seen in the top right and bottom left plots up until $t_{min} = 19$ whereupon the signal for the first excited state dies. The Q values for the two correlation/two exponential fits are rather poor for t_{min} values less than 24 and only rise at this point because the amplitude $a^3b(2,2)$ coupling the $(2, loc)$ correlation with the first excited state changes to become consistent with zero. The reason for the relatively poor but consistent Q values is explained by the bottom right plot of figure (5.5) where it can be seen that between the t_{min} values of 5 and 23, the χ^2 per degree of freedom is relatively higher than expected. This is probably due both to the fact that the statistics for the $\beta = 6.2$ simulations were relatively low—216 configurations for results having a t_{max} of 47 and also to the fact that noise from the multi-origin smearing (see section 2.7.2) appears to affect the $^3S_1$ and $^1P_1$ states more so than for the $^1S_0$ state. Although the χ^2/dof values fall rapidly at earlier t_{min} values indicating the need for a third exponential, they become steady from $t_{min} = 5$ onwards and so this steadiness was taken as a better indicator of good fitting rather than the corresponding Q values. The fit with $t_{min} = 9$ was subsequently taken as the best determination of the ground and first excited state energies.

	N_{exp}	t_{min}/t_{max}	aE_1	aE_2	Q
fits to (1,loc)	2	2/47	0.3128(3)	0.517(3)	0.00
and (2,loc)		3/47	0.3130(3)	0.508(3)	0.00
correlations		4/47	0.3131(3)	0.504(4)	0.00
		5/47	0.3131(3)	0.499(4)	0.02
		6/47	0.3132(3)	0.499(5)	0.04
		7/47	0.3133(3)	0.493(6)	0.10
		8/47	0.3133(3)	0.491(7)	0.08
		9/47	0.3132(3)	0.488(8)	0.07
		10/47	0.3131(3)	0.494(10)	0.07
		11/47	0.3130(3)	0.491(11)	0.06
		12/47	0.3130(4)	0.483(13)	0.05
		13/47	0.3131(4)	0.490(17)	0.05
		14/47	0.3133(4)	0.502(20)	0.04
		15/47	0.3133(4)	0.491(26)	0.02
		16/47	0.3132(4)	0.464(28)	0.02
		17/47	0.3132(4)	0.518(45)	0.02
		18/47	0.3133(4)	0.463(48)	0.02
		19/47	0.3135(4)	0.482(93)	0.02
fits to (1,loc)	1	20/47	0.3130(4)		0.43
correlation		21/47	0.3129(4)		0.46
		22/47	0.3129(4)		0.42
		23/47	0.3130(4)		0.55
		24/47	0.3129(4)		0.51
		25/47	0.3129(4)		0.45

Table 5.2: Examples of simultaneous row fits to one and two $^3S_1$ correlations.

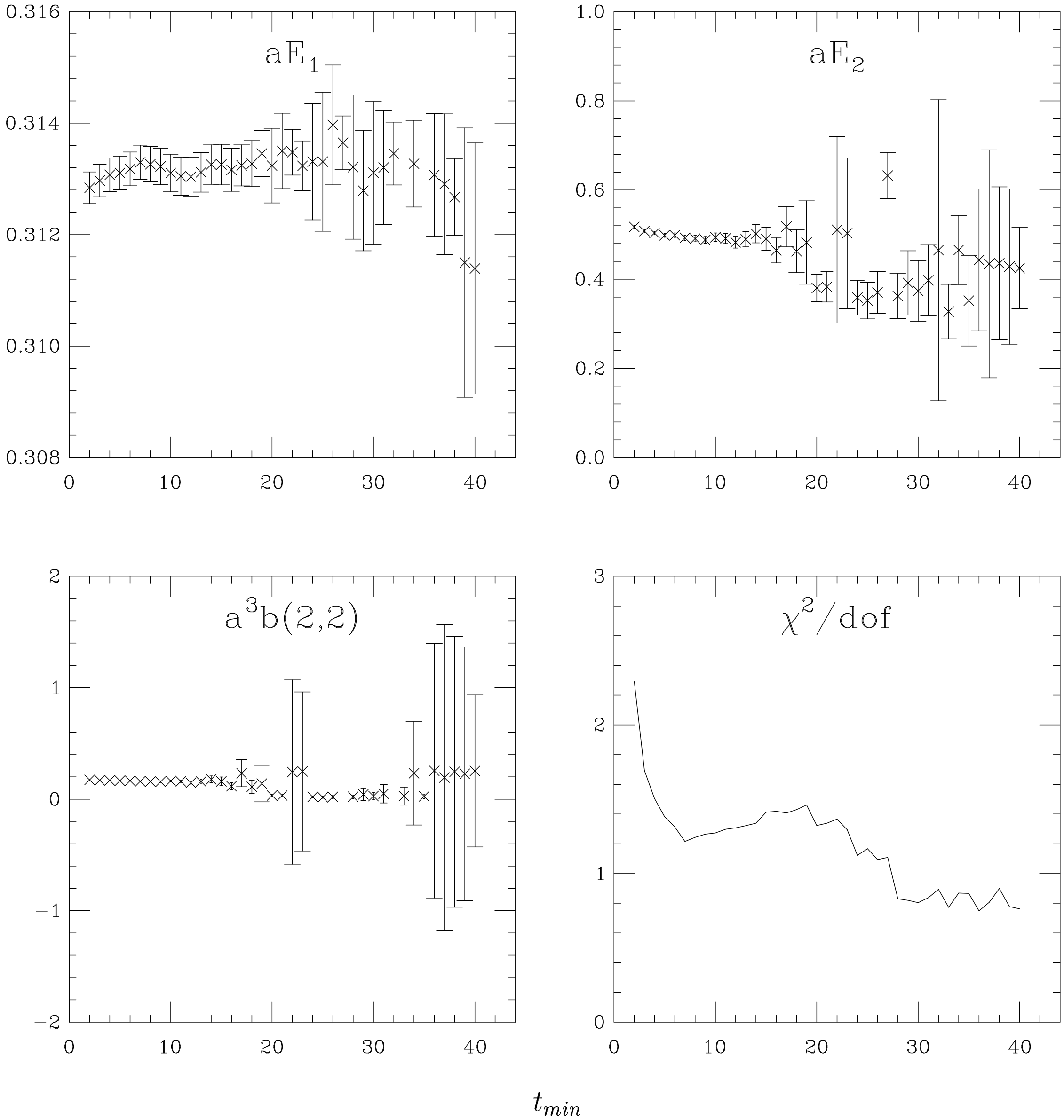

Figure 5.5: From top left to bottom right; ground state energy aE_1, first excited state energy aE_2, amplitude $a^3b(2,2)$ and chi-square per degree of freedom χ^2/dof; obtained from fit s to two $^3S_1$ correlations, all plotted against t_{min} ($t_{max} = 47$). Some rouge fit points have been omitted.

Fits with three correlations and three exponentials were undertaken in an attempt to extract a value for the second excited state energy of the $^3S_1$, some of the results being shown in table (5.3). For $t_{max} = 47$ the Q values were in general found to be very poor up until $t_{min} = 24$, presumably because of the large size of the covariance matrix since the results with $t_{max} = 24$ give reasonable Q values, and so the χ^2/dof was used as a guide to good fits. A variety of energies and amplitudes along with the χ^2/dof are shown for the $t_{max} = 47$ case in the t_{min} plots of figure (5.6). Here, small plateaux seem to be apparent between the t_{min} values of 2 and 5 indicating a short lived second excited state, verified by the sharp change in χ^2/dof of figure (5.5) at early t_{min} values. The signal for the second excited state seems to have disappeared beyond $t_{min} = 5$ and as a consequence the fits with t_{min} between 6 and 21 yield fluctuating values for the second excited state energy and the amplitudes $a^3b(3,3)$ and $a^3b(3,2)$ coupling the $(3, loc)$ correlation with the second and third exponentials. Beyond $t_{min} = 21$, the amplitudes $a^3b(3,3)$ and $a^3b(3,2)$ are consistent with zero while $a^3b(3,1)$ is steady indicating that only the ground state signal remains in the $(3, loc)$ correlation data. Shown in the top left diagram of figure (5.6), the ground state energy values plateau fairly well, however the results for the first excited state are not as good; after short plateaux, there is a turbulent time between the t_{min} values of 6 and 11 where the first excited state energy and the amplitude $a^3b(2,2)$ fluctuate wildly before settling down between $t_{min} = 11$ and $t_{min} = 28$ to values inconsistent with those obtained from the two correlation/two exponential fits. Only for t_{min} values greater than 28, when the amplitude $a^3b(2,2)$ becomes consistent with zero, does the first excited state energy become consistent again with the value obtained from the two correlation fits. Since the χ^2/dof does not change dramatically at any point over the full range of t_{min} values, the fits with t_{min} less than 6 were deemed acceptable in determining the second excited state energy. $t_{min} = 5$ was chosen as the best determination.

Table (5.5) and figure (5.7) show results obtained from similar row fits to

	N_{exp}	t_{min}/t_{max}	aE_1	aE_2	aE_3	Q
fits to (1,loc),	3	2/24	0.3138(6)	0.453(11)	0.626(14)	6×10^{-4}
(2,loc) and		2/47	0.3144(3)	0.468(9)	0.636(13)	9×10^{-8}
(3,loc)		3/24	0.3138(6)	0.461(14)	0.614(18)	0.01
correlations		3/47	0.3143(3)	0.478(9)	0.641(20)	8×10^{-7}
		4/24	0.3137(6)	0.459(17)	0.613(25)	0.01
		4/47	0.3143(3)	0.486(12)	0.669(38)	3×10^{-7}
		5/24	0.3138(7)	0.474(23)	0.611(40)	0.01
		5/47	0.3144(3)	0.477(16)	0.649(40)	2×10^{-10}
		6/24	0.3136(9)	0.432(30)	0.561(18)	0.03
		6/47	0.3141(4)	0.392(23)	0.557(11)	7×10^{-8}
		7/24	0.3132(8)	0.472(28)	0.599(44)	0.07
		7/47	0.3141(4)	0.443(36)	0.596(38)	4×10^{-7}
		8/24	0.3134(9)	0.454(31)	0.609(46)	0.07
		8/47	0.3136(6)	0.377(28)	0.573(21)	2×10^{-7}
		9/24	0.3131(9)	0.457(28)	0.679(75)	0.14
		9/47	0.3136(5)	0.390(32)	0.603(37)	3×10^{-7}
		10/24	0.3125(11)	0.432(36)	0.680(90)	0.23
		10/47	0.3135(5)	0.411(34)	0.723(116)	5×10^{-7}

Table 5.3: Examples of simultaneous row fits to three $^3S_1$ correlations.

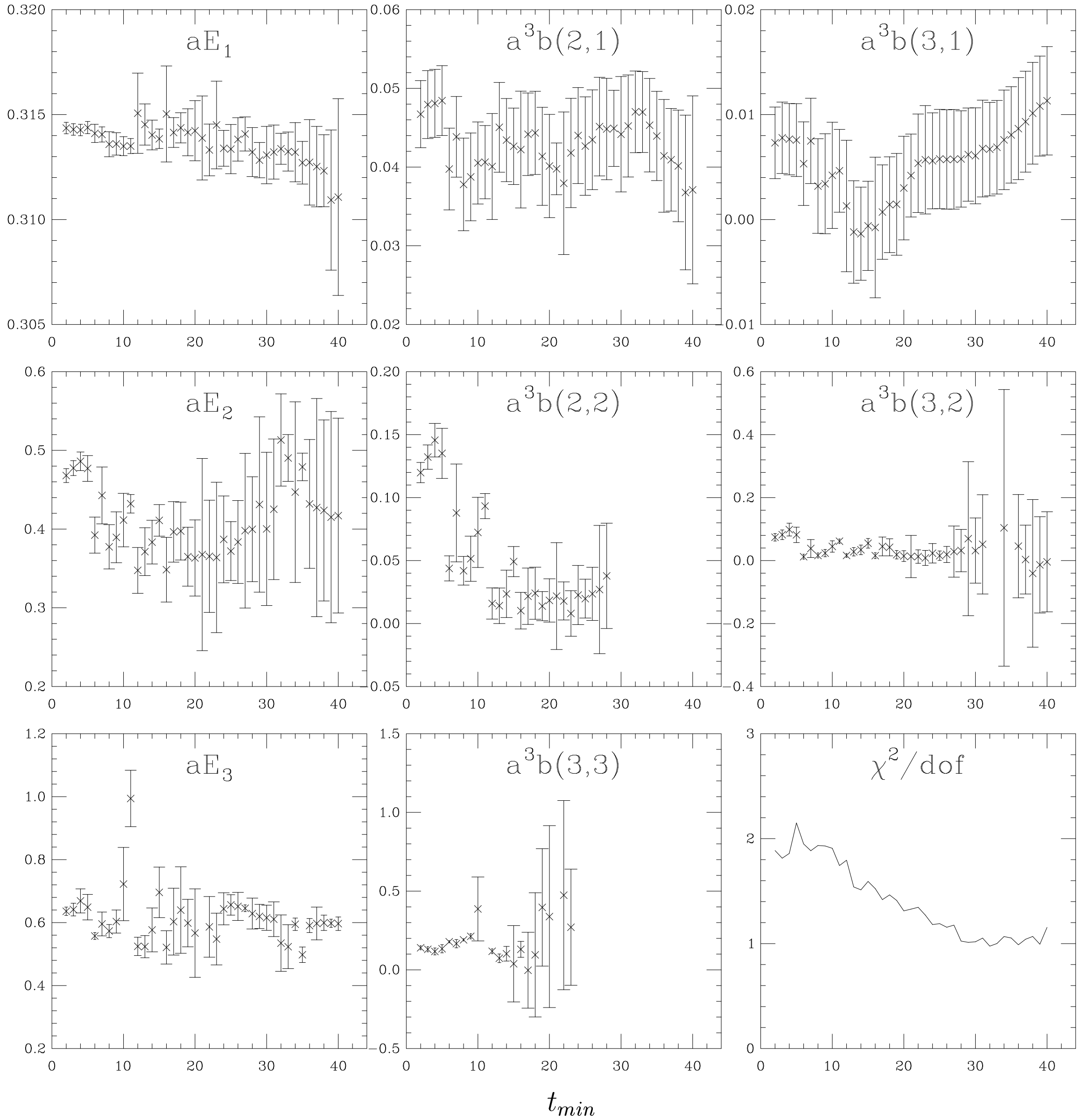

Figure 5.6: From top left to bottom right; ground state energy aE_1, amplitude $a^3b(2,1)$, amplitude $a^3b(3,1)$, first excited state energy aE_2, amplitude $a^3b(2,2)$, amplitude $a^3b(3,2)$, second excited state energy aE_3, amplitude $a^3b(3,3)$ and chi-square per degree of freedom χ^2/dof; obtained from fits to three $^3S_1$ correlations, all plotted against t_{min} ($t_{max} = 47$). Some fit points with large errors have been omitted.

${}^1P_1$ correlations. Again, the χ^2/dof was used as a guide to good fitting for the $t_{max} = 47$ fits rather than the Q values which were found to be too small up until $t_{min} = 28$. Following a similar pattern to the analysis of the ${}^1S_0$ and ${}^3S_1$ states, it can be seen from the bottom left plot in figure (5.7) that the signal for the excited ${}^1P_1$ state dies beyond $t_{min} = 11$, and from the bottom right plot that acceptable fits were obtained over a large range of t_{min} owing to the relative steadiness of the χ^2/dof. $t_{min} = 9$ was taken as the best determination of the ground state energy, while although $t_{min} = 6$ seems a good determination of the excited state, fits with three exponentials to two correlations gave the higher value of 0.60(7) for this excited state. Since this higher value encompasses the value from the two exponential fits, it was taken to be a better determination.

All the simulation mass results are collected together in table (5.4). Bootstrap row fit results are also shown in the third column of this table. The central values for these results are consistent with those of the ordinary row fits, however the errors are generally larger by a factor of $1\frac{1}{2} \sim 2$. It is not clear whether these larger errors are a result of the multi-origin smearing noise or the low statistics relative to the size of the covariance matrix.

state	simulation result	bootstrap result
1^1S_0	0.3028(2)	0.3029(4)
2^1S_0	0.478(6)	0.479(9)
1^3S_1	0.3132(3)	0.3132(6)
2^3S_1	0.488(8)	0.490(12)
3^3S_1	0.65(4)	0.64(11)
1^1P_1	0.438(5)	0.438(12)
2^1P_1	0.60(7)	0.61(5)

Table 5.4: Dimensionless masses.

	N_{exp}	t_{min}/t_{max}	aE_1	aE_2	Q
fits to (1,loc)	2	3/24	0.435(5)	0.569(13)	0.27
and (2,loc)		3/32	0.431(4)	0.567(12)	0.01
correlations		3/47	0.434(4)	0.577(12)	2×10^{-5}
		4/24	0.434(6)	0.549(15)	0.39
		4/32	0.429(5)	0.549(13)	0.01
		4/47	0.433(5)	0.547(13)	4×10^{-5}
		5/24	0.435(6)	0.560(19)	0.35
		5/32	0.433(5)	0.555(17)	0.02
		5/47	0.436(5)	0.557(17)	3×10^{-5}
		6/24	0.436(7)	0.572(25)	0.30
		6/32	0.431(6)	0.562(21)	0.01
		6/47	0.431(5)	0.567(21)	4×10^{-5}
		7/24	0.443(7)	0.593(34)	0.38
		7/32	0.439(7)	0.580(29)	0.02
		7/47	0.442(6)	0.589(29)	5×10^{-4}
		8/24	0.445(7)	0.658(58)	0.46
		8/32	0.441(7)	0.631(48)	0.03
		8/47	0.443(6)	0.634(43)	8×10^{-4}
		9/24	0.439(7)	0.716(86)	0.64
		9/32	0.435(7)	0.664(66)	0.05
		9/47	0.438(5)	0.712(68)	1×10^{-3}
		10/24	0.433(11)	0.649(118)	0.57
		10/32	0.433(9)	0.642(99)	0.03
		10/47	0.439(6)	0.722(114)	9×10^{-4}

Table 5.5: Examples of simultaneous row fits to two ${}^1P_1$ correlations.

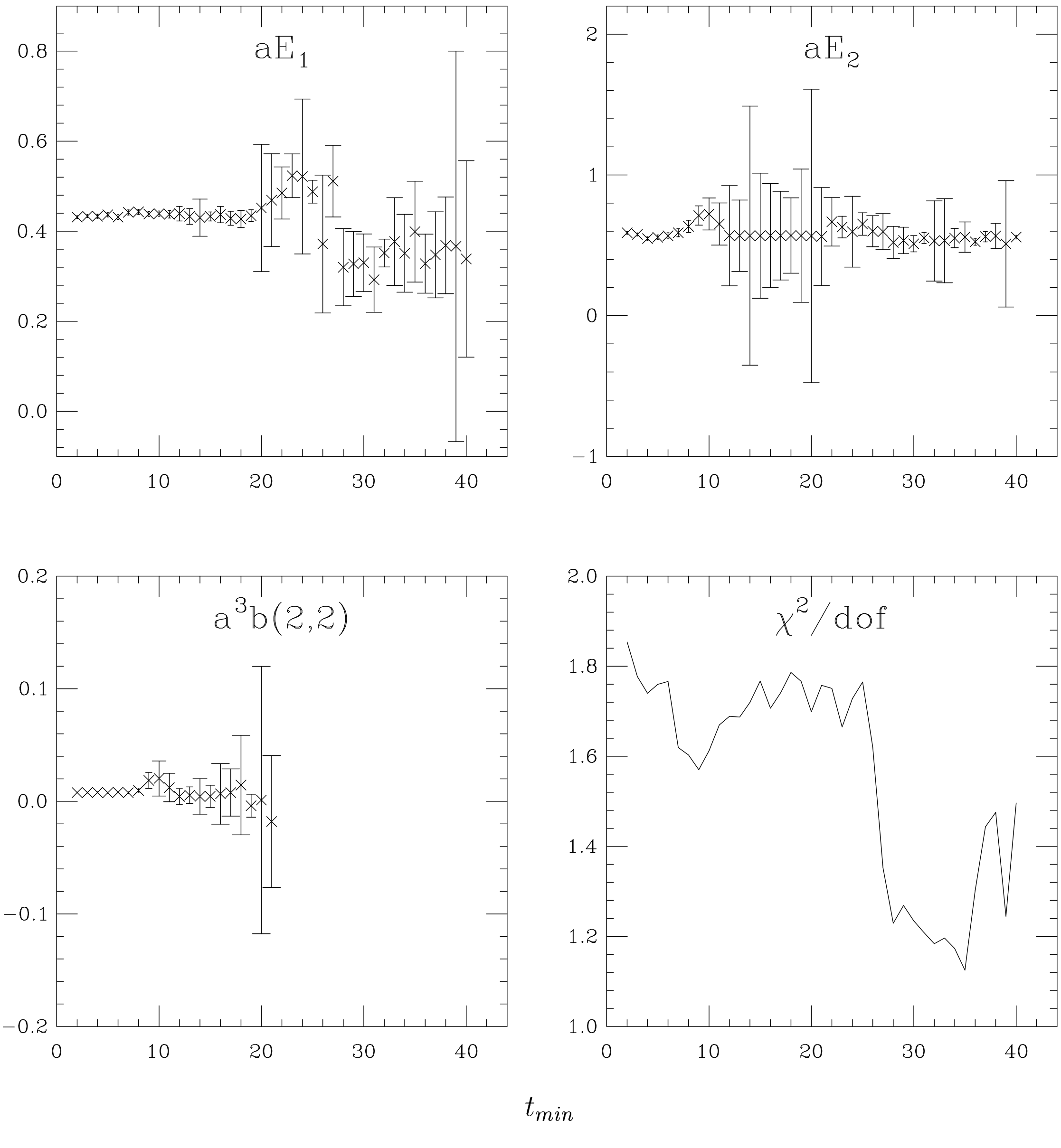

Figure 5.7: From top left to bottom right; ground state energy aE_1, first excited state energy aE_2, amplitude $a^3b(2,2)$ and chi-square per degree of freedom χ^2/dof; obtained from fits to two ${}^1P_1$ correlations, all plotted against t_{min} ($t_{max} = 47$). Some fit points with large errors have been omitted.

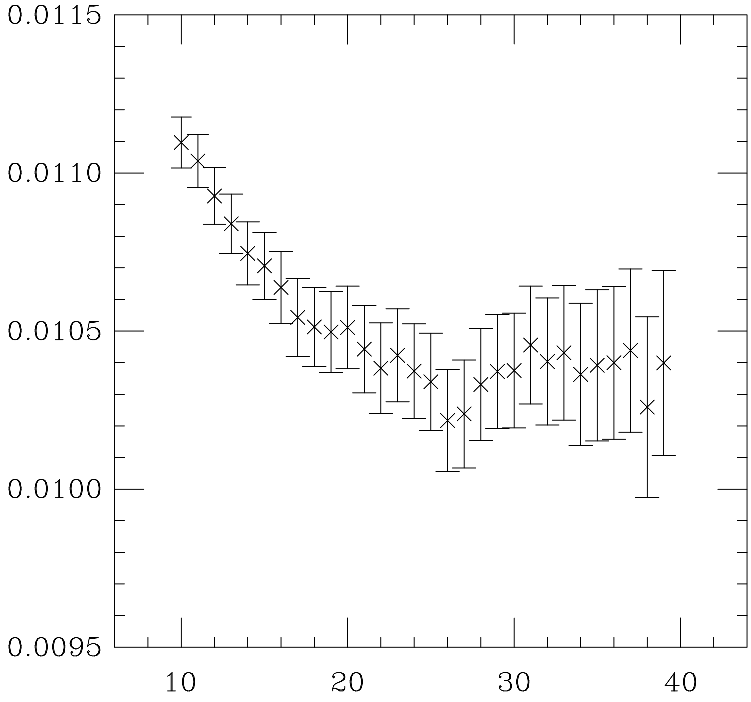

Figure 5.8: ${}^3S_1 - {}^1S_0$ splitting against t_{min} ($t_{max} = 47$).

5.3 Fitting Results for Spin Splittings

As discussed in section 3.3, spin splittings arise from the spin terms (3.3) and with a dimensionless mass of $aM = 1.22$ at $\beta = 6.2$, these terms have order of magnitude 0.0008 and 0.003 respectively. The typical error from row fitting to the ${}^1S_0$ and ${}^3S_1$ ground states is around 0.002/0.004 and for the ${}^1P_1$ ground state, around 0.005, therefore the ratio fitting procedure described in section 3.3 was employed to obtain estimates of the spin splitting energies.

Shown in table (5.6) are splitting energies and Q values from ratio fits over various t_{min}/t_{max} ranges to the ${}^3S_1 - {}^1S_0$ hyperfine splitting. The Q values are poor presumably because the multi-origin noise does not allow a good correlation to be obtained between the ${}^1S_0$ and ${}^3S_1$ states, however they are reasonably steady from $t_{min} = 14$ onwards. The results are plotted against t_{min} in figure (5.8) where it can be seen that they plateau beyond $t_{min} = 21$. The result at $t_{min} = 22$ was

	N_{exp}	t_{min}/t_{max}	$a\delta E$	Q
fits to ratio	1	10/47	0.01110(8)	2×10^{-7}
of (1,loc)		11/47	0.01104(8)	2×10^{-6}
correlations		12/47	0.01093(9)	3×10^{-5}
		13/47	0.01084(9)	3×10^{-4}
		14/47	0.01075(10)	2×10^{-3}
		15/47	0.01071(11)	2×10^{-3}
		16/47	0.01064(11)	2×10^{-3}
		17/47	0.01054(12)	4×10^{-3}
		18/47	0.01051(13)	5×10^{-3}
		19/47	0.01050(13)	3×10^{-3}
		20/47	0.01051(13)	3×10^{-3}
		21/47	0.01044(14)	3×10^{-3}
		22/47	0.01038(14)	5×10^{-3}
		23/47	0.01042(15)	5×10^{-3}
		24/47	0.01037(15)	8×10^{-3}
		25/47	0.01034(15)	7×10^{-3}
		26/47	0.01022(16)	2×10^{-2}
		27/47	0.01024(17)	2×10^{-2}
		28/47	0.01033(18)	4×10^{-2}
		29/47	0.01037(18)	4×10^{-2}
		30/47	0.01038(18)	3×10^{-2}

Table 5.6: Examples of ratio fits to the ${}^3S_1 - {}^1S_0$ splitting.

taken as the best determination of this hyperfine splitting.

Like section 3.3, for evaluation of P state splittings advantage was taken of the maximum correlation between particular polarizations of the ${}^1P_1$ state with those of the ${}^3P$ states. The effective mass plots of figure (5.9) allowed a preliminary assessment of the quality of the data for selected states and indicated that a t_{max} value of 20 should be used for the ratio fitting to avoid fitting to noise.

Example results of ratio fits to P splittings are shown in tables (5.7) through (5.10) where it can be seen that the Q values are extremely high, possibly due to the jackknifing ratio procedure giving covariance matrix entries that are essentially too large. In figure (5.10) the dimensionless splittings have been plotted against time. All four plots give good plateaux with correlation errors in evidence. Again, estimates for the splittings were taken at the t_{min} values for which the splittings began to plateau.

Results for all the ratio fits are given in table (5.11) along with average splittings between particular channels. Two errors are given for the average splittings; the first is a statistical error typical of the individual splittings while the second is a systematic error accounting for the spread of the central values of the individual splittings.

Results relative to the spin-average of the ${}^3P$ states, ${}^3P_{\mathrm{CM}}$(defined by (3.5)), were calculated using the same procedure as in section 3.3 and are shown in table (5.12), where the final errors were obtained by taking all contributing errors in quadrature. These results are shown diagramatically in section 5.5.

5.4 Wavefunctions at the Origin

Values extracted for the ${}^1S_0$ and ${}^3S_1$ wavefunctions at the origin can be used in perturbative estimates of many quantities, amonst them the S state hyperfine splitting. However, possibly their most important use, as far as the work of this thesis is concerned, is in perturbative estimates of the $\mathcal{O}(a^2)$ corrections to the

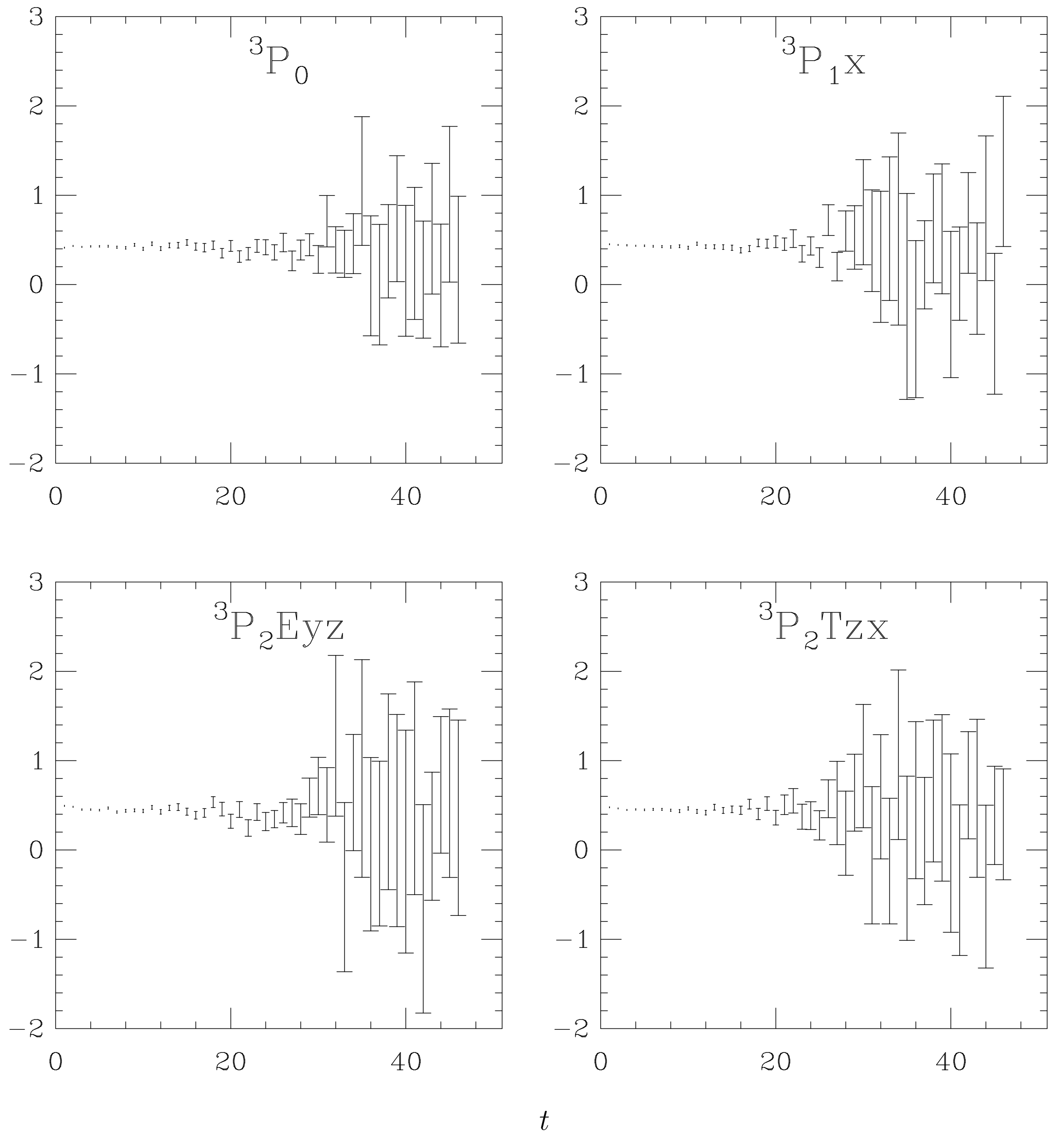

Figure 5.9: Effective masses of the $^3P_0$ state and some $^3P_1$ and $^3P_2$ polarization states, all of whi ch have the $(1, loc)$ smearing combination.

	N_{exp}	t_{min}/t_{max}	$a\delta E$	Q
fits to ratio	1	2/20	0.012(6)	1.00
of (1,1)		3/20	0.012(7)	1.00
correlations		4/20	0.013(8)	1.00
		5/20	0.013(10)	1.00
		6/20	0.016(11)	1.00
		7/20	0.014(13)	1.00
		8/20	0.013(15)	1.00
		9/20	0.013(16)	1.00
		10/20	0.016(19)	1.00
		11/20	0.008(22)	1.00
		12/20	0.015(27)	1.00

Table 5.7: Examples of ratio fits to the ${}^1P_1z - {}^3P_0$ splitting.

	N_{exp}	t_{min}/t_{max}	$a\delta E$	Q
fits to ratio	1	2/20	0.0019(63)	1.00
of (1,1)		3/20	0.0017(67)	1.00
correlations		4/20	0.0016(71)	1.00
		5/20	0.0013(75)	1.00
		6/20	0.0018(85)	1.00
		7/20	0.002(10)	1.00
		8/20	0.002(12)	1.00
		9/20	0.004(14)	1.00
		10/20	0.003(16)	1.00
		11/20	$-0.002(19)$	1.00

Table 5.8: Examples of ratio fits to the ${}^1P_1y - {}^3P_1x$ splitting.

	N_{exp}	t_{min}/t_{max}	$a\delta E$	Q
fits to ratio	1	2/20	0.0094(41)	1.00
of (1,loc)		3/20	0.0077(44)	1.00
correlations		4/20	0.0072(47)	1.00
		5/20	0.0072(48)	1.00
		6/20	0.0069(50)	1.00
		7/20	0.0067(56)	1.00
		8/20	0.0062(60)	1.00
		9/20	0.0066(65)	1.00
		10/20	0.0071(78)	1.00
		11/20	0.0055(89)	1.00
		12/20	0.0062(96)	1.00

Table 5.9: Examples of ratio fits to the ${}^3P_2Tyz - {}^1P_1y$ splitting.

	N_{exp}	t_{min}/t_{max}	$a\delta E$	Q
fits to ratio	1	2/20	0.0093(39)	0.98
of (1,loc)		3/20	0.0072(40)	1.00
correlations		4/20	0.0069(43)	1.00
		5/20	0.0071(49)	0.99
		6/20	0.0074(55)	0.99
		7/20	0.0060(59)	0.99
		8/20	0.0076(75)	0.98
		9/20	0.0067(86)	0.97
		10/20	0.0109(107)	0.96
		11/20	0.0090(128)	0.94

Table 5.10: Examples of ratio fits to the ${}^3P_2Eyz - {}^1P_1z$ splitting.

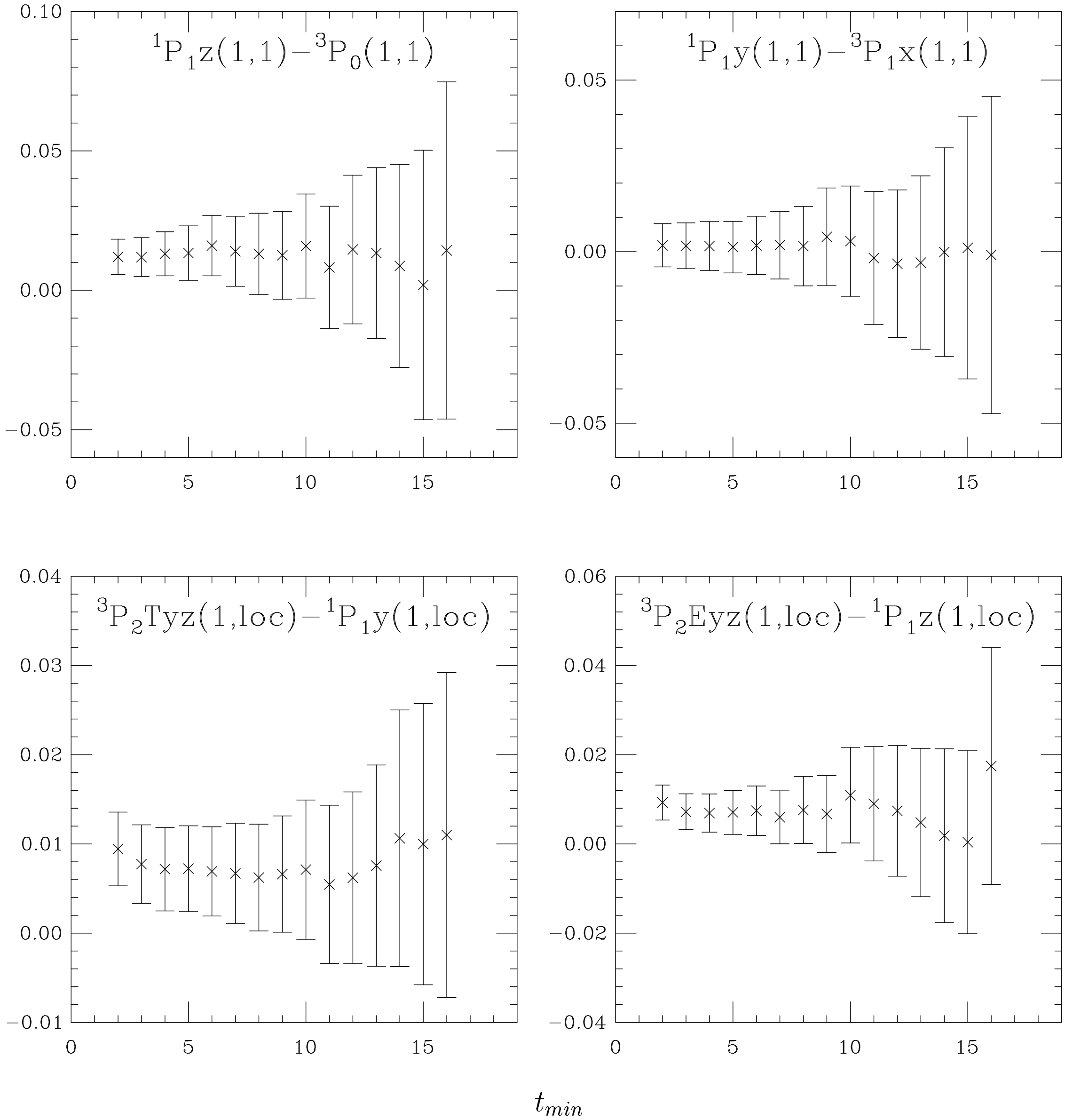

Figure 5.10: Examples of P state splittings against t_{min} ($t_{max} = 20$)

splitting	simulation result	average result
${}^3P_2Tzx(1,loc) - {}^1P_1x(1,loc)$	0.0060(52)	0.0076(41)(7)
${}^3P_2Tyz(1,loc) - {}^1P_1y(1,loc)$	0.0072(47)	
${}^3P_2Ezx(1,loc) - {}^1P_1z(1,loc)$	0.0083(41)	
${}^3P_2Eyz(1,loc) - {}^1P_1z(1,loc)$	0.0072(40)	
${}^1P_1x(1,loc) - {}^3P_1y(1,loc)$	0.0027(38)	0.0028(42)(10)
${}^1P_1y(1,loc) - {}^3P_1x(1,loc)$	0.0039(42)	
${}^1P_1y(1,1) - {}^3P_1x(1,1)$	0.0019(63)	
${}^1P_1z(1,loc) - {}^3P_0(1,loc)$	0.0139(49)	0.0130(49)(10)
${}^1P_1z(1,1) - {}^3P_0(1,1)$	0.0120(64)	

Table 5.11: Individual dimensionless splittings with quantum numbers, polarizations and smearing combinations specified. For the results in the third column the first error is statistical while the second error is systematic.

splitting	calculated result
${}^3P_2 - {}^3P_{\mathrm{CM}}$	0.0058(24)
${}^3P_{\mathrm{CM}} - {}^3P_1$	0.0046(37)
${}^3P_{\mathrm{CM}} - {}^3P_0$	0.0148(52)
${}^3P_{\mathrm{CM}} - {}^1P_1$	0.0018(28)

Table 5.12: Dimensionless splittings to the ${}^3P_{\mathrm{CM}}$.

gluonic action (see equation (4.1)).

Two methods were used to extract values for the wavefunction at the origin; the first used values of $a^3 b(n_{sc}, m)$ and $a^{3/2} a(n_{sc}, m)$ as in section 3.4, the $a^{3/2} a(n_{sc}, m)$ values being obtained from a matrix fit to the four correlations having (n_{sc}, n_{sk}) equal to (loc, loc), $(loc, 1)$, $(1, loc)$ and $(1, 1)$; the second method made use of row fits to the correlations (loc, loc), $(1, loc)$ and $(2, loc)$ in order to extract the amplitudes $a^3 b(loc, m)$ from which, using the arguments of section 3.4 and equation (2.129), values for $\Psi_m(0)$ can be found by

$$\Psi_m(0) = a(loc, m) = \sqrt{b(loc, m)} \tag{5.3}$$

Amplitudes from row and matrix fits to both the ${}^1S_0$ and ${}^3S_1$ states are shown in table (5.13), while subsequent wavefunction at the origin values are given in table (5.14). Again, as in section 3.4, multiplication by $e^{aM/2}$ was needed to alleviate the propagator code/fitting routine time misalignment. Encouraging results were obtained for $a^{3/2} a(1, 1)$ for both the ${}^3S_1$ and ${}^1S_0$ states—in each case values of around 0.8, giving corrected values of around 0.95, indicate that the ground state smearing process is targetting meson correlations to ground state decaying exponentials very well indeed. It is also encouraging that good agreement was obtained for each of the $\Upsilon(1S)$ and $\eta_b(1S)$ wavefunctions at the origin from three different calculation methods, vindicating the use of these three calculation methods.

5.5 Scaling Properties of the Spectrum

With the bare quark mass for the $\beta = 6.2$ simulations having been tuned in section 5.1, the inverse lattice spacing $a^{-1}(g)$ was determined, as in section 3.5, by matching both the $2S - 1S$ and $1P - 1S$ dimensionless splittings to experiment. Before doing this, $\mathcal{O}(a^2)$ corrections to the $\beta = 6.2$ gluonic action, calculated

m^3S_1	$a^3b(n_{sc},m)$ $n_{sc}=loc$	$n_{sc}=1$	$a^{3/2}a(n_{sc},m)$ $n_{sc}=loc$	$n_{sc}=1$
$m=1$	0.00917(9)	0.0792(7)	0.0965(7)	0.830(5)
$m=2$	0.0075(7)			
	$a^3b(n_{sc},m)$		$a^{3/2}a(n_{sc},m)$	
m^1S_0	$n_{sc}=loc$	$n_{sc}=1$	$n_{sc}=loc$	$n_{sc}=1$
$m=1$	0.01272(10)	0.0933(7)	0.1134(6)	0.826(4)
$m=2$	0.0048(11)			

Table 5.13: Examples of dimensionless amplitudes obtained from multi-exponential fits to $^1S_0$ and $^3S_1$ correlations.

	obtained from		
meson(mS)	$a^{3/2}\sqrt{b(loc,m)}$	$a^{3/2}a(loc,m)$	$a^{3/2}b(1,m)/a(1,m)$
$\Upsilon(1S)$	0.1120(5)	0.1129(8)	0.1116(12)
$\Upsilon(2S)$	0.111(5)		
$\eta_b(1S)$	0.1312(5)	0.1319(7)	0.1314(12)
$\eta_b(2S)$	0.088(10)		

Table 5.14: Dimensionless wavefunctions at the origin for ground and excited $^1S_0$ and $^3S_1$ states.

β	state	$a\Delta M_g$
5.7	1^3S_1	0.015
	2^3S_1	0.010
6.0	1^3S_1	0.0037
	2^3S_1	0.0031
6.2	1^3S_1	0.0020
	2^3S_1	0.0020

Table 5.15: Results of calculations of $\mathcal{O}(a^2)$ gluonic corrections $a\Delta M_g$ to quenched simulation masses at three β values.

for S states (P states are not affected) using the perturbative formula (4.1) and displayed in table (5.15), were added to the appropriate simulation masses. The values for these net corrections to the $2S - 1S$ and $1P - 1S$ splittings and the subsequent a^{-1} values obtained at $\beta = 6.2$ are shown in table (5.16). The dimensionless hyperfine splitting can be used as a check for the gluonic correction to the 1^3S_1 state. Combining the perturbative relations from [49] gives

$$a\Delta M_g = \frac{3}{40}(aM_b)^2 a\Delta M_{\text{hfs}}. \tag{5.4}$$

This yields a value of 0.0019 for the 1^3S_1 state, consistent with the value obtained using the wavefunction at the origin displayed in table (5.15).

An average inverse lattice spacing of $a^{-1} = 3.3\,\text{GeV}$ was taken for $\beta = 6.2$ and used to make the energies and splittings of tables (5.4) and (5.12) dimensionful. The spin-independent energies are shown in figure (5.11) alongside those obtained at $\beta = 6.0$, where again the simulation energies have been shifted so that the 1^3S_1 energy matches experiment. The spin-dependent states are shown in figure (5.12) alongside those obtained at $\beta = 6.0$. The errors shown in both figures reflect statistical errors and some systematic fitting errors. Systematic errors such

β	splitting	$a\Delta M$	$a\Delta M_g$	a^{-1}(GeV)
5.7	$\Upsilon' - \Upsilon$	0.41(3)	-0.005	1.35(13)
	$\chi_b - \Upsilon$	0.326(6)	-0.015	1.41(4)
6.0	$\Upsilon' - \Upsilon$	0.241(9)	-0.001	2.34(9)
	$\chi_b - \Upsilon$	0.174(3)	-0.004	2.59(5)
6.2	$\Upsilon' - \Upsilon$	0.175(8)	0.000	3.22(15)
	$\chi_b - \Upsilon$	0.127(5)	-0.002	3.52(14)

Table 5.16: Results for mass spittings $a\Delta M$, gluonic corrections $a\Delta M_g$ and inverse lattice spacings a^{-1} (in GeV) at three β values. (Experimental values for ΔM are 562.9 MeV for $\Upsilon' - \Upsilon$ and 439.8 MeV for $\chi_b - \Upsilon$).

as quenching, finite lattice spacing and higher order relativistic terms, as well as uncertainties in the value of a^{-1}, are not shown.

The spin-independent results reproduce experiment quite well with only the higher radial excitations 3^3S_1 and 2^1P_1 showing any signs of large systematic errors. These errors are quenching errors explained by the following argument. P states are associated with a longer range part of the quark potential than S states and as a result, the typical gluon momentum associated with P states is smaller than that for S states, $q_{\chi_b} < q_\Upsilon$. Obtaining a^{-1} from the $2S - 1S$ splitting is equivalent to tuning the coupling constant at q_Υ, $\alpha_s^{(0)}(q_\Upsilon) = \alpha_s^{(3)}(q_\Upsilon)$. Since the quenched coupling runs faster than the unquenched coupling, and since the perturbative binding energy is given by [7]

$$\frac{\alpha_s^2(q) C_F^2 M_b}{16}, \tag{5.5}$$

the P states will be more tightly bound in the quenched than in the unquenched case. Alternatively, determining a^{-1} from the $1P - 1S$ splitting is equivalent to tuning the coupling at a scale somewhere between q_{χ_b} and q_Υ and so running

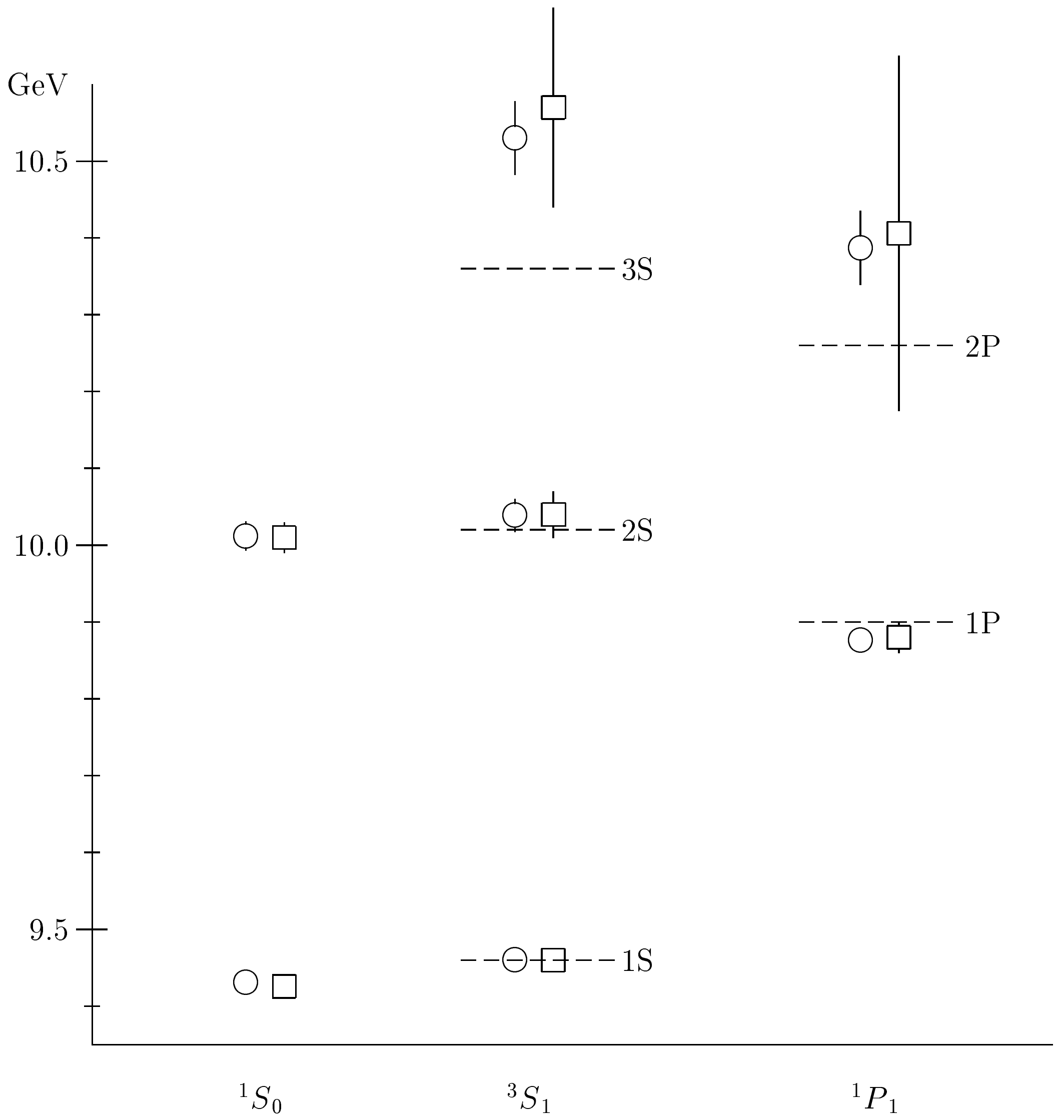

Figure 5.11: Υ **spin-independent spectrum** for $\beta = 6.0$, $n_f = 0$ (open circles) alongside the results of this chapter, $\beta = 6.2$, $n_f = 0$ (boxes). The dashed horizontal lines denote experimental values. The energy zero has been shifted such that the 1^3S_1 states coincide with experiment.

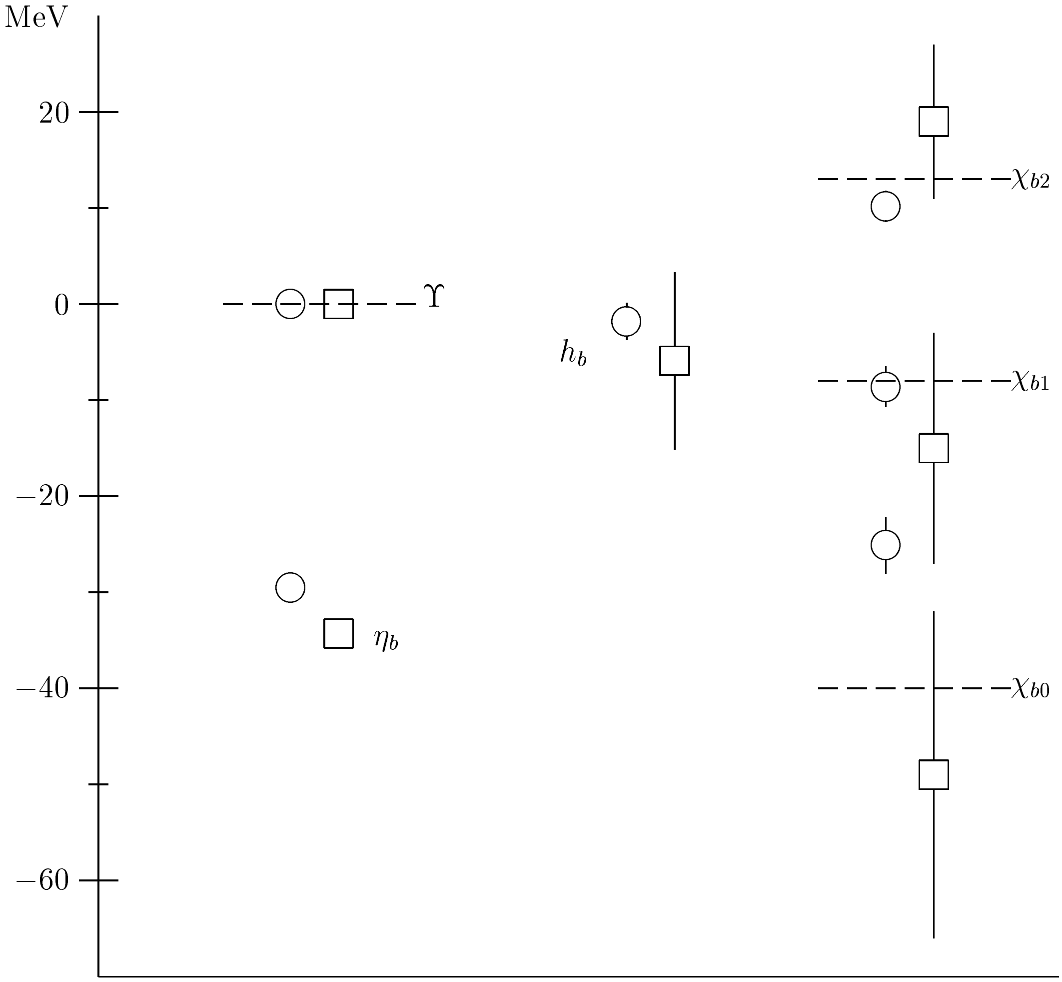

Figure 5.12: Υ **spin-dependent spectrum** for $\beta = 6.0$, $n_f = 0$ (open circles) alongside the results of this chapter, $\beta = 6.2$, $n_f = 0$ (boxes). The dashed horizontal lines denote experimental values. Splittings are shown relative to the Υ or $^3P_{\mathrm{CM}}$ as appropriate.

to q_Υ gives quenched S states that are not as tightly bound as unquenched S states. Taking an average a^{-1} from the two splittings means that both effects will occur as can be clearly seen in figures (3.6) and (5.11) where the 2^3S_1 states are overestimated compared to experiment while the 1^1P_1 states are underestimated compared to experiment. For the dynamical ($n_f = 2$) case, these effects are not as severe as in the quenched case since the $\alpha_s^{(2)}$ coupling runs faster than $\alpha_s^{(3)}$ but slower than $\alpha_s^{(0)}$.

It is unclear whether the spin-dependent states of figure (5.12) are consistent going from one quenched simulation to the other as the errors for the $\beta = 6.2$ case are too large. However using average inverse lattice spacings to scale the spectra introduces an unnecessary uncertainty—a better idea is to choose a^{-1} from one particular splitting. This was undertaken using a^{-1} values from the $2S - 1S$ splitting (since this gave a better tuning of aM_b^0 than the $1P - 1S$ splitting [58]) for the quenched results at $\beta = 6.0$ and 6.2 along with results from a similar quenched simulation at $\beta = 5.7$ [59], the results of which are shown in table (5.17).

Firstly however, the scaling of the spin-independent spectrum was investigated using the results at the three β values.

5.5.1 Radial and orbital splittings

Figure (5.13) shows dimensionless ratios of the $3S-1S$ ($3^3S_1 - 1^3S_1$), the $2P-1S$ ($2^1P_1 - 1^3S_1$) and the $2S - 1S$ ($2^3S_1 - 1^3S_1$) splittings to the $1P - 1S$ ($1^3P_{\mathrm{CM}} - 1^3S_1$) splitting plotted against the lattice spacing. Very flat scaling is apparent in each case indicating that the ratios have been corrected for finite lattice spacing errors and are therefore essentially continuum results. This is desirable as the lattice spacing cannot be extrapolated to zero, since as mentioned at the beginning of chapter 3, this would cause the perturbative expansions of the coupling constants c_i to be divergent thus rendering the theory non-renormalizable. Spin-independent ratios such as these have next to leading order terms included in the

	simulation result
1^1S_0	0.5029(5)
2^1S_0	0.92(3)
1^3S_1	0.5186(6)
2^3S_1	0.94(4)
1^1P_1	0.843(6)
1^3P_{CM}	0.845(6)
$1^3S_1 - 1^1S_0$	0.01575(8)
$1^3P_2 - 1^3P_0$	0.020(2)
$1^3P_2 - 1^3P_1$	0.011(2)
$1^3P_1 - 1^3P_0$	0.0079(5)
wave func. at	
origin for $\Upsilon(1S)$	0.385(5)
for $\Upsilon(2S)$	0.30(2)

Table 5.17: Dimensionless results from quenched simulation at $\beta = 5.7$ [59].

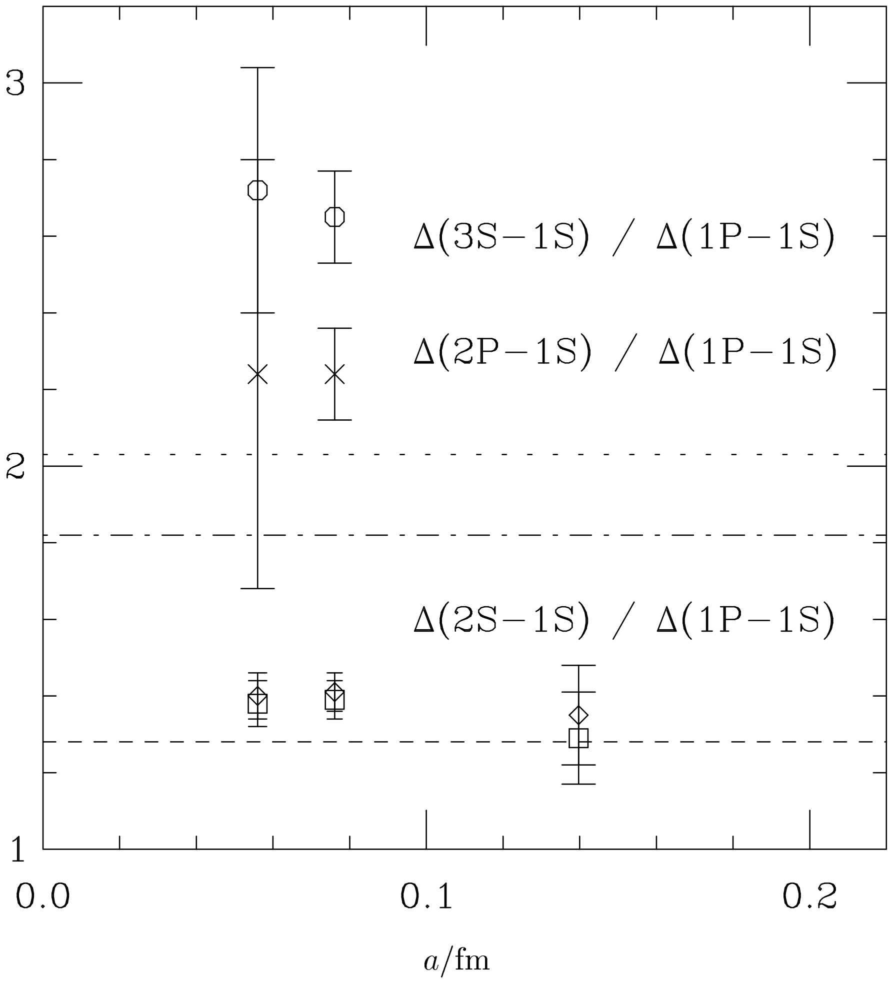

Figure 5.13: Dimensionless ratios of the $3S-1S$, the $2P-1S$ and the $2S-1S$ splittings to the $1P-1S$ splitting against the lattice spacing (determined from the $1P-1S$ splitting). The ratios are denoted by octagons, crosses and diamonds respectively while the experimental values are given by the short dash, dot-dash and dashed lines respectively. Squares denote ratios of the $2S-1S$ splitting to the $1P-1S$ splitting with no $\mathcal{O}(a^2)$ gluonic corrections added.

Lagrangian and so neglected relativistic correction terms are believed to be at the 1% level from the v^2 power counting argument. The fact that the ratios do not agree with experiment is basically a failure of the quenched approximation and is addressed in chapter 6.

Figure (5.14), obtained from [58], shows ratios of the $1P - 1S$ splitting to both the QCD Λ parameter in the V scheme [39] and the ρ mass, as calculated by the UKQCD collaboration at the same three β values [60]. Again essentially flat scaling can be seen for both sets of ratios. The ρ mass used for the octagonal points was calculated with an action having $\mathcal{O}(a)$ lattice spacing errors removed, while that used for the square points was obtained from an earlier determination [61] with no finite lattice spacing corrections. It is interesting to note that ratios with this unimproved ρ mass do not have flat scaling and show incorrect agreement with experiment on coarse lattices.

The discrepancy with experiment of the $1P - 1S\ /m_\rho$ ratio is primarily caused by quenching, not helped by the fact that the scales involved in the light hadron system are very different from those of the Υ system.

5.5.2 Spin splittings and the wavefunction at the origin

Figure (5.15) shows the physical hyperfine ($1^3S_1 - 1^1S_0$) splitting plotted against the square of the lattice spacing. The lattice spacing used here was determined from the $2S - 1S$ splitting as this gave the best agreement with experiment when tuning the bare quark mass [58]. The reason for plotting against the square of the lattice spacing in this section is that lattice spacing errors resulting from the spin terms in the Lagrangian are $\mathcal{O}(a^2)$ relative to these spin terms and so it is plausible that linear relationships will be obtained.

Looking at the square points, a clear dependence on the lattice spacing can be seen. This is probably due to the fact that only lowest order spin terms were included in the Lagrangian and no attempt to correct these terms for finite

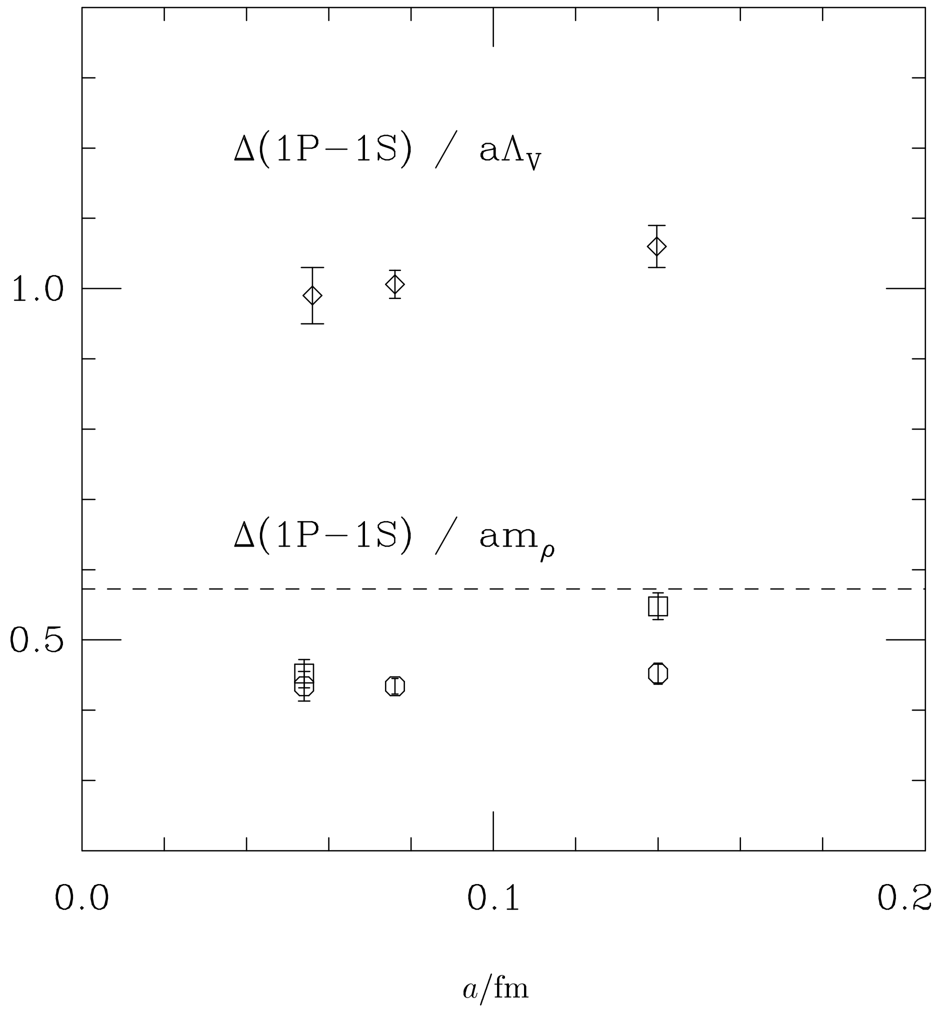

Figure 5.14: Dimensionless ratios of the $1P - 1S$ splitting to the Λ_V parameter (diamonds) and to the UKQCD ρ mass (octagons) against the lattice spacing (determined from the $1P - 1S$ splitting). Ratios using the GF11 ρ mass are denoted by squares. The experimental value for $1P - 1S\ /m_\rho$ is given by the dashed line.

lattice spacing errors was made. The diamond point, however, was obtained at $\beta = 6.0$ from a simulation which included the next to leading order spin terms (terms of order Mv^6) and comparable lattice spacing correction terms [37]. A slight reduction can be seen for the hyperfine splitting for the diamond point when compared with the square point. Since discretization errors are larger at larger lattice spacings, lattice spacing corrections have the effect of increasing the hyperfine splitting and so the next to leading order spin terms presumably have the effect of reducing the hyperfine splitting. Unfortunately more work will have to be done at other β values having the spin improvement terms of [37] before the scaling of the hyperfine splitting can be expected to be flat.

As discussed in section 2.6.4, the tadpole improvement program gives far more convergent perturbative expansions for the coupling constants c_i, allowing the tree-level values of 1 to be used. However radiative corrections to the leading order spin terms are still expected to be of the order of 10%, comparable with the next to leading order spin terms. Different quantities used to define u_0 will have different perturbative expansions and will therefore give different radiative corrections to the couplings c_i. The work of [62] shows that for the charmonium spectrum, the radiative corrections seem to be smaller if u_0 is taken as the mean link in Landau gauge, u_{0L}, rather than the fourth root of the plaquette, u_{0P}. Shown in figure (5.15) by the fancy squares and diamonds are values for the hyperfine splitting rescaled by the sixth power of the ratio of u_{0L} to u_{0P} [63]. These rescaled values show a reduced lattice spacing dependence that is almost linear as was found for the charmonium spectrum by [62].

Figure (5.16) shows physical splittings of the ^3P states to their spin-average, $^3P_{\mathrm{CM}}$, plotted against the square of the lattice spacing. Again the lattice spacing determined from the $2S - 1S$ splitting was used to set the scale.

Looking at the square points, the $^3P_2 - {}^3P_{\mathrm{CM}}$ and $^3P_1 - {}^3P_{\mathrm{CM}}$ splittings show small lattice spacing dependence while that for the $^3P_0 - {}^3P_{\mathrm{CM}}$ splitting is stronger. Again this is likely to be due to having only lowest order spin terms in

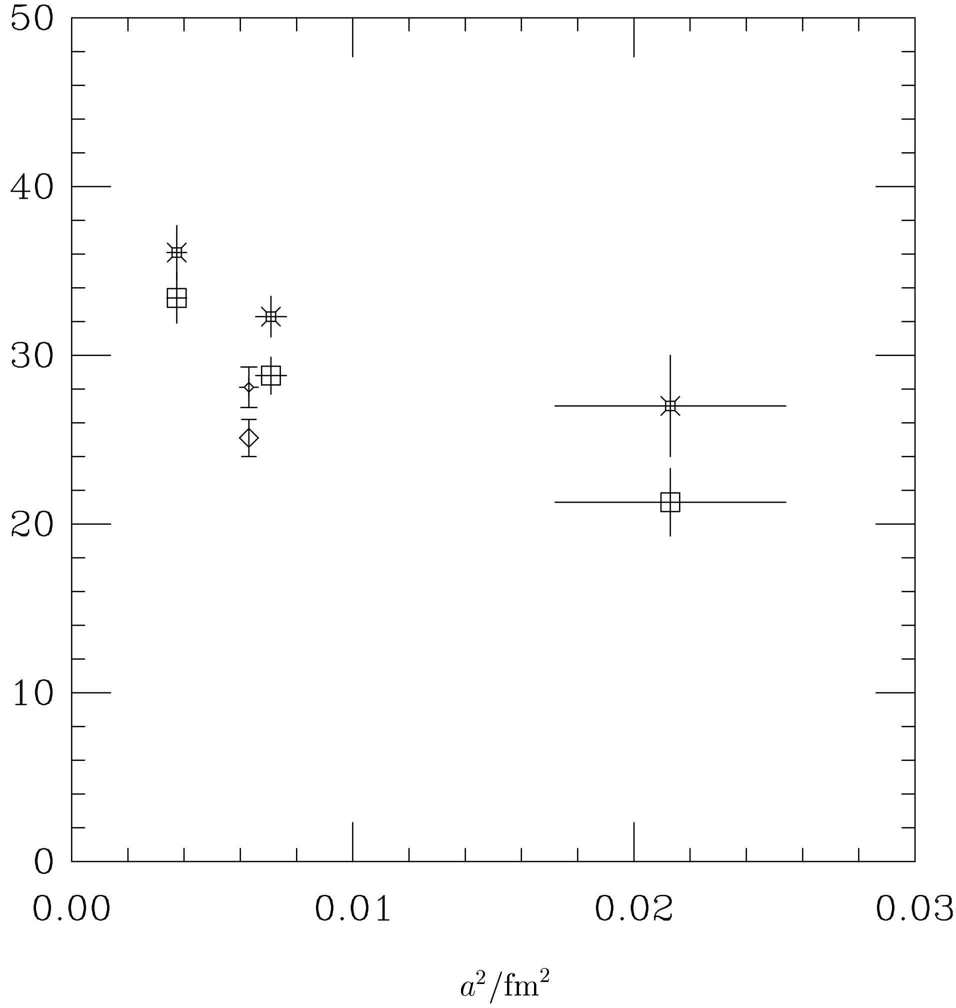

Figure 5.15: Physical hyperfine splitting in MeV using the $2S - 1S$ splitting to set the scale, against the lattice spacing squared. Ordinary squares and the diamond represent values obtained using u_{0P}, the diamond result having been generated with a higher order action [37]. Fancy points are results rescaled by the sixth power of the ratio of u_{0L} to u_{0P}. The diamond points are offset slightly for clarity. The errors shown are statistical only.

the Lagrangian with no finite lattice spacing corrections to these spin terms. For each of the three splittings it would appear that discretization errors have the effect of reducing the splittings and so again, as was found for the hyperfine splitting, lattice spacing correction terms have the effect of increasing the splittings while the next to leading order spin correction terms (included along with comparable lattice spacing corrections for the $\beta = 6.0$ results represented by the diamond points [37]) have the effect of reducing the splittings.

Figure (5.16) also shows the splitting results rescaled by the fourth power of the ratio of u_{0L} to u_{0P} [63] in an attempt to investigate the effects of radiative corrections to the couplings c_i. These rescaled points are denoted by the fancy squares and diamonds and in each case the splitting is larger than that of the corresponding unrescaled one, suggesting that using u_{0L} instead of u_{0P} has the effect of slightly reducing apparent lattice spacing errors.

A short distance quantity that has contributions from both the spin-independent and spin-dependent terms is the wavefunction at the origin, shown in figure (5.17) for the 1^3S_1 and 2^3S_1 states. Since this quantity is sensitive to quark mass, the lattice spacing determined from the $2S - 1S$ splitting, which gave the best mass tuning, was used to set the scale.

The results for both states certainly show some lattice spacing dependence, however large statistical errors arising from the a^{-1} values make it difficult to conclude anything. Naive experimental values, denoted by the bursts, are shown obtained from the Van Royen–Weisskopf formula [64] and from experimental values of the partial leptonic widths [3]. However comparison with these experimental values should probably only be undertaken when higher order ($1/M_b$ and α/M_b) corrections to the electromagnetic current are included.

For scaling of spin splittings and the wavefunction at the origin, and for the purposes of extrapolation in n_f (see chapter 6), it may be wrong to set the scale using the $2S - 1S$ splitting. This is because the typical momentum scale associated with the radial and orbital splittings, $0.5 \sim 1$ GeV, means that the appropriate

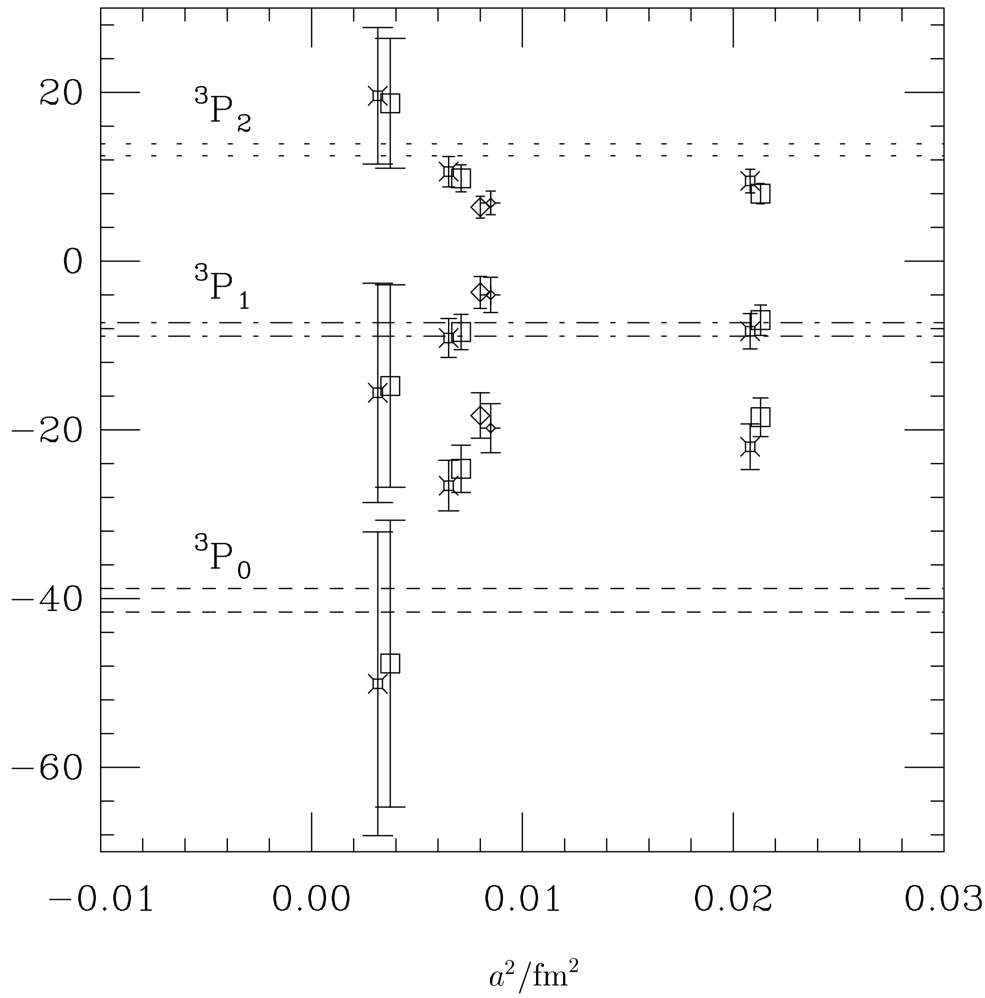

Figure 5.16: Physical splittings in MeV between various ${}^3P$ states and the ${}^3P_{\rm CM}$using the $2S-1S$ splitting to set the scale, against the lattice spacing squared. Ordinary squares and diamonds represent values obtained using u_{0P}, the diamond results having been generated with a higher order action [37]. Fancy points are results rescaled by the fourth power of the ratio of u_{0L} to u_{0P}. The experimental value ranges are given by the broken lines. The diamond points are offset slightly for clarity. The errors shown are statistical only.

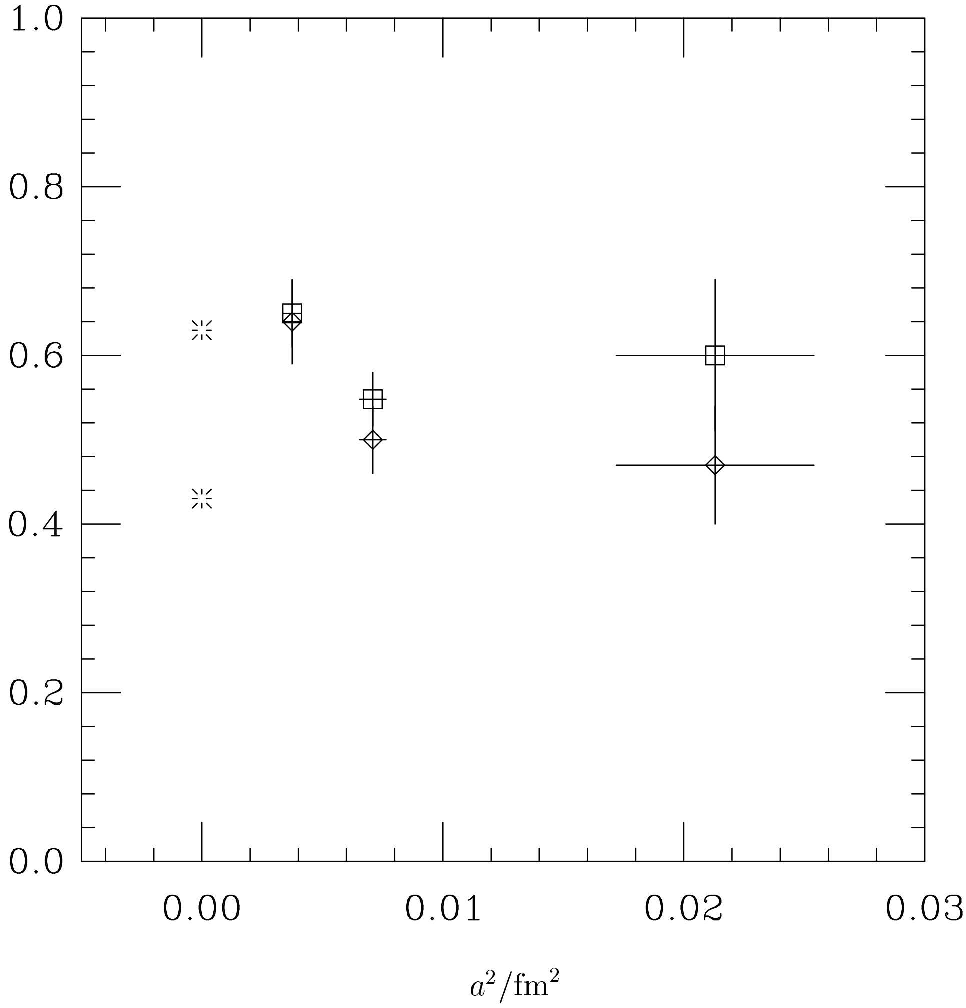

Figure 5.17: Physical wavefunctions at the origin in GeV$^{3/2}$ using the $2S-1S$ splitting to set the scale, against the lattice spacing squared. Squares represent values for the 1^3S_1 state and diamonds for the 2^3S_1 state. The bursts represent experimental values derived from the leptonic widths of the 1^3S_1 (0.63) and 2^3S_1 (0.43) using the Van Royen–Weisskopf formula. The errors shown are statistical only.

number of flavours of vacuum polarization quarks, n_f, is 3 for these splittings. Whereas, the typical momentum scales associated with the spin splittings and wavefunction at the origin are higher and so the appropriate n_f value for these quantities may be 4.

Figure (5.18) shows the ratio of the hyperfine splitting to the $1^3P_2 - 1^3P_0$ splitting against the square of the lattice spacing. It is encouraging to see reduced lattice spacing dependence when compared with figures (5.15) and (5.16), presumably because some cancellation has taken place between the lattice spacing errors of the two splittings.

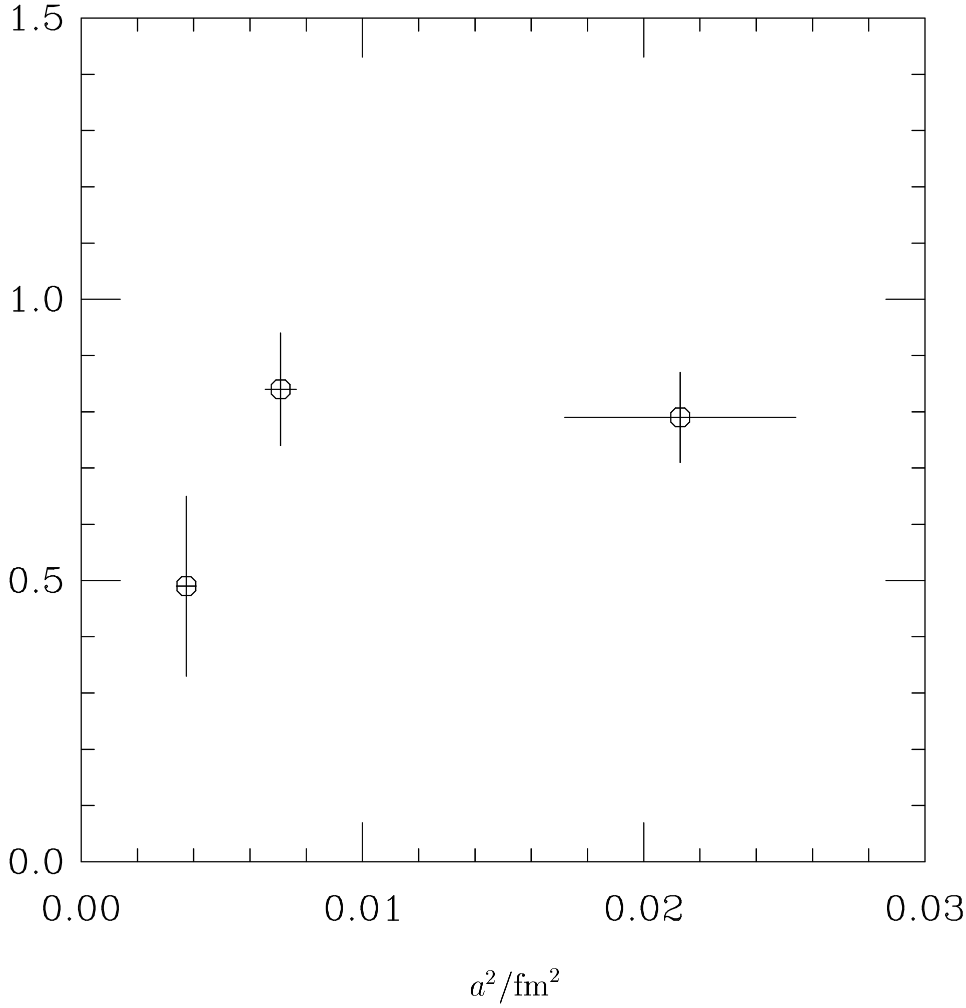

Figure 5.18: Dimensionless ratio of the hyperfine splitting to the $1^3P_2 - 1^3P_0$ splitting against the lattice spacing squared (determined from the $2S - 1S$ splitting). The errors shown are statistical only.

Chapter 6

Upsilon Spectrum n_f Dependency

In section 5.5 the scaling properties of the spin-independent radial and orbital splittings and the spin-dependent splittings as well as the wavefunction at the origin were investigated. It was found that although the radial and orbital splittings showed a discrepancy with experiment, believed to be a systematic quenching error, they gave flat scaling, thereby allowing the quenched ($n_f = 0$) values at $\beta = 6.0$ (those with the smallest errors) to be combined with the dynamical ($n_f = 2$) results at $\beta = 5.6$ (given in table (3.16)) in an attempt to alleviate the quenching error.

The spin splittings and the wavefunction at the origin, on the other hand, exhibited more obvious lattice spacing dependencies presumably because only leading order relativistic spin terms were included in the simulations and no attempt was made to correct for lattice spacing errors arising from these leading order spin terms. Figure (5.18) shows, however, that the lattice spacing dependence seems to be reduced when the ratio of two quantities having similar momentum scales is plotted and so in section 6.2, this principle was adhered to allowing an exploratory investigation of the n_f dependencies of these quantities using the quenched $\beta = 6.0$ and the dynamical $\beta = 5.6$ results (both of which are given in table (3.16)).

6.1 Radial and Orbital Splittings

The typical momentum scale p_Υ associated with the radial and orbital Υ splittings is $0.5 \sim 1$ GeV and so for the masses of the first four quarks;

$$m_u, m_d, m_s \ll p_\Upsilon < m_c. \tag{6.1}$$

This implies that to obtain realistic predictions, extrapolation of such splittings to three flavours of vacuum polarization quarks, $n_f = 3$, must be undertaken. Before doing this, the dynamical configuration results should be extrapolated in the light quark mass to the value $am_s^0/3$, as mentioned in section 1.8. From the discussions of [7] however, the $am_q^0 = 0.01$ results of table (3.16) should give correctly extrapolated values to within 4%, i.e. to within existing statistical errors and so these dynamical configuration results were considered adequate for the n_f extrapolations.

Although the NRQCD systematic improvement program accounts for $\mathcal{O}(a^2)$ lattice spacing errors in the quark action, $\mathcal{O}(a^2)$ errors still exist in the gluonic action. As discussed in sections 4.2 and 5.5, these errors can be corrected for by adding to the dimensionless masses a mass shift, $a\Delta M_g$, given by either (4.1) or (5.4). Table (6.1) shows values for these gluoinc mass shifts for the $^3S_1$ state at $\beta = 5.6$ and 6.0, calculated using (4.1). Using (5.4) along with the hyperfine $1^3S_1 - 1^1S_0$ splittings of table (3.16) gives values for the ground states consistent with those from (4.1).

Figure (6.1) shows the dimensionless ratio of the $2S - 1S$ ($2^3S_1 - 1^3S_1$) splitting to the $1P - 1S$ ($1^3P_{\rm CM} - 1^3S_1$) splitting plotted against n_f. The square points have not been corrected for gluonic mass shifts whereas the diamond points have been and lie about a quarter sigma above the square points. When linearly extrapolated to $n_f = 3$ the diamond points give a value for this ratio 1.28(9), which is in excellent agreement with the experimental value of 1.280 [3]. Although the errors involved are considerably larger than the difference between the improved

β	n_f	state	$a\Delta M_g$
6.0	0	1^3S_1	0.0037
		2^3S_1	0.0031
5.6	2	1^3S_1	0.0051
		2^3S_1	0.0031

Table 6.1: Results of calculations of $\mathcal{O}(a^2)$ gluonic corrections $a\Delta M_g$ to both quenched and dynamical simulation masses.

and unimproved points, it is encouraging to see the agreement with experiment on extrapolation improved when $\mathcal{O}(a^2)$ gluonic corrections are made.

Figure (6.2) shows dimensionless ratios of the $3S-1S$ ($3^3S_1 - 1^3S_1$) and $2P-1S$ ($2^1P_1 - 1^3S_1$) splittings to the $1P-1S$ ($1^3P_{\rm CM} - 1^3S_1$) splitting plotted against n_f. Gluonic mass shifts have been included, with those for the 3^3S_1 state assumed to be equal to those for the 2^3S_1 state since wavefunctions at the origin for the 3^3S_1 state were not extractable. The experimental value in the $2P-1S$ case is that for the ratio $2^3P_{\rm CM} - 1^3S_1 / 1^3P_{\rm CM} - 1^3S_1$ since the 2^1P_1 state has not been seen experimentally.

When linearly extrapolated to $n_f = 3$ the octagon points give a value for the $3S-1S\ /1P-1S$ ratio of 1.84(26) and for the $2P-1S\ /1P-1S$ ratio, the crosses give a value of 1.55(26). Both these values are in agreement with the experimental values of 2.035 and 1.818 [3], respectively, however the fact that they are between a half to one sigma lower might indicate that linear extrapolation is not adequate for ratios involving the 3^3S_1 and 2^1P_1 states. This can be appreciated by observing the quenched and dynamical predictions for these states in figure (3.6), where it can be seen that quenching results in large discrepancies with experiment.

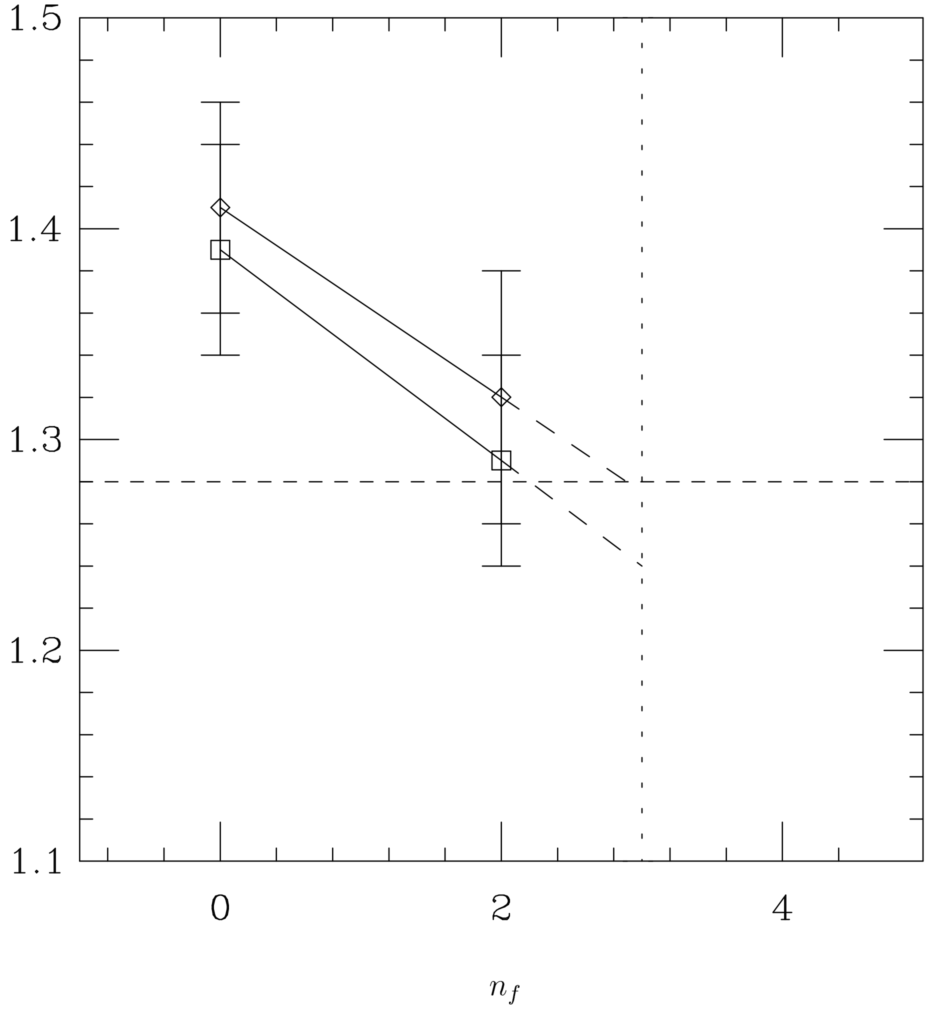

Figure 6.1: Dimensionless ratio of the $2S - 1S$ splitting to the $1P - 1S$ splitting against the number of flavours of vacuum polarization quarks. Diamonds denote values with $\mathcal{O}(a^2)$ gluonic corrections added while squares denote values without these corrections. The horizontal dashed line indicates the experimental value of 1.280.

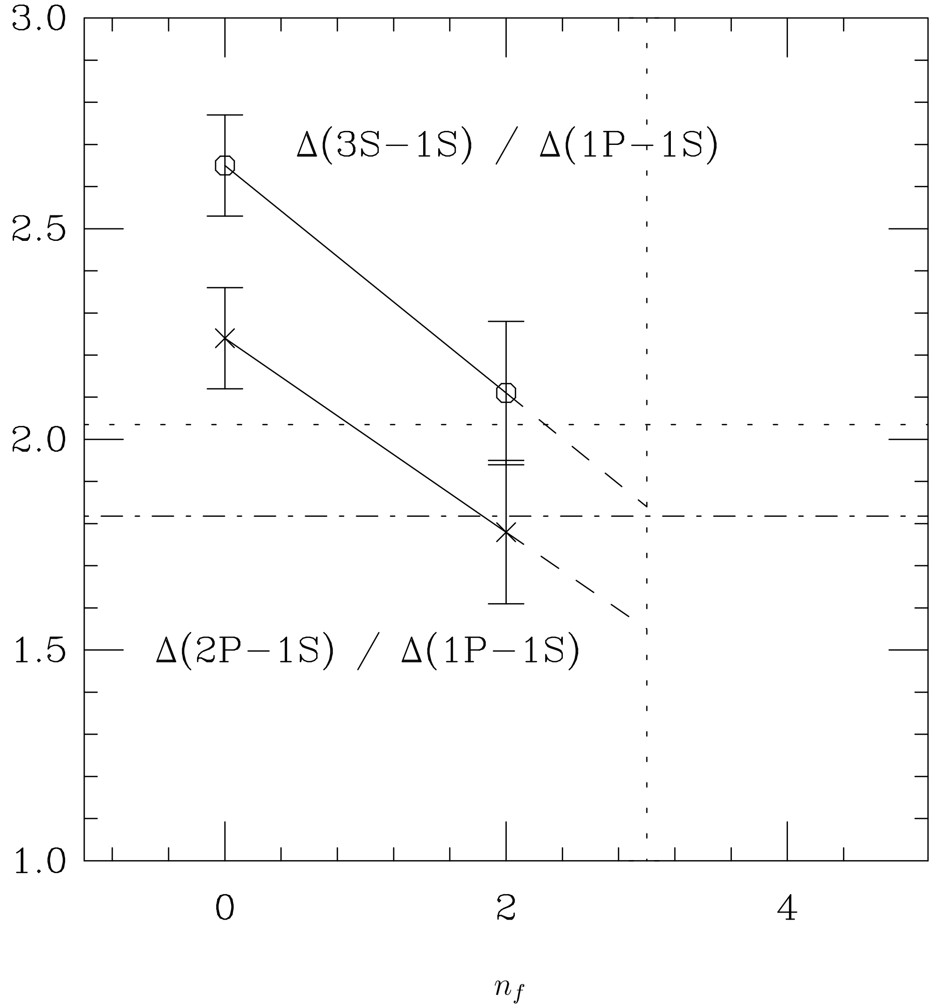

Figure 6.2: Dimensionless ratios of the $3S - 1S$ and the $2P - 1S$ splittings to the $1P - 1S$ splitting against the number of flavours of vacuum polarization quarks. The ratios are denoted by octagons and crosses respectively while the experimental values are given by the horizontal short dash (2.035) and dot-dash (1.818) lines respectively.

6.2 Spin Splittings and the Wavefunction at the Origin

The typical momentum scale p_{fs} associated with the spin-orbit potential term (2.10), which is responsible for the P fine structure splittings, is $\sim \pi/a$ [15]. For $\beta = 5.6, 6.0$ this is approximately 7.5 GeV and so for the masses of the first five quarks;

$$m_u, m_d, m_s, m_c \ll p_{\text{fs}} < 2m_b. \tag{6.2}$$

This implies that to obtain realistic estimates of these P spin splittings, and presumably also the S hyperfine splitting and wavefunctions at the origin, extrapolation to four flavours of vacuum polarization quarks, $n_f = 4$, should be undertaken.

Figure (6.3) shows physical splittings of the ^3P states to their spin-average, $^3P_{\text{CM}}$, plotted against n_f. Rather than use the $1P - 1S$ or $2S - 1S$ splittings to set the scale, the $^3P_2 - {}^3P_0$ splitting was used instead[1], for the ordinary squares, diamonds and crosses, having a similar typical momentum scale. All three sets of points give extrapolated values which are in good agreement with experiment. The extrapolated values are; for the $^3P_2 - {}^3P_{\text{CM}}$ splitting 11(7) MeV, for the $^3P_1 - {}^3P_{\text{CM}}$ splitting $-5(7)$ MeV and for the $^3P_0 - {}^3P_{\text{CM}}$ splitting $-40(13)$ MeV. These compare with the experimental values of 13.0(7) MeV, $-8.3(8)$ MeV and $-40.4(14)$ MeV respectively.

The fact that the agreement with experiment is quite good is probably caused in part by a cancellation of the lattice spacing errors from both the splittings and the a^{-1} values. It is also almost certainly true that using the $^3P_2 - {}^3P_0$ splitting to set the scale allows cancellation of errors arising from the absence of

[1]Setting the scale using the $^3P_2 - {}^3P_0$ splitting means using a^{-1} values obtained from dividing the experimental value for this splitting by the dimensionless values obtained from the $\beta = 5.6, 6.0$ simulations

the next to leading order relativistic spin terms. With this in mind, the P fine structure splittings were also plotted against n_f, this time scaled by values of a^{-1} extracted from the 1^3S_1 wavefunction at the origin, with experimental values for this wavefunction at the origin obtained using the Van Royen–Weisskopf formula [64] along with experimental values of the partial leptonic widths [3].

The splittings scaled by the wavefunction at the origin are denoted in figure (6.3) by the fancy squares, diamonds and crosses. The errors on these splittings do not take into account the omission of higher order ($1/M_b$ and α/M_b) corrections to the electromagnetic current. Again extrapolation to $n_f = 4$ gives values for the splittings (11(4) MeV for ${}^3P_2 - {}^3P_{\rm CM}$, $-7(4)$ MeV for ${}^3P_1 - {}^3P_{\rm CM}$ and $-37(10)$ MeV for ${}^3P_0 - {}^3P_{\rm CM}$) that are in good agreement with experiment. It is interesting to see that the large discrepancy between the quenched ${}^3P_0 - {}^3P_{\rm CM}$ splitting and experiment disappears on extrapolation to $n_f = 4$, indicating that perhaps the discrepancies with experiment shown in figure (5.16) may be caused in large part by quenching rather than lattice spacing errors and omission of next to leading order relativistic spin terms.

This last statement is vindicated by the dimensionless ratio of the ${}^3P_2 - {}^3P_1$ splitting to the ${}^3P_1 - {}^3P_0$ splitting, known as the Peskin ratio [16], plotted against n_f in figure (6.4). Here the large discrepancy with experiment at $n_f = 0$ is alleviated on unquenching; the extrapolated value at $n_f = 4$ is 0.4(3) which is in agreement with the experimental value of 0.66(4) [3]. It is interesting also to observe that a value of -30 MeV instead of the present -24.6 MeV for the ${}^3P_0 - {}^3P_{\rm CM}$ splitting at $\beta = 6.0$ of figure (5.16) (a relatively small change still leaving a large systematic discrepancy with experiment) gives a Peskin ratio of 0.85 at $n_f = 0$ and therefore an extrapolated central value of 0.63 at $n_f = 4$ which is in excellent agreement with experiment.

Figures (6.3) and (6.4) indicate that extrapolation to $n_f = 4$ gives reasonable agreement with experiment for the P fine structure splittings. This fact was made use of to obtain a prediction for the S hyperfine ($1^3S_1 - 1^1S_0$) splitting,

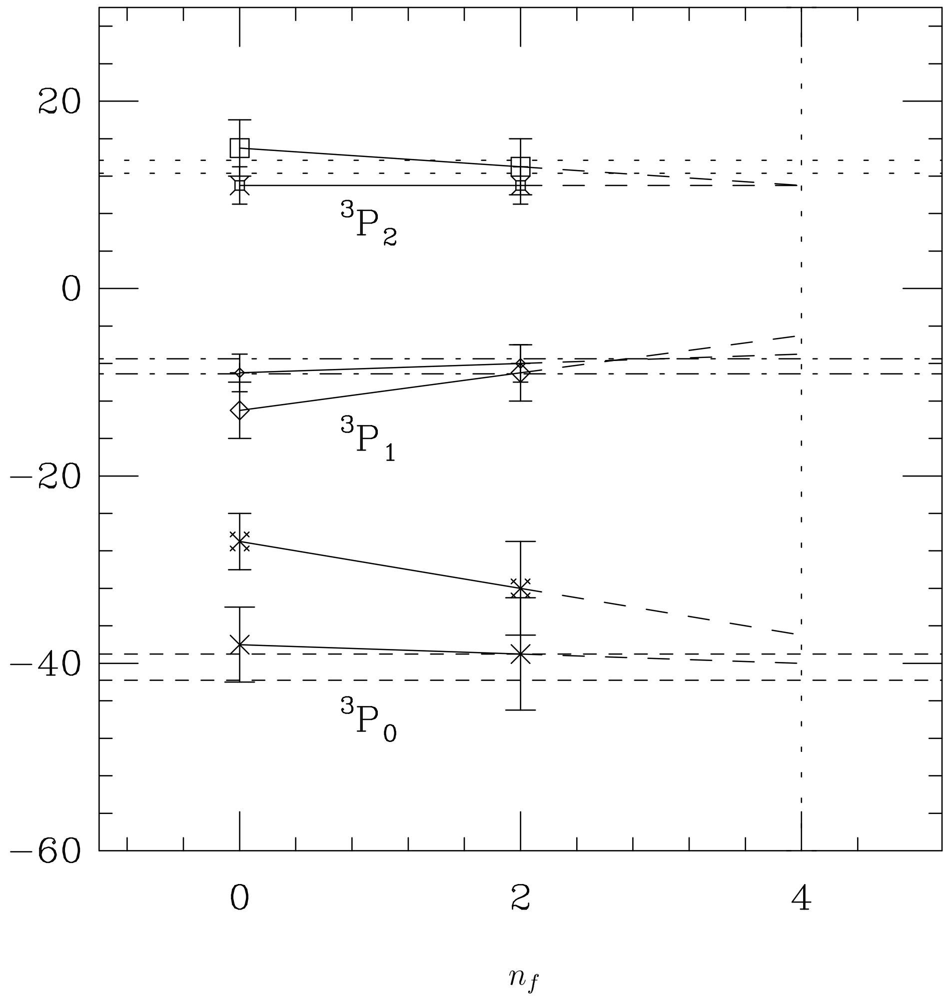

Figure 6.3: Physical splittings in MeV between various ^3P states and the $^3P_{\mathrm{CM}}$against the number of vacuum polarization quarks. Ordinary points represent values scaled by the $^3P_2 - {}^3P_0$ splitting while fancy points represent values scaled by the 1^3S_1 wavefunction at the origin. The experimental value ranges are given by the horizontal broken lines. The errors shown are statistical only.

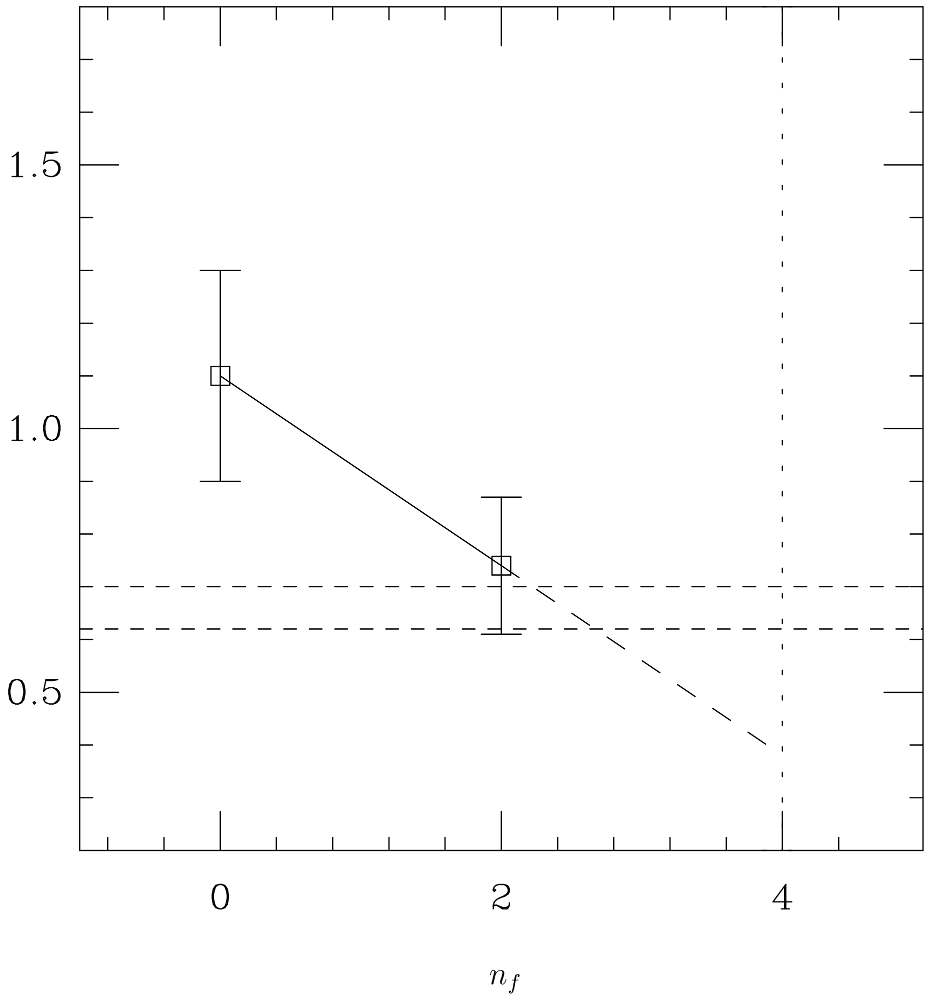

Figure 6.4: Dimensionless ratio of the ${}^3P_2 - {}^3P_1$ splitting to the ${}^3P_1 - {}^3P_0$ splitting (Peskin ratio) against the number of flavours of vacuum polarization quarks. The horizontal dashed lines indicate the experimental value range of 0.66(4). The errors shown are statistical only.

which has not been seen experimentally. Figure (6.5) shows the dimensionless ratio of the S hyperfine splitting to the $^3P_2 - {}^3P_0$ splitting plotted against n_f. Extrapolation to $n_f = 4$ gives a value for this ratio of 0.8(2) and so multiplication by the experimental $^3P_2 - {}^3P_0$ splitting value (53.4(14) MeV) gives an S hyperfine splitting prediction of 43(11) MeV. The error quoted here is a statistical one and does not take into account systematic errors arising from the omission of next to leading order spin terms in the Lagrangian and the omission of comparable lattice spacing correction terms. However it is quite possible that the ratio of the two spin splittings gives rise to a certain amount of cancellation of these systematic errors and so it may be that the statistical error dominates.

In figure (6.3) the scaling of the P fine structure splittings using the wavefunction at the origin $\psi(0)$ gave reasonably good results, making $\psi(0)$ a good candidate for predicting the S hyperfine splitting. To test this further, figure (6.6) shows the dimensionless ratio of the cube of the $^3P_2 - {}^3P_0$ splitting to the square of the wavefunction at the origin plotted against n_f. The squares use $\psi(0)$ for the 1^3S_1 state while the diamonds use $\psi(0)$ for the 2^3S_1 state. Extrapolation to $n_f = 4$ gives values for the ratio which, when multiplied by experimental $\psi(0)$ values, yield for the $^3P_2 - {}^3P_0$ splitting the values 48(9) MeV and 46(9) MeV respectively. Both of which agree with the experimental value of 53.4(14) MeV, but are $1/2 \sim 1\sigma$ lower. It is interesting to note that if the values 48(9) MeV and 46(9) MeV for the $^3P_2 - {}^3P_0$ splitting are slightly low because of the absence of higher order electromagnetic current terms in the Lagrangian, then inclusion of these terms would give larger a^{-1} values from the wavefunction at the origin and so the agreement with experiment in figure (6.3) of the P splittings scaled by these a^{-1} values would be improved in all three cases.

Figure (6.7) shows similarly the dimensionless ratio of the cube of the S hyperfine splitting to the square of the wavefunction at the origin plotted against n_f. Again the squares use $\psi(0)$ for the 1^3S_1 state while the diamonds use $\psi(0)$ for the 2^3S_1 state. Extrapolation to $n_f = 4$ and subsequent multiplication by

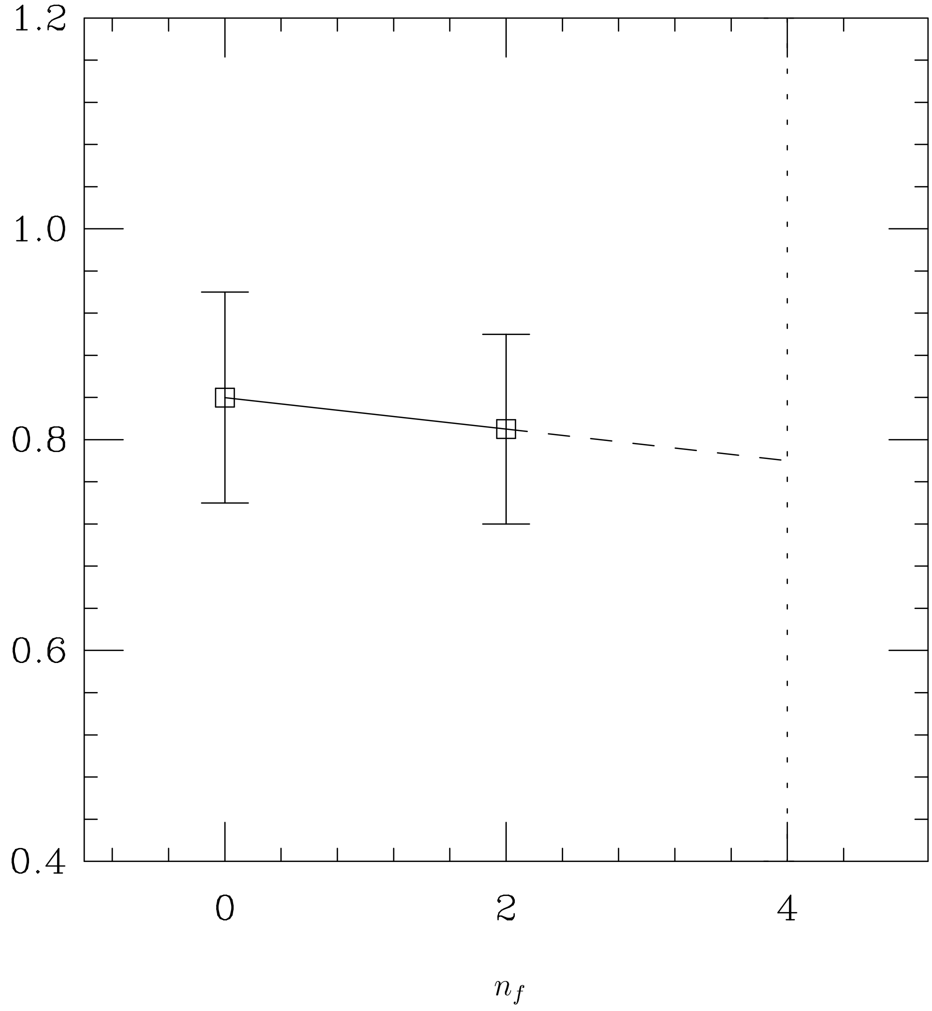

Figure 6.5: Dimensionless ratio of the S hyperfine splitting to the ${}^3P_2 - {}^3P_0$ splitting against the number of flavours of vacuum polarization quarks. The errors shown are statistical only.

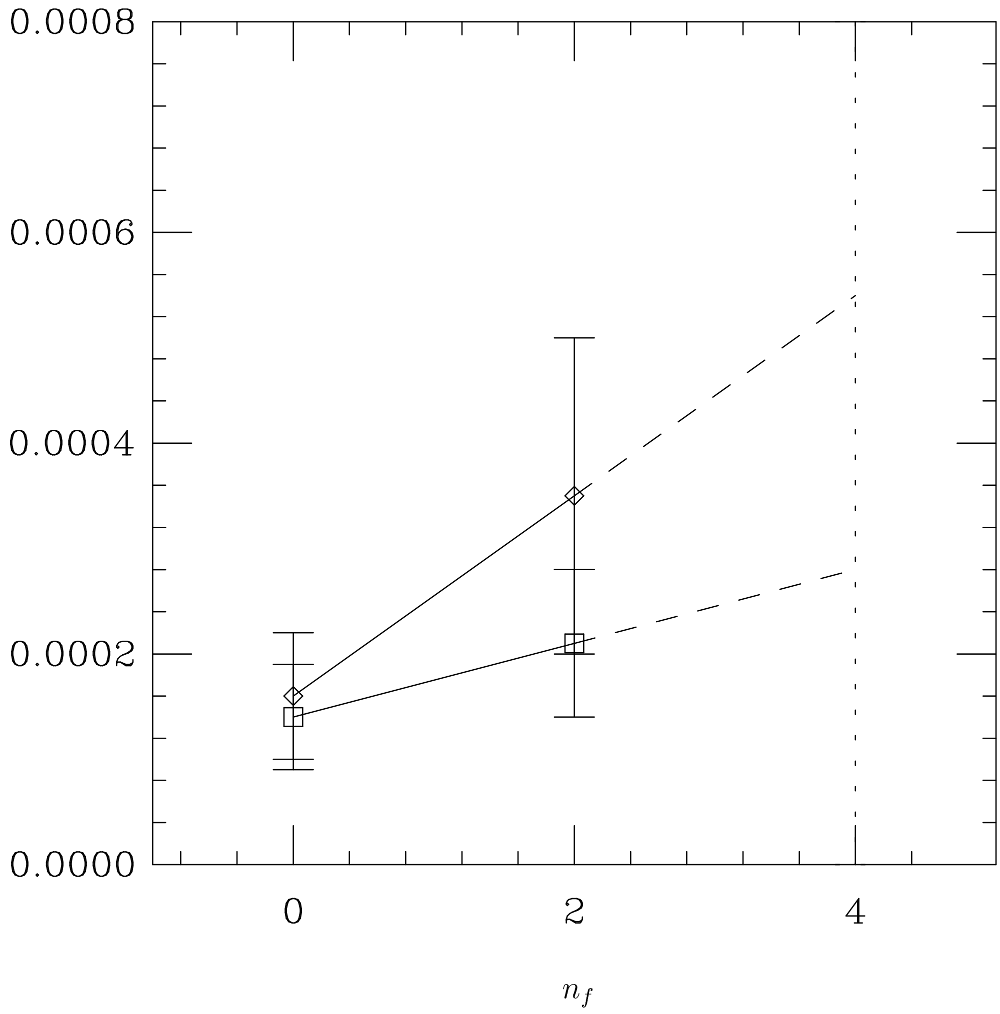

Figure 6.6: Dimensionless ratio of the cube of the $^3P_2 - {}^3P_0$ splitting to both the square of the 1^3S_1 wavefunction at the origin (squares) and the square of the 2^3S_1 wavefunction at the origin (diamonds), against the number of flavours of vacuum polarization quarks. The errors shown are statistical only.

the experimental $\psi(0)$ values yields predictions for the S hyperfine splitting of 38.9(4) MeV and 37(4) MeV respectively. Making the assumption that these values are $1/2 \sim 1\sigma$ lower (as was the case for the ${}^3P_2 - {}^3P_0$ splitting), a common value of 41(4) MeV is arrived at.

The value 41(4) MeV for the S hyperfine splitting agrees really well with the determination from figure (6.5) of 43(11) MeV. In both cases the errors reflect only statistical errors, however judging by the agreement obtained with experiment where possible in this section, systematic quenching errors seem to have been alleviated leaving only systematic errors such as omission of next to leading order spin terms and omission of lattice spacing corrections to the leading order spin terms. From the velocity expansion power counting arguments, a naive estimate of 10% can be made for the magnitude of these systematic errors. This implies then a predicted value for the S hyperfine splitting of 41(4)(4) MeV $\equiv$ 41(6) MeV.

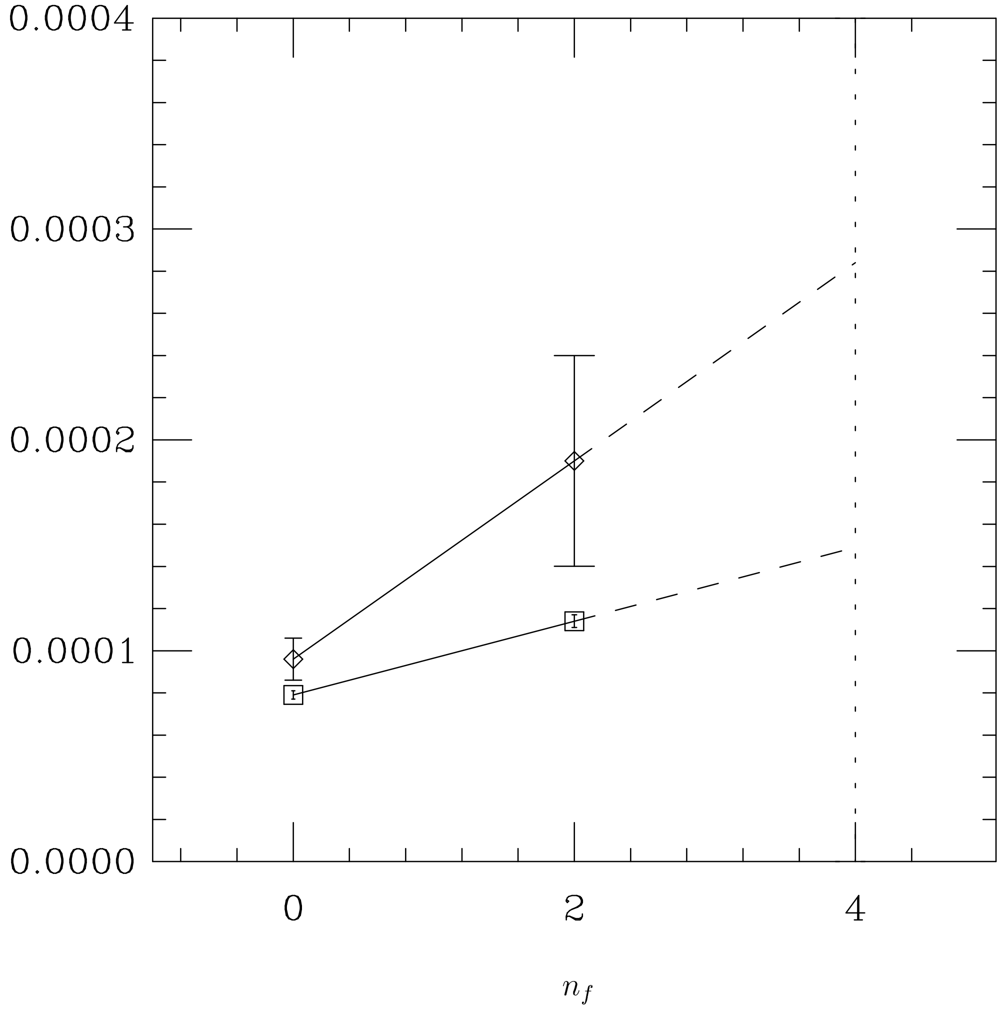

Figure 6.7: Dimensionless ratio of the cube of the S hyperfine splitting to both the square of the 1^3S_1 wavefunction at the origin (squares) and the square of the 2^3S_1 wavefunction at the origin (diamonds), against the number of flavours of vacuum polarization quarks. The errors shown are statistical only.

Chapter 7

Conclusions

The method of non-relativistic QCD has been shown to be an excellent method for the simulation and analysis of the upsilon spectrum. The power counting method proves to be valuable when assessing the contribution to the overall energy made by a particular term in the expansion. The accuracy of this NRQCD method can be systematically increased by including more expansion terms as required and the scope for doing so is only limited in theory by higher order four-Fermi interaction terms. This contrasts with potential models where the price for increasing accuracy is the inclusion of many more free parameters and where in principle there is a limit on the accuracy of spin terms.

The quenched simulations at $\beta = 6.0, 6.2$ of chapters 3 and 5 provided good, accurate determinations of the upsilon spectrum. Here all terms whose magnitude was of order Mv^4 or larger were included, thus leading and next to leading order spin-independent terms and leading order spin-dependent terms were included as were leading order lattice spacing corrections to the leading order spin-independent terms, which were found to be comparable with the order Mv^4 terms. The results for a similar quenched simulation at $\beta = 5.7$ and a dynamical simulation at $\beta = 5.6$, carried out by other NRQCD collaboration members, are also included in chapters 3 and 5. Figures (3.6), (3.7), (5.11) and (5.12) show all the results graphically, where it can be observed that statistical errors (the errors shown) are of a similar magnitude to systematic errors such as omission of higher order relativistic terms, finite lattice spacing errors and quenching errors. This last type of systematic error is particularly evident in figures (3.6) and (3.7) where the $\beta = 5.6$ results having two flavours of vacuum polarization quarks give better agreement with experiment than the $\beta = 6.0$ results having no flavours of vacuum polarization quarks.

For the upsilon spin-independent radial and orbital splittings, systematic errors seem to be under control as demonstrated in section 5.5.1 where very flat scaling is in evidence for ratios of these splittings. Unfortunately statistical errors are still too large for the 2^1P_1 and 3^3S_1 states, particularly for the $\beta = 6.2$ simulations. This flat scaling implies that discrepancies with experiment are caused by quenching and so in section 6.1 results for $\beta = 6.0$, $n_f = 0$ and $\beta = 5.6$, $n_f = 2$ were extrapolated to $n_f = 3$. It would be desirable to observe the scaling behaviour of the dynamical radial and orbital splitting spectrum, however NRQCD collaboration results for this spectrum were only available at $\beta = 5.6$ and so work will have to be done at other β values before this is possible.

Excellent agreement with experiment was obtained for the ratio of the $2S - 1S$ splitting to the $1P - 1S$ splitting extrapolated to $n_f = 3$, particularly when leading order lattice spacing corrections to the gluonic action are included. Reasonable agreement with experiment was obtained for ratios of splittings involving the 2^1P_1 and 3^3S_1 states, however it may be that a linear extrapolation to $n_f = 3$ is not appropriate for quantities involving these states.

For the upsilon spin-dependent splittings and the wavefunction at the origin a definite lattice spacing dependence can be seen in the figures of section 5.5.2 due primarily to the absence of lattice spacing corrections to the leading order spin-dependent terms and also to the absence of next to leading order spin-dependent terms. Results from other NRQCD simulations at $\beta = 6.0$ having these extra terms consistently gave a reduction in the splitting values. Using u_{0L} instead of u_{0P} for tadpole improvement consistently gave an increase in the splittings and a reduced lattice spacing dependence and indicates that radiative corrections to the leading order spin terms may be substantial. As future work, it would be desirable to observe the scaling behaviour of spin-dependent quantities from simulations having all spin terms of magnitudes Mv^6, $a^2M^3v^6$ and αMv^4 present, for both the quenched and dynamical cases.

Surprisingly reasonable agreement with experiment was obtained in section 6.2 for the triplet P_J state splittings, where various spin-dependent quantities from the $\beta = 6.0$, $n_f = 0$ and $\beta = 5.6$, $n_f = 2$ simulations were extrapolated to $n_f = 4$. This may well be caused by a partial cancellation of both lattice spacing errors and the absence of higher order spin terms. Three determinations of the S state hyperfine splitting gave results consistent with the value 41(6) MeV and so this was taken as a prediction for the splitting.

The method outlined in chapter 4 for determining the strong coupling constant in the $\overline{\mathrm{MS}}$ scheme at the Z^0 mass is amongst the most accurate in the world, as can be seen from figure (4.2), and gave a best value of 0.1171(23). The error quoted here is largely statistical and comes mainly from the determination of the lattice spacing which is used to scale the coupling. In turn, the error quoted on the lattice spacing is due to the limited number of gauge configurations in the ensembles used, particularly the dynamical ensemble and so as future work it would be interesting to repeat the calculations of chapter 4 with larger ensembles.

Also investigated in chapter 4 were systematic errors contributing to the final value of $\alpha_{\overline{\mathrm{MS}}}(M_Z)$. Most were found to be almost negligible and the only appreciable error came from the uncertainty over which n_f to extrapolate the inverse plaquette coupling to. Although 3 is believed to be the correct value, 4 will only be ruled out when NRQCD simulations are undertaken having four flavours of dynamical quarks.

Bibliography

[1] L. H. Ryder, *Quantum Field Theory*, Cambridge University Press (1991).

[2] F. Mandl and G. Shaw, *Quantum Field Theory*, John Wiley and Sons (1990).

[3] Physical Review D, *Particles and Fields*, Part I, *Review of Particle Physics*, American Institute of Physics (1996).

[4] K. G. Wilson, *Confinement of quarks*, Phys. Rev. D **10**, 2445 (1974).

[5] H. J. Rothe, *Lattice Gauge Theories, An Introduction*, World Scientific (1992).

[6] B. Grinstein and I. Z. Rothstein, *Errors in lattice extractions of α_s due to use of unphysical pion masses*, Phys. Lett. B **385**, 265 (1996).

[7] C. T. H. Davies, K. Hornbostel, G. P. Lepage, P. McCallum, J. Shigemitsu and J. Sloan, *Further Precise Determinations of α_s from Lattice QCD*, hep-lat/9703010

[8] These ensembles of gauge configurations were provided by the HEMCGC collaboration.

[9] W. Lucha, F. F. Schöberl and D. Gromes, *Bound States of Quarks*, Phys. Rep. **200**, 127 (1991).

[10] E. Eichten, K. Gottfried, T. Kinoshita, J. Kogut, K. D. Lane and T. M. Yan, *Spectrum of Charmed Quark-Antiquark Bound States*, Phys. Rev. Lett. **34**, 369 (1975).

[11] E. Eichten, K. Gottfried, T. Kinoshita, K. D. Lane and T. M. Yan, *Charmonium: Comparison with experiment*, Phys. Rev. D **21**, 203 (1980).

[12] J. L. Richardson, *The Heavy Quark Potential and the Υ, J/ψ Systems*, Phys. Lett. B **82**, 272 (1979).

[13] F. Schöberl, *A Non-Perturbative Calculation of Meson and Baryon Masses With a One-Parameter Potential*, Z. Phys. C **15**, 261 (1982).

[14] E. Eichten and F. Feinberg, *Spin-dependent forces in quantum chromodynamics*, Phys. Rev. D **23**, 2724 (1981).

[15] G. S. Bali, K. Schilling and A. Wachter, *Complete $\mathcal{O}(v^2)$ corrections to the static interquark potential from SU(3) gauge theory*, Wuppertal preprint WUB-97-11, hep-lat/9703019.

[16] M. Peskin, *Dynamics and Spectroscopy at High Energy*, Proceedings of the 11th SLAC Summer Institute on Particle Physics, SLAC report 267.

[17] G. P. Lepage and B. A. Thacker, *Effective Lagrangians for Simulating of Heavy Quark Systems*, Nucl. Phys. B (Proc. Suppl.) **4**, 199 (1988).

[18] B. A. Thacker and G. P. Lepage, *Heavy-quark bound states in lattice QCD*, Phys. Rev. D **43**, 196 (1991).

[19] C. T. H. Davies and B. A. Thacker, *Heavy-quark renormalization parameters in nonrelativistic QCD*, Phys. Rev. D **45**, 915 (1992).

[20] G. P. Lepage, L. Magnea, C. Nakhleh, U. Magnea and K. Hornbostel, *Improved Nonrelativistic QCD for Heavy Quark Physics*, Phys. Rev. D **46**, 4052 (1992).

[21] A. S. Kronfeld and P. B. Mackenzie, *Progress in Quantum Chromodynamics with Lattice Gauge theory*, Annu. Rev. Nucl. Part. Sci. **43**, 793 (1993).

[22] G. T. Bodwin, E. Braaten and G. P. Lepage, *Rigorous QCD Analysis of Inclusive Annihilation and Production of Heavy Quarkonium*, Phys. Rev. D **51**, 1125 (1995).

[23] S. M. Catterall, F. R. Devlin, I. T. Drummond, R. R. Horgan and A. D. Simpson, *Non-relativistic QCD for Heavy Quark Systems*, Phys. Lett. B **300**, 393 (1993).

[24] C. T. H. Davies and B. A. Thacker, *Upsilon Spectroscopy from Lattice QCD*, Nucl. Phys. B **405**, 593 (1993).

[25] S. M. Catterall, F. R. Devlin, I. T. Drummond, R. R. Horgan, *Radial excited states for heavy quark systems in NRQCD*, Phys. Lett. B **321**, 246 (1994).

[26] C. T. H. Davies, K. Hornbostel, A. Langnau, G. P. Lepage, A. Lidsey, J. Shigemitsu and J. Sloan, *Precision Υ spectroscopy from nonrelativistic lattice QCD*, Phys. Rev. D **50**, 6963 (1994).

[27] C. T. H. Davies, K. Hornbostel, A. Langnau, G. P. Lepage, A. Lidsey, C. J. Morningstar, J. Shigemitsu and J. Sloan, *New Determination of the Pole Mass of the b Quark Using Lattice QCD*, Phys. Rev. Lett. **73**, 2654 (1994).

[28] C. T. H. Davies, K. Hornbostel, G. P. Lepage,A. J. Lidsey, J. Shigemitsu and J. Sloan, *Precision charmonium spectroscopy from lattice QCD*, Phys. Rev. D **52**, 6519 (1995).

[29] C. T. H. Davies, K. Hornbostel, G. P. Lepage, A. J. Lidsey, J. Shigemitsu and J. Sloan, *B_c Spectroscopy From Lattice QCD*, Phys. Lett. B **382**, 131 (1996).

[30] C. T. H. Davies, *B_c and Υ Spectra from Lattice NRQCD - Results at $\beta = 5.7$*, Nucl. Phys. B (Proc. Suppl.) **47**, 421 (1996).

[31] A. Ali Khan, C. T. H. Davies, S. Collins, J. Sloan and J. Shigemitsu, *Heavy-light spectrum from lattice NRQCD*, Phys. Rev. D **53**, 6433 (1996).

[32] S. Collins, U. M. Heller, J. H. Sloan, J. Shigemitsu, A. Ali Khan and C. T. H. Davies, *B Spectroscopy from NRQCD with Dynamical Fermions*, (unpublished).

[33] A. Ali Khan, *B Physics with NRQCD: A Quenched Study*, Nucl. Phys. B (Proc. Suppl.) **47**, 425 (1996).

[34] J. P. Costella and B. H. J. McKellar, *The Foldy-Wouthuysen Transformation*, Amer. Journ. Phys. **63**, 1119 (1995).

[35] A. Y. Silenko, *Dirac-equation in the Foldy-Wouthuysen Representation Describing the Interaction of Spin-$\frac{1}{2}$ Relativistic-particles with an External Electromagnetic-field*, Theor. & Math. Phys. **105**, 1224 (1995).

[36] G. V. Grigoryan and R. P. Grigoryan, *Pseudoclassical Foldy-Wouthuysen Transformation and Canonical Quantization of $(D = 2N)$-dimensional Relativistic Particle with Spin in an External Electromagnetic-field*, Theor. & Math. Phys. **102**, 275 (1995).

[37] T. Manke, I. T. Drummond, R. R. Horgan and H. P. Shanahan, *Υ-spectrum from NRQCD with Improved Action*, hep-lat/9706003

[38] B. Sheikholeslami and R. Wohlert, *Improved Continuum Limit Lattice Action for QCD with Wilson Fermions*, Nucl. Phys. B **259**, 572 (1985).

[39] G. P. Lepage and P. B. Mackenzie, *On the Viability of Lattice Perturbation Theory*, Phys. Rev. D **48**, 2250 (1993).

[40] C. J. Morningstar, *Radiative-corrections to the kinetic couplings in nonrelativistic lattice QCD* Phys. Rev. D **50**, 5902 (1994).

[41] I. Montvay and G. Münster, *Quantum Fields on a Lattice*, Cambridge University Press (1994).

[42] These values were kindly provided by J. Sloan *et al.*

[43] B. H. Bransden and C. J. Joachain, *Introduction to Quantum Mechanics*, Longman Scientific & Technical (1990).

[44] R. D. Kenway, Proceedings of the XXII International Conference on High Energy Physics, Leipzig, ed. A. Meyer and E. Wieczorek, Akademie der Wissenschaften der DDR (1984) 51.

[45] M. Lüscher and U. Wolff, *How to calculate the elastic scattering matrix in two-dimensional quantum field theories by numerical simulation*, Nuc. Phys. B **339**, 222 (1990).

[46] W. H. Press, B. P. Flannery, S. A. Teukolsky and W. T. Vetterling, *Numerical Recipes*, Cambridge University Press (1986).

[47] This ensemble of gauge configurations was provided by J. Kogut et al.

[48] Results are taken from an n_f extrapolation paper by C. T. H. Davies *et al* in preparation. They can also be seen in P. McCallum and J. Shigemitsu, *Update on Quarkonium Spectroscopy and* α_{strong} *from NRQCD*, Nucl. Phys. B (Proc. Suppl.) **47**, 409 (1996).

[49] C. T. H. Davies, K. Hornbostel, G. P. Lepage, A. Lidsey, J. Shigemitsu and J. Sloan, *A precise determination of* α_s *from lattice QCD*, Phys. Lett. B **345**, 42 (1995).

[50] G. Rodrigo and A. Santamaria, *QCD matching conditions at thresholds*, Phys. Lett. B **313**, 441 (1993).

[51] This coefficient was supplied by Kent Hornbostel, Southern Methodist University, Dallas.

[52] M. Lüscher and P. Weisz, *Two-loop relation between the bare lattice coupling and the* $\overline{\mathrm{MS}}$ *coupling in pure* $SU(N)$ *gauge theories*, Phys. Lett. B **349**, 165 (1995).

[53] J. Fingberg, *Notes on effective coupling schemes*, Private Communication.

[54] F. Di Renzo, E. Onofri and G. Marchesini, *Renormalons from eight loop expansion of the gluon condensate in lattice gauge theory*, Nucl. Phys. B **457**, 202 (1995).

[55] P. McCallum and J. Shigemitsu, *Update on Quarkonium Spectroscopy and* α_{strong} *from NRQCD*, Nucl. Phys. B (Proc. Suppl.) **47**, 409 (1996).

[56] This ensemble of gauge configurations was provided by the UKQCD collaboration.

[57] C. J. Morningstar, *Heavy-quark self-energy in nonrelativistic lattice QCD*, Phys. Rev. D **48**, 2265 (1993).

[58] C. T. H. Davies, K. Hornbostel, G. P. Lepage, A. Lidsey, P. McCallum, J. Shigemitsu and J. Sloan, *Scaling of the* Υ *spectrum in Lattice QCD*, in preparation.

[59] A. J. Lidsey, PhD thesis, *Non-Relativistic QCD on the Lattice.*

[60] UKQCD collaboration, R. D. Kenway, Nucl. Phys. B (Proc. Suppl.) **53**, 209 (1997); UKQCD collaboration, H. P. Shanahan *et al*, *Effect of tree-level and mean-field improvement on the light-hadron spectrum in quenched QCD*, Phys. Rev. D **55** 1548 (1997).

[61] GF11 collaboration, F. Butler *et al*, *Hadron masses from the valence approximation to lattice QCD*, Nucl. Phys. B **430**, 179 (1990).

[62] H. D. Trottier, *Quarkonium spin structure in lattice NRQCD*, Phys. Rev. D **55**, 6844 (1997).

[63] The values of u_{0L} at $\beta = 6.0$ and 6.2 were supplied by Jon Ivar Skullerud (UKQCD collaboration).

[64] R. Van Royen and V. F. Weisskopf, *Hadron Decay Processes and the Quark Model*, Nuovo Cim. Serie 10 A **50**, 617 (1967); Errata, Nuovo Cim. Serie 10 A **51**, 583 (1967).